IMPROVED SEGMENTATION AND ANALYSIS OF WHITE MATTER TRACTS BASED ON ADAPTIVE GEODESIC TRACKING

by

Xiang Hao

A dissertation submitted to the faculty of
The University of Utah
in partial fulfillment of the requirements for the degree of

Doctor of Philosophy

in

Computing

School of Computing

The University of Utah

May 2014

The University of Utah Graduate School

STATEMENT OF DISSERTATION APPROVAL

The dissertation of **Xiang Hao**

has been approved by the following supervisory committee members:

Thomas Fletcher	, Chair	**01/22/2014** Date Approved
Ross Whitaker	, Member	**01/22/2014** Date Approved
Guido Gerig	, Member	**01/22/2014** Date Approved
Robert Michael Kirby, II	, Member	**01/22/2014** Date Approved
Janet Lainhart	, Member	Date Approved

and by **Ross Whitaker**, Chair/Dean of

the Department/College/School of **Computing**

and by David B. Kieda, Dean of The Graduate School.

ABSTRACT

Recent developments in magnetic resonance imaging (MRI) provide an in vivo and noninvasive tool for studying the human brain. In particular, the detection of anisotropic diffusion in biological tissues provides the foundation for diffusion-weighted imaging (DWI), an MRI modality. This modality opens new opportunities for discoveries of the brain's structural connections. Clinically, DWI is often used to analyze white matter tracts to understand neuropsychiatric disorders and the connectivity of the central nervous system. However, due to imaging time required, DWI used in clinical studies has a low angular resolution. In this dissertation, we aim to accurately track and segment the white matter tracts and estimate more representative models from low angular DWI.

We first present a novel geodesic approach to segmentation of white matter tracts from diffusion tensor imaging (DTI), estimated from DWI. Geodesic approaches treat the geometry of brain white matter as a manifold, often using the inverse tensor field as a Riemannian metric. The white matter pathways are then inferred from the resulting geodesics. A serious drawback of current geodesic methods is that geodesics tend to deviate from the major eigenvectors in high-curvature areas in order to achieve the shortest path. We propose a method for learning an adaptive Riemannian metric from the DTI data, where the resulting geodesics more closely follow the principal eigenvector of the diffusion tensors even in high-curvature regions. Using the computed geodesics, we develop an automatic way to compute binary segmentations of the white matter tracts. We demonstrate that our method is robust to noise and results in improved geodesics and segmentations. Then, based on binary segmentations, we present a novel Bayesian approach for fractional segmentation of white matter tracts and simultaneous estimation of a multitensor diffusion model. By incorporating a prior that assumes the tensor fields inside each tract are spatially correlated, we are able to reliably estimate multiple tensor compartments in fiber crossing regions, even with low angular diffusion-weighted imaging. This reduces the effects of partial voluming and achieves a more reliable analysis of diffusion measurements.

CONTENTS

LIST OF FIGURES

LIST OF TABLES

ACKNOWLEDGMENTS

First and foremost, I would like to express my sincere gratitude to my advisor Tom Fletcher for his continuous support during my doctoral study. I joined Tom's research group in May 2009 and started to work on DWI research. At that time, I had no idea how to conduct research or write academic papers. Tom is a very nice and patient advisor. In my early days of my Ph.D. program, he spent a great deal of time providing me with background knowledge and discussing different research directions. His guidance was a key throughout my whole Ph.D. program, and the logical thinking ability I leaned from him will definitely play an important role in my future work and research.

I would like to thank Ross Whitaker. Ross always has very insightful thoughts about how to solve research problems. For example, he proposed the idea of scaling the Riemannian metric to correct the high curvature geodesic deviation, and this idea was turned into my first academic paper. Special thanks to Guido Gerig. His knowledge about image analysis and computer vision helped me obtain a broader view of my research. I would also like to thank Mike Kirby for his willingness to help. I can still remember the helpful discussion with him about how to discretize partial differential equation appropriately. Also, I would like to give thanks to Janet Lainhart for her great support of my research. I am so lucky to work with Doctor Lainhart. She is so kind and nice, and her comments from the clinical side are extremely helpful for a computer science student.

Numerous people have made my life and research more enjoyable and productive. Special thanks to Kristen Zygmunt. Her expertise in software development has helped me solve many technical problems efficiently. I would also like to thank my fellow students and colleagues: Sylvain Gouttard, Sarang Joshi, Fangxiang Jiao, Wei Liu, Dafang Wang, Bo Wang, Nikhil Singh, Gopalkrishna Veni, Prasanna Venkatesh, Jacob Hinkle, Neda Sadeghi, and numerous other people for the helpful discussions. Also, thanks to the the SCI staff: Christine Pickett, Deborah Zemek, Edward Cask, Magali Coburn, Brenda Peterson, and Tony Portilo. Their support made me enthusiastic and concentrative to work at SCI.

Last, but not least, I want to thank my parents, Dongsheng Hao and Yulan Gong, and my sister, Jian Hao, for their selfless support throughout my life. Finally, and most importantly, I want to thank my wife, Jing Xie, for her invaluable love and support.

CHAPTER 1

INTRODUCTION

1.1 Motivation

For the past centuries, many histological studies have been conducted to explore the unknown structures of the brain [1–4]. While these studies are productive and effective, they are ex vivo and commonly involve cells/tissue sectioning and staining. Fortunately, the developments of magnetic resonance imaging (MRI) [5–9] in the last century provide us an in vivo and noninvasive tool [10–14] that can create good contrast between soft tissues of the human body. Moreover, diffusion-weighted imaging (DWI) [15–17], an MRI modality, opens new opportunities for discoveries of the brain's structural connections [18–26], as it can measure the diffusion of water along different gradient directions in tissues (such as brain white matter) and reveal in vivo properties of the brain white matter.

Clinically, DWI is useful for understanding neuropsychiatric disorders [27, 28], such as autism [29] and the connectivity of white matter tracts of the central nervous system. For example, DWI can be used to study normal brain development [30–33] over time, analyze the differences between typically developing people and people with disorders or diseases [34–37], and research the connections between different functional regions of the brain. In these kinds of studies, tracking and segmenting white matter tracts [38–63] with certain modeling of diffusion signals is often the primary goal of DWI analysis, and the extracted diffusion measurements (computed based on the diffusion model) from the segmented white matter tracts are used in the further statistical analysis.

There are many ways to model the DWI signals [17,64–75]. One important way to decode the diffusion signals is diffusion tensor imaging (DTI) [17], during which a second-order tensor is used to model the diffusion in a voxel from the DWI data. This model only requires DWI signals along a small number of gradient directions. The derived diffusion measurements, such as fractional anisotropy (FA) and mean diffusivity (MD), are widely used in clinical studies. While the diffusion tensor provides an elegant characterization of anisotropic diffusion in white matter, it is limited to represent only one tract in each imaging voxel, which is problematic in the presence of multiple fibers, such as fiber crossing or partial

voluming. High-angular resolution diffusion imaging (HARDI) (see [65] for a review) has been introduced as a means of distinguishing multiple diffusion compartments. It requires DWI signals along many more gradient directions. Several multicompartment models of diffusion have been introduced, such as the multitensor [66] and ball-and-stick [72] models. However, one drawback to HARDI is the increased imaging time required, which has been a barrier to its introduction in clinical studies. *Therefore, given the low angular DWI data in clinical studies, it is interesting to ask how we can accurately track and segment the white matter tracts, and whether it is possible to estimate a HARDI model, such as the multitensor model.*

Several works have developed methods for tracking and segmenting white matter tracts from DWI data, such as deterministic tractography [38–40]. These methods compute streamlines (sometimes called fibers) by forward integration of the principal eigenvector of the diffusion tensors, estimated from DWI signals, from a region. The streamlines are filtered by predefined regions of interest (ROIs) to create a segmentation of a white matter tract. One major problem with tractography is that imaging noise causes errors in the principal eigenvector direction, and these errors accumulate in the integration of the streamlines. Stochastic tractography [41–46] is an approach that deals with the problems arising from image noise. In these methods, large numbers of streamlines are initiated from each seed voxel and are integrated along directions determined stochastically at each point. However, this is a computationally-intensive procedure (typically requiring several hours). Also, stochastic tractography, like deterministic tractography, suffers from the same problems with streamlines stopping in noisy or low-anisotropy regions, leading to artificially low (or even zero) probabilities of connection.

An alternative approach that deals with this problem is the front-propagation methods [47–55]. The methods infer the pathways of white matter by first evolving a level set representing the time-of-arrival of paths emanating from a predefined starting region. Then, pathways are computed by integrating the characteristic vectors of the level set backward from any target point to the starting region [49]. The direction and speed of this evolving front at each point is determined by a cost function chosen by the users or derived from the diffusion tensor data. One such method, first proposed by O'Donnell et al. [48], is to treat the inverse of the diffusion tensor as a Riemannian metric and the paths in the propagating front as geodesics, i.e., shortest paths under this metric. This makes intuitive sense: traveling along the large axis of the diffusion tensor results in shorter distances, while traveling in the direction of the small axes results in longer distances. Therefore, the

shortest paths will tend to remain tangential to the principal eigenvector of the diffusion tensor.

Front-propagation approaches for analyzing white matter pathways are attractive for at least three reasons. First, the front-propagation algorithms are more robust to noise than both deterministic tractography and stochastic tractography. This is because front-propagation methods compute fibers by optimizing a global criterion over the whole brain, so the wavefront is not constrained to follow exactly the principal eigenvector of the tensors. Although the principal eigenvector of the tensor is the preferred direction for paths to travel, the minimal-cost paths may deviate from these directions if the deviation decreases the overall cost, and hence the paths are less sensitive to noise or partial voluming. Second, front-propagation methods can compute a large number of fibers using a short computational time. Efficient implementations of front-propagation solvers are much faster (typically requiring several seconds) than stochastic tractography. The graphics processing unit (GPU) implementation by Jeong et al. [76] even runs at near real-time speeds. Finally, as shown by Fletcher et al. [52], front-propagation methods can be used to segment white matter tracts by solving the geodesic flow from two ROIs and combining the resulting cost functions. In contrast to tractography methods, this approach has the advantage that the solution will not get stuck in regions of noisy data or low anisotropy.

While this is a powerful framework for computing white matter pathways, these geodesics have the serious deficiency that they tend to deviate from the eigenvector directions in high-curvature tracts and take straighter trajectories than is desired [53–55]. That is, in high-curvature regions, the incremental cost of following the tensor field is overcome by the cost associated with the longer (more curved) path. To solve this problem, I develop a new Riemannian metric that relies on diffusion tensor data but resolves this problem by adapting to high-curvature tracts. This results in geodesic paths that more faithfully follow the principal eigenvectors. Based on the computed geodesics from the two end regions of a white matter tract, I develop an automatic binary segmentation framework resulting in segmentations that better delineate the white matter tracts without requiring the users to tune parameters or employ other kinds of user intervention [55].

Despite the advantages of the binary segmentation framework, it uses DTI model and it is limited to segment only one diffusion tensor in each imaging voxel. In several regions of our brain, such as corona radiata, at least two white matter tracts are passing through each other, and voxels at these region have two or even more neural tracts traveling in different directions. In addition, some white matter tracts are mixed with gray matter or

cerebrospinal fluid (CSF) at the boundary, such as in the corpus callosum of the human brain. In these cases, a single diffusion tensor cannot separate them, and thus the signal diffusion tensor is inappropriate and the characterization of the diffusion in these voxels using the signal diffusion tensor model is inaccurate. Furthermore, binary segmentations sometimes undersegment or oversegment the white matter tracts, which could bias the diffusion measurement statistics and produce misleading results in clinical studies. To overcome the drawbacks mentioned above, I propose a novel Bayesian approach to estimate simultaneously both the fractional segmentation of white matter tracts and the multitensor diffusion model [77]. Our model consists of several white matter tracts, and each voxel contains a set of weights and tensor compartments. By incorporating a prior that assumes the tensor fields inside each tract are spatially correlated, we are able to estimate reliably multiple tensor compartments in fiber crossing regions, even with low angular diffusion-weighted imaging (DWI). Our model distinguishes the diffusion compartment associated with each tract, which reduces the effects of partial voluming and achieves more reliable statistics of diffusion measurements.

1.2 Thesis Statement

Geodesic tracking with an adaptive Riemannian metric results in more representative geodesics and more accurate segmentations of white matter pathways. Using a spatial prior, we can estimate fractional segmentation and multitensor compartments simultaneously even with low angular DWI. The proposed methods reduce the partial volume effects and result in a more reliable diffusion measurement analysis in clinical studies.

The term *adaptive* means that the Riemannian metric is modulated based on the curvature of white matter tracts. The modulated metric will let the geodesic faithfully follow the principal eigendirection of tensors in a region.

The term *fractional segmentation* means that we estimate multitensor compartments in each voxel. Each compartment belongs to a white matter tract, and it is associated with a number that reveals the fraction of the voxel occupied by the corresponding tract.

1.3 Contributions

I propose the following contributions:

- **Adaptive Riemannian Metrics for Improved Geodesic Tracking.** We formulate a modification of the Riemannian metric that results in geodesics adapted to

follow the principal eigendirection of the tensor even in high-curvature regions. We show that this correction can be formulated as a simple scalar field modulation of the metric and that the appropriate variational problem results in a Poisson's equation on the Riemannian manifold. We demonstrate that the proposed method results in improved geodesics using both synthetic and real DTI data.

- **Binary Segmentation of White Matter Tracts Based on Geodesic Tracking.** We propose an automatic method to segment white matter tracts based on the angles of the two characteristic vector fields from the two ROIs. There are almost no parameters in our whole framework, and the only necessary user intervention is to draw the ROIs. As such, our method can be very useful for large data clinical studies, where fewer parameters and less user intervention are preferred.
- **Joint Fractional Segmentation and Multitensor Estimation.** To overcome the drawbacks of binary segmentation, we propose a novel Bayesian approach for fractional segmentation of white matter tracts and simultaneous estimation of a multitensor diffusion model. By incorporating a prior that assumes the tensor and fraction fields inside each tract are spatially correlated, we are able reliably to estimate multiple tensor compartments in fiber crossing regions, even with low angular diffusion-weighted imaging (DWI).
- **Diffusion Measurement Analysis of Autism Disorder.** I apply both binary segmentation and fractional segmentation to explore the white matter abnormalities in autism neuropsychiatric disorder by analyzing the diffusion measurements from both typically developing people and people with neuropsychiatric disorders. I also compare the results from binary segmentation with the ones from fractional segmentation.

1.4 Organization of the Thesis

The remainder of the thesis is organized as follows:

Chapter 2 provides the necessary background on topics including human brain white matter, diffusion weighted imaging, Riemannian geometry, and methods used to study brain white matter.

Chapter 3 presents a geodesic-based method to track the brain white matter tracts. This method uses a modification of the Riemannian metric that results in geodesics adapted to follow the principal eigendirection of the diffusion tensor even in high-curvature brain regions.

Chapter 4 describes an automatic framework to segment white matter tracts based on the geodesic tracking of the white matter tracts. A comparison between the framework and other segmentation methods is included, and the advantages of using the automatic framework are also demonstrated.

Chapter 5 presents a Bayesian approach for fractional segmentation of white matter tracts and simultaneous estimation of a multitensor diffusion model. This method incorporates a prior that assumes the tensor fields inside each tract are spatially correlated, and it reliably estimates multiple tensor compartments in fiber crossing regions, even with low angular DWI. The method is also applied to explore the white matter abnormalities in autism neuropsychiatric disorders, with a comparison of binary segmentation method.

Chapter 6 concludes with a discussion of the dissertation's contributions and limitations and proposes possible future research in DWI segmentation and tracking.

CHAPTER 2

BACKGROUND

2.1 Human Brain White Matter

The human brain contains about 100 billion neurons and 100 trillion synapses, and its major components are grey matter and white matter. Grey matter consists mostly of neuronal cell bodies, and it contains regions that coordinates the human senses, such as taste, smell, hearing, speech, and vision. White matter, in contrast, is mainly made up of glial cells and myelinated axons that transmit signals between functional regions in the grey matter.

Axons are projections of nerve cells, as shown in Fig. 2.1, and they transmit signals to other cells in the grey matter. Therefore, white matter plays an important role in coordinating communication between different brain functional regions, affects how the brain learns and functions, and is related to many common diseases, such as Autism, Alzheimer's disease, and Multiple Sclerosis. During the past few centuries, histological studies have been conducted to explore the brain white matter. However, these studies are ex vivo. But, fortunately, recent developments in diffusion-weighted imaging (DWI) provide an in vivo and noninvasive tool to explore the brain white matter.

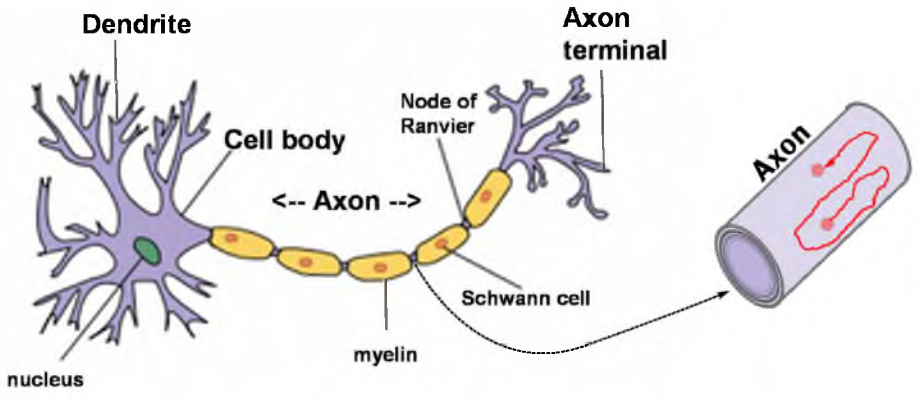

Fig. 2.1. Structure of a neuron. The image is adapted from Wikipedia [78].

2.2 Diffusion Weighted Imaging

As shown in Fig. 2.1, water molecules in tissues, such as axons, are not free. They can move around but are restricted by many obstacles, such as membranes. DWI can characterize the diffusion process of water molecules in biological tissues, and thus it can be used to study properties of white matter tissues [15–17, 64]. In this section, we will briefly explain water diffusion and DWI (Section 2.2.1) and discuss different diffusion modeling techniques (Section 2.2.2).

2.2.1 Molecular Diffusion and DWI

Diffusion, or molecular diffusion, is a natural process in which each molecule randomly moves around at temperatures above absolute zero. The motion of each molecule is known as Brownian motion, a concept developed by Albert Einstein [79]. According to Einstein's law, although the motions of every molecule are unpredictable, the radius, r, of the smallest circle that contains all possible molecule positions after time τ can be modeled as

$$r = \sqrt{6D\tau}.$$

On one hand, if the motions are unimpeded, the distance of a molecule from its original position is dependent only on its diffusion coefficient, D, and the time allowed to diffuse. As illustrated in the left column of Fig. 2.2, starting at the same position, 10 molecules move randomly without any spatial constraints, but after a lapse of time, the molecules are distributed within a circle. On the other hand, if the molecules are impeded in certain directions, water molecules tend to move slower in the impeded directions, and the motion of the molecules is anisotropic, as shown in the right column of Fig. 2.2. In human brain white matter, the diffusion of molecules is impeded by numerous anisotropic biological tissues, such as cell membranes, myelin sheaths, and axons. For example, in the right image of Fig. 2.1, since the axons have a tubular structure, water molecules diffuse much faster along the axon than they do across its membrane.

The detection of the anisotropic diffusion in biological tissues provides the foundation for DWI. By applying different gradient directions, g_j, during the imaging, the motion of molecules causes signal decay along the directions (see [64] for more details about principles of DWI). Thus, we can use the acquired diffusion weighted signals, S_j, to model the molecular diffusion.

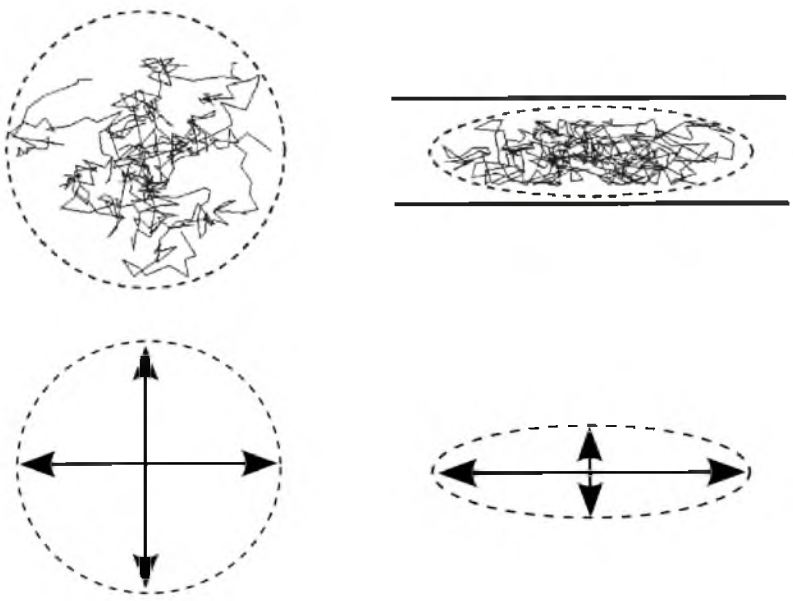

Fig. 2.2. Computer simulated Brownian motion (adapted from Lim et al. [80]). Isotropic motion (left) versus anisotropic motion (right).

2.2.2 Different Diffusion Modeling Techniques

There are many ways to model diffusion signals. One important way to model the diffusion from DWI signals S_j is through the diffusion tensor imaging (DTI) model [17], which uses a positive-definite symmetric 3×3 matrix (diffusion tensor) D to describe the DWI signals S_j in a voxel x as

$$S_j(x) = S_0(x)e^{-bg_j^T D(x)g_j}.$$

In this formula, b is the known b-value, S_0 is the acquired baseline image, and g_j is the j-th gradient encoding direction. Technically, as there are six unknowns in matrix D, we only need DWI signals along six gradient directions to estimate D. However, we usually need more to get a robust estimation.

In Fig. 2.3, we show a slice of DTI, where each voxel, a diffusion tensor D, is visualized by an ellipsoid.

Since D is positive-definite and symmetric, we can compute its eigendecomposition as $D = R\Sigma R^{-1}$, where each column of R is an eigenvector of D, and Σ is a diagonal matrix, of which the diagonal elements are the corresponding eigenvalues λ_i. The eigenvector corresponding to the largest eigenvalue is called the principal eigenvector, as shown in the red arrow in the right image of Fig. 2.3. The principal eigenvector represents the direction,

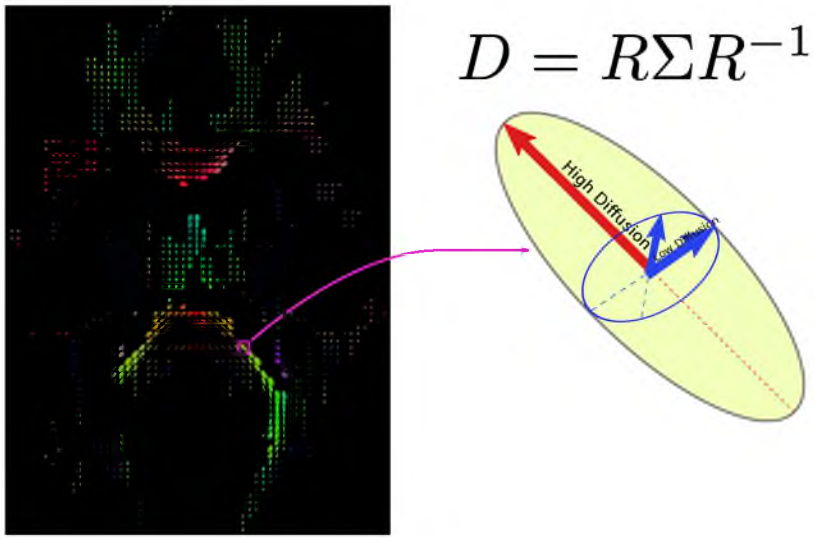

Fig. 2.3. A slice of a DTI.

in which the water molecules diffuse the fastest. In Fig. 2.4, we show a color-coded principal eigenvector image. In the image, the colors represent different tensor directions, and the saturation represents the anisotropy of the tensors.

To measure the anisotropy and the total amount of diffusion, numerous diffusion measurements have been derived from the diffusion tensor D, such as fractional anisotropic (FA) and mean diffusivity (MD), which are widely used in clinical studies. The formula for FA is

$$\text{FA} = \frac{\sqrt{3((\lambda_1 - E[\lambda])^2 + (\lambda_2 - E[\lambda])^2 + (\lambda_3 - E[\lambda])^2)}}{\sqrt{2(\lambda_1^2 + \lambda_2^2 + \lambda_3^2)}}.$$

The FA value represents the normalized standard deviation of the diffusivities. When the second and the third axes have the same eigenvalue as the principal axis, D is spherical and the FA is 0. When the principal axis has a much larger eigenvalue, D is elongate and the FA is close to 1. The formula for MD is

$$\text{MD} = \frac{1}{3}(\lambda_1 + \lambda_2 + \lambda_3),$$

which can be thought of as the average diffusivity in the voxel.

While the diffusion tensor is an elegant description of anisotropic diffusion in white matter and it only requires DWI signals along a few number of gradient directions, it represents only one tract in each imaging voxel, which is problematic in the presence of fiber crossing or partial voluming. High-angular resolution diffusion imaging (HARDI) (see [65] for a review) has been introduced as a means to distinguish multiple diffusion

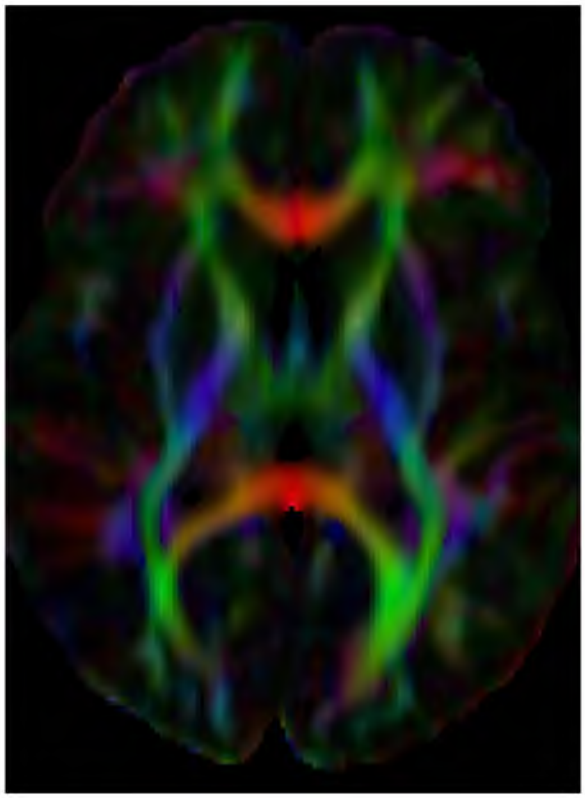

Fig. 2.4. Color-coded principal eigenvector image.

compartments, and it requires DWI signals along much more gradient directions. There are many methods, such as multicompartment [66, 72], q-space [69], diffusion spectrum imaging (DSI) [64], spherical harmonics [70], q-ball [67], and high order tensor method [73, 74], to model the HARDI signals. Among the introduced models, the multitensor [66] model is one of the models that is widely used.

To model multiple diffusion compartments within a voxel, whether from crossing white matter fiber tracts or mixtures of white matter with CSF or gray matter, the multitensor model uses n tensor compartments, D_i. Each tensor compartment is associated with a nonnegative volume fraction f_i to model the DWI signals S_j as

$$S_j(x) = S_0(x) \sum_{i=1}^{n} f_i(x) e^{-b g_j^T D_i(x) g_j}, \text{ with } f_i \geq 0 \text{ and } \sum_{i}^{n} f_i = 1, \tag{2.1}$$

where b is the b-value, S_0 is the baseline image, and g_j is the j-th gradient encoding direction.

The multitensor model is closely related to the DTI model, and the diffusion measurements for DTI can also be applied to each diffusion tensor of the multitensor model. In fact, when one of the fractions is equal to 1, the multitensor model is equivalent to the DTI

model, but to estimate f_i and D_i, DWI signals along more gradient directions are required. The larger the n, the more DWI signals are required.

2.3 White Matter Tracking and Segmentation Methods

In DWI, there exist three major classes of methods to analyze white matter pathways: deterministic tractography [38–40], stochastic tractography [41–46], and front-propagation [47–54]. Deterministic tractography computes streamlines by integrating the principal eigenvectors of the diffusion tensors from a seed region. One disadvantage of this technique is that it is sensitive to noise, as it accumulates errors arising from image noise along the integration of the streamlines. It also has difficulty in cases where the goal is to find pathways between two regions because the streamlines are likely to prematurely stop due to image noise. Another similar approach is stochastic tractography, in which a large number of streamlines are initiated from each seed voxel and are integrated along directions determined stochastically at each point. However, this is a computationally intensive procedure, and it suffers from the same problems with streamlines stopping in noisy or low-anisotropy regions. An alternative method is front-propagation, which infers the white matter pathways using geodesics between two regions. It is an attractive technique and has at least two major advantages. First, it is more robust to noise, for it considers the whole diffusion tensor field, and second, it is more efficient and computes the geodesics from a starting region to any other region simultaneously. In the following subsections, we provide an overview of these three methods.

2.3.1 Deterministic Tractography

In DTI, each voxel is a diffusion tensor, D, which is represented by a 3×3 symmetric positive-definite matrix. From linear algebra, we know D has 3 eigenvalues, $\lambda_1 \geq \lambda_2 \geq \lambda_3$, and 3 eigenvectors, e_1, e_2, and e_3, corresponding to the eigenvalues. Recall that water molecules have a maximum diffusion along e_1, and we usually call e_1 the principal eigenvector or the orientation of D. We can reconstruct the fiber tracts by integrating the principal eigenvector of the diffusion tensor from a predefined seed region, as shown in the right image of Fig. 2.5. The left image of Fig. 2.5 shows some integrated streamlines filtered by some predefined ROIs. This algorithm is usually called deterministic tractography or streamline tracking. The pseudocode is in Algorithm 1.

Deterministic tractography [38–40] computes streamlines (sometimes called fibers) by forward integration of the principal eigenvector of the diffusion tensors from one region.

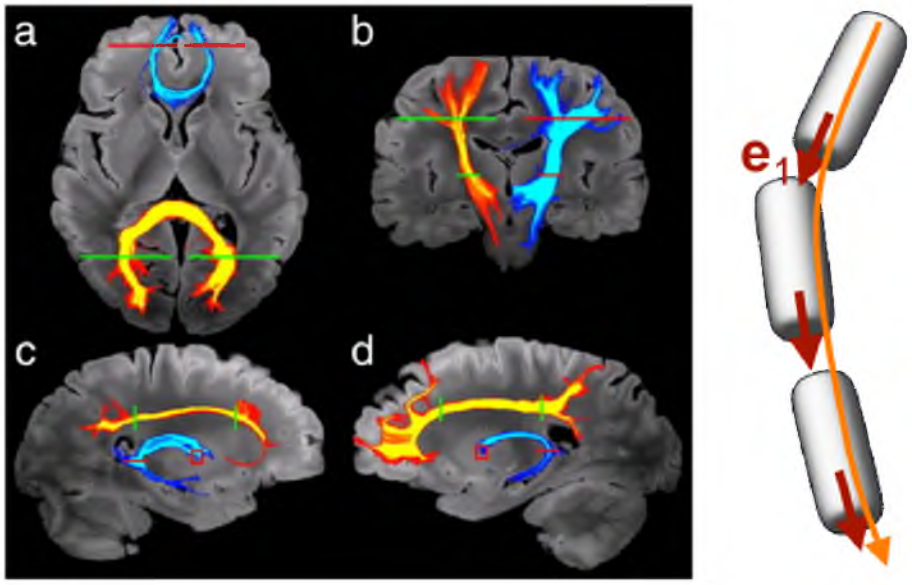

Fig. 2.5. Figure is adapted from Miller et al. [81].

Algorithm 1 Deterministic tractography algorithm in a generic form

```
for each voxels x in the seed region do
  while none of the stop criteria is triggered do
    v(x) = the principal eigenvector of the diffusion tensor D(x) at x.
    Do one step of forward integration along v(x).
  end while
end for
```

One major problem with tractography is that imaging noise causes errors in the principal eigenvector direction, and these errors accumulate in the integration of the streamlines. Another disadvantage to tractography is that it has difficulty in cases where the goal is to find pathways between two regions. In this scenario, streamlines begin in one of the regions and are accepted only if they eventually pass through the desired ending region. However, several factors conspire to often result in only a small fraction of fibers being accepted. For example, accumulated errors in the streamlines can throw them off the final destination. Also, noise and partial volume effects in the tensor field can cause stopping criteria to be prematurely triggered, either by low anisotropy tensors or sudden direction changes. The Brute-Force (BF) approach proposed by Conturo et al. [39] can increase the number of accepted fibers by initiating fiber tracking from every voxel in the brain. However, this approach still suffers from the same factors mentioned above and can often segment only the main core of the white matter tracts.

For diffusion modeling techniques other than DTI, the tractography algorithm is very similar to the above one, except that we need other ways to find the direction $v(x)$. The deterministic tractography algorithm is simple and easy to implement, and there exist some variants of this algorithm that improve its robustness, such as the tensor line method, in which the outgoing vector is modulated according to the orientation of the diffusion tensor, but it is still deterministic and does not account for the uncertainty of the diffusion tensor.

2.3.2 Stochastic Tractography

Stochastic tractography is a class of algorithms that is similar to deterministic tractography, but it considers the uncertainty along the fiber tracking. The major difference between deterministic and stochastic tractography is that stochastic tractography initiates a large number of streamlines from each seed voxel, as shown in the bottom image of Fig. 2.6. The streamlines are integrated along directions determined stochastically at each point. The pseudocode is in Algorithm 2.

Compared to deterministic tractography, the modeling of the probability density function (PDF) $p(x)$ and sampling steps are much more complicated, and the cost of estimating $p(x)$ and sampling varies as the models and sampling methods change, but it usually costs much more than an eigendecomposition of a diffusion tensor. Several estimated

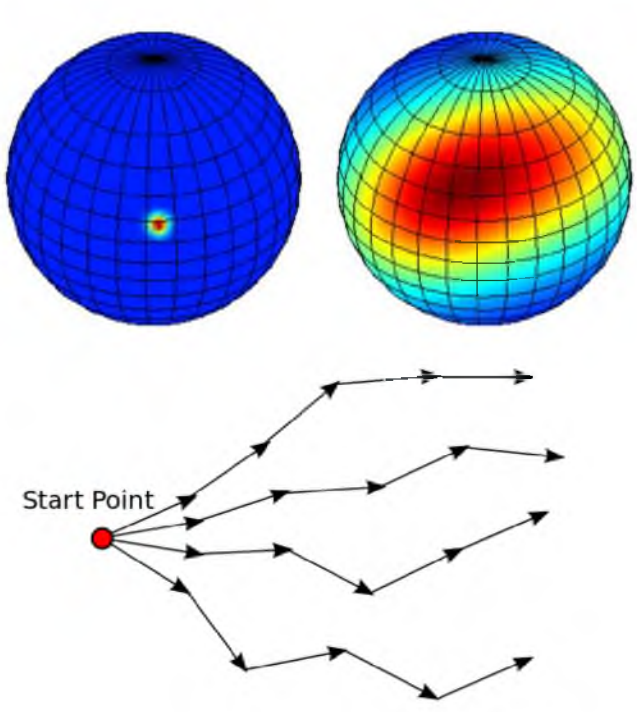

Fig. 2.6. Figure is adapted from Friman et al. [82].

Algorithm 2 Stochastic tractography algorithm in a generic form

```
for each voxels x in the seed region do
  N: number of streamlines initiated from each seed voxel
  for i = 0; i < N; i++ do
    while none of the stop criteria is triggered do
      Sample a direction v(x) from the estimated probability density function p(x) from
      the previous direction and the diffusion tensor D(x) at x.
      Do one step of forward integration along v(x).
    end while
  end for
end for
```

$p(x)$ are shown in the top image of Fig. 2.6. For more details, please refer to [82–84]. Since large numbers of streamlines are initiated from each seed voxel and are integrated along directions determined stochastically at each point, this is a computationally intensive procedure (typically requiring several hours). Also, stochastic tractography suffers from the same problems with streamlines stopping in noisy or low-anisotropy regions, leading to artificially low (or even zero) probabilities of connection. Although Barbieri et al. [85] combined tensor clustering technique with stochastic tractography in order to improve the accuracy of the segmentation results, this method introduces more parameters and strongly depends on the quality of the connectivity map.

Stochastic tractography computes many tracts starting from the seed region A. From these tracts, we can compute the probability of region A's connection to another region B, $p(A \rightarrow B)$, by basically computing the fraction of fibers that pass B, as mentioned in [82]. Intuitively, $p(A \rightarrow B)$ provides some information about whether there is a connection between A and B; i.e., if the probability is high, there is probably a connection between A and B; otherwise, there is less likely a connection between A and B. However, this probability has limitations. First, the probability $p(A \rightarrow B)$ is not necessarily symmetric; i.e., $p(A \rightarrow B)$ is not always equal to $p(B \rightarrow A)$, which means B is less likely connected to A even if A is probably connected to B. Second, this algorithm explicitly evaluates the probability $p(c)$ of each tract c, from which we can find the maximal probability path. High $p(c)$ means the associated tract is likely a true fiber (connection). However, the computed $p(c)$ depends on the length of the fiber: the probability decreases while the length of the fiber increases. So, in stochastic tractography, a short fiber usually has higher probability than a longer fiber. In other words, two regions close to each other usually have a higher connection probability than two regions distant from each other, which is probably not the case in the real human brain. Moreover, it is not necessarily true that two regions connected

with more streamlines have a stronger connectivity than two regions connected with less streamlines. So higher probability does not equate to a stronger connection. In addition, we need to be very careful when we choose the prior during the estimation of $p(x)$. If we use different priors to estimate $p(x)$ or choose different methods to sample $p(x)$, the resulting streamlines or probability map will vary.

2.3.3 Front-Propagation Method

We first give a toy example of the front-propagation method to compute the shortest distance between a point p and any other point in Fig. 2.7. From the starting point p, with a predefined local cost function (that tells us the time cost it takes to move in a direction), we compute the time it takes to arrive at any other point from point p. This computation is shown in the second image of Fig. 2.7. In the second image of Fig. 2.7, we also show the contours of this time of arrival function. These contours are just concentric circles, for we use an isotropic cost function, which means the costs of moving in any direction are the same. Then, we compute the gradient vector field of the time of arrival function and integrate the gradient field backward to p from any point q.

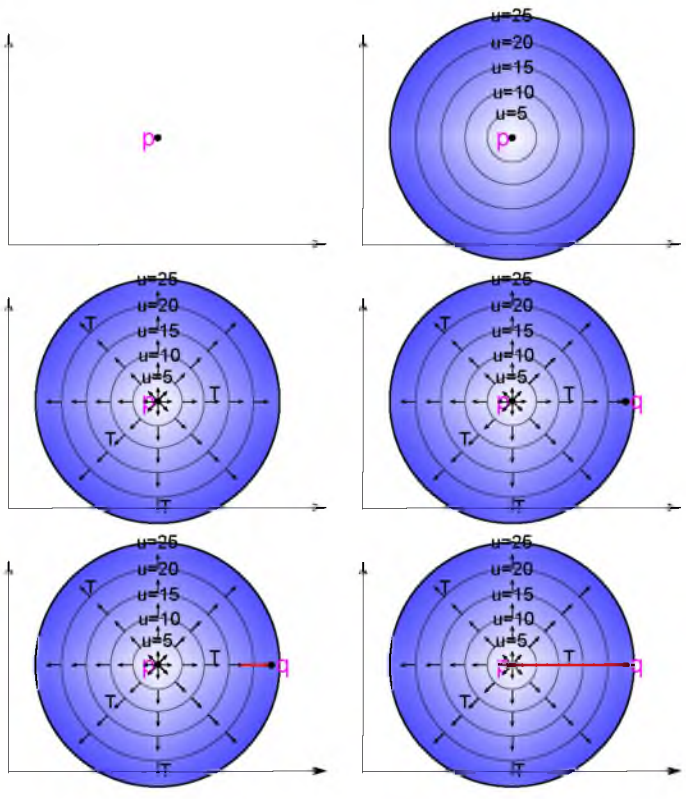

Fig. 2.7. Front-Propagation from point p with an isotropic cost function.

In the DTI literature, front-propagation approaches are one class of methods to track and segment the white matter pathways. These methods infer the pathways of white matter by first evolving a level set representing the time-of-arrival of paths emanating from some starting region. Then the pathways are computed by integrating the characteristics vectors of the level set backward from any target point to the starting region [49]. The direction and speed of this evolving front at each point is determined by some cost function derived from the diffusion tensor data. In the front-propagation method, we need to know two pieces of information beforehand. One is the starting point/region, which is shown as point p in the first image of Fig. 2.8. For visualization purposes, we use a T1 image as the background, but this whole front-propagation actually works in DTI. The other piece of information we need to know is the local cost function, $f(x, v)$, defined on every point x of the domain. The goal is to find a path that minimizes $\int_0^1 f(x, v)dt$. The local cost function depends on both the position x and the traveling direction v. It identifies the cost if we move in a certain direction v at the local position x. This cost function can be thought of as a time cost function. For example, imagine that there is a freeway in the corpus callosum and we are driving in the corpus callosum; the time cost to move along the corpus callosum is very low, for the speed limit is high on the freeway. If the road we are traveling is narrow, the time cost will be very high, for the speed limit is low on a narrow road. Put simply, the cost function tells us the traffic conditions.

Given the starting point p and the traffic condition provided by the local cost function f, we can compute how long it takes to travel from the starting point p to another position. We can also compute the time-of-arrival function u by propagating from the starting point, as shown in the last three images of Fig. 2.8. What is the time-of-arrival function? When you take a flight, the airline usually estimates the time of arrival of the destination. This function u is exactly the same as the an estimated time of arrival. As mentioned earlier, the value of the function u at a position q tells how long it takes to arrive at q from the starting point p. Fig. 2.8 shows the contours of the function u. A contour with a value, say 10 hours, tells us that within 10 hours, we can travel to any point inside the contour.

A flight not only estimates a time of arrival but also follows a specific route of travel. The time of arrival function u tells us the time cost to arrive at a point q as well as the path it takes to arrive at q. To compute this path, we can first compute the gradient of the u, '∇u', as shown in red arrows in the first image of Fig. 2.9. We then integrate from q backward to the starting point p, as shown in Fig. 2.9. This can be done for any point other than the starting point p, as shown in Fig. 2.10. Here the ∇u is quoted because

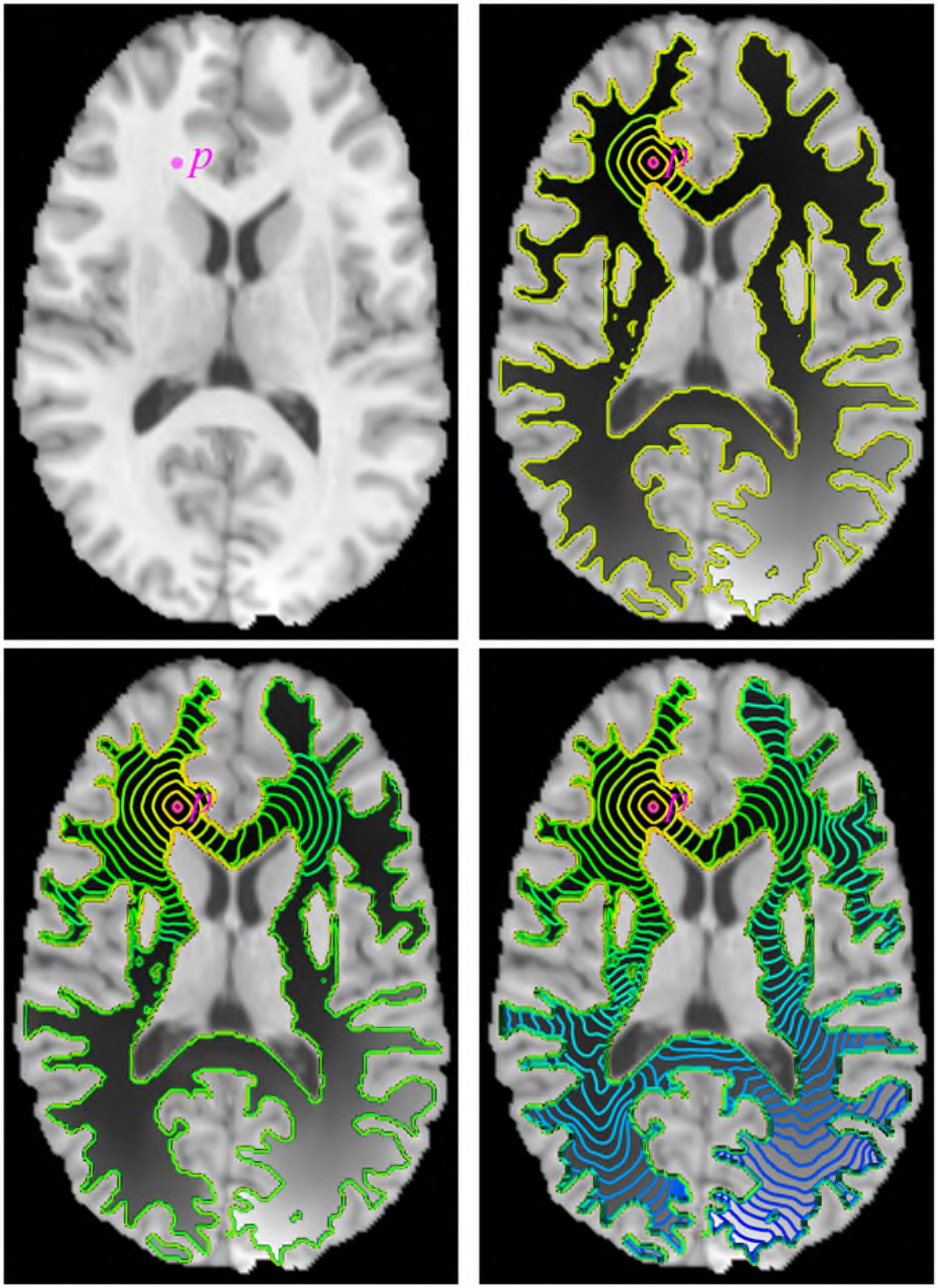

Fig. 2.8. Starting from point p, we compute a time of arrival function.

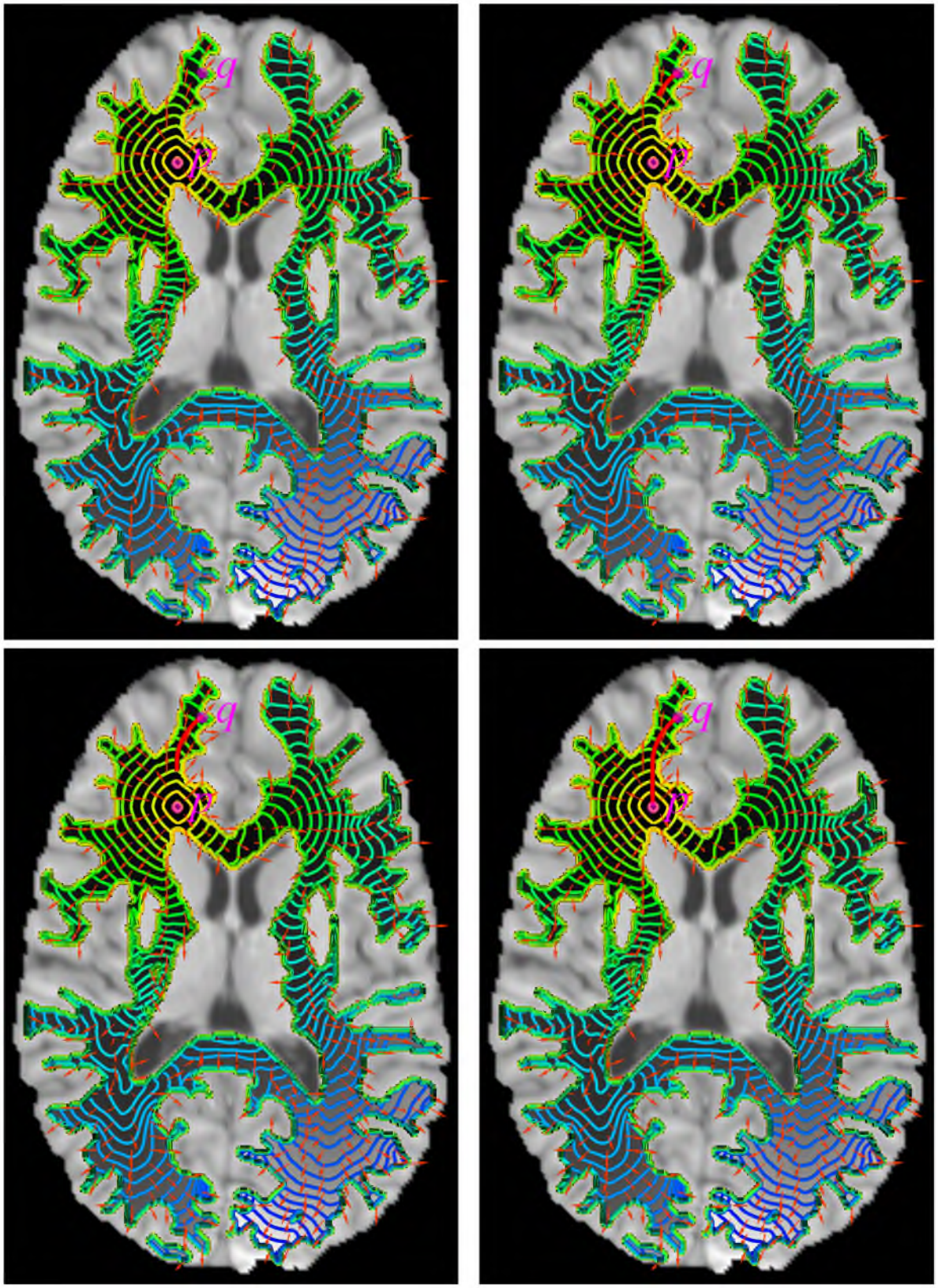

Fig. 2.9. We compute the gradient (shown in red arrows) of the time of arrival function and integrate backward to p from any other point q.

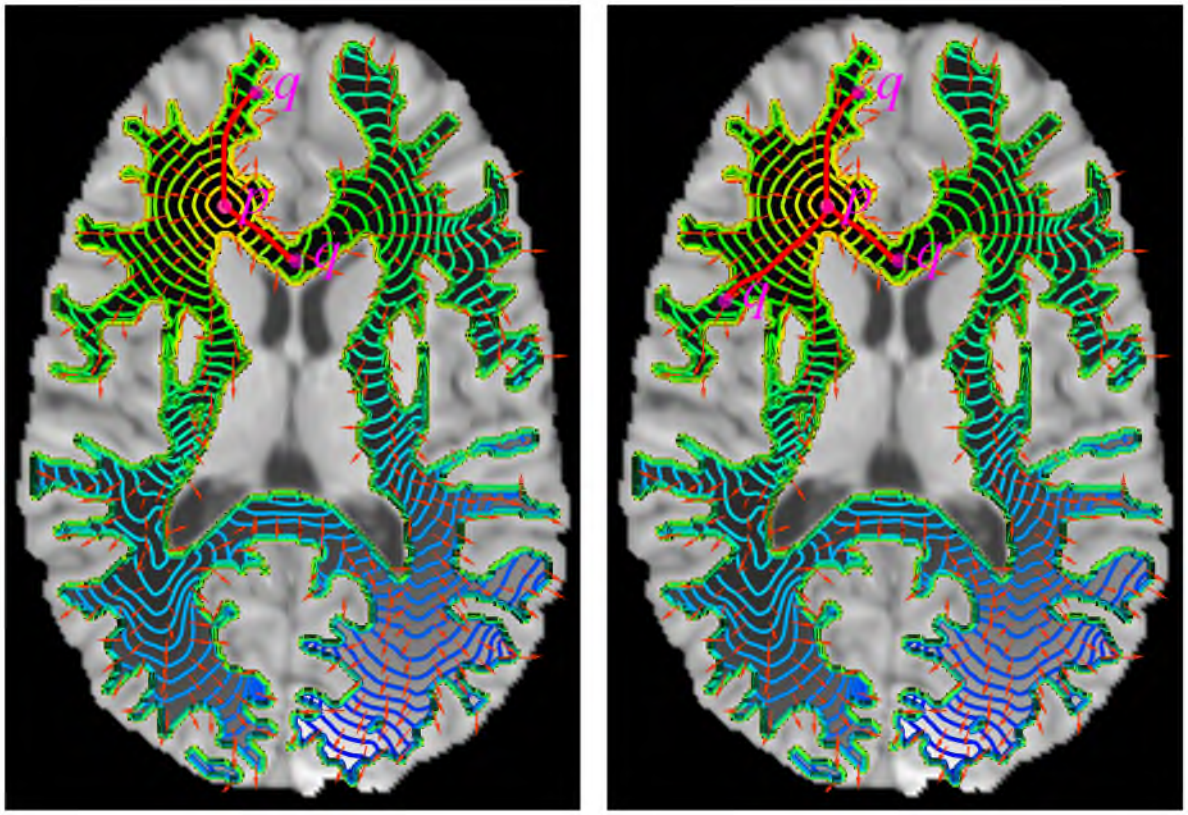

Fig. 2.10. We can compute the Geodesic between p and any other point q.

strictly speaking, sometimes, we need to modify the ∇u first before we do the integration. By computing the time-of-arrival function u, we can also get the geodesics between the starting point p and all other points. This is one property of front-propagation.

The front-propagation algorithm summarized in Algorithm 3 actually solves the Eikonal equation. For a mathematical discussion about how the Eikonal equation is related to the shortest path problem, see Section 2.4.3.

Algorithm 3 Front-Propagation algorithm in a generic form

Given a starting point/region p and a local cost function $f(x, v)$,
To find a path between p and q that minimize

$$\int_p^q f(x, v)dt$$

Step 1: compute the time-of-arrival function u by propagating from p.
Step 2: compute '∇u', from any point q integrate '∇u' backward to p to get the geodesic between p and q.

Front-propagation approaches for analyzing white matter pathways are attractive for at least three reasons. First, the front-propagation algorithms are more robust to noise

than both deterministic tractography and stochastic tractography. This is because front-propagation methods compute fibers by optimizing a global criterion over the whole brain, so the wavefront is not constrained to exactly follow the principal eigenvector of the tensors. Although the principal eigenvector of the tensor is the preferred direction for paths to travel, the minimal-cost paths may deviate from these directions if the deviation decreases the overall cost and hence are less sensitive to noise or partial voluming. Second, front-propagation methods can compute a large number of fibers using a short computational time. Efficient implementations of front-propagation solvers are much faster (typically requiring several seconds) than stochastic tractography. The graphics processing unit (GPU) implementation by Jeong et al. [76] even runs at near real-time speeds. Finally, as shown by Fletcher et al. [52], front-propagation methods can be used to segment white matter tracts by solving the geodesic flow from two ROIs and combining the resulting cost functions. This approach has the advantage that the solution will not get stuck in regions of noisy data or low anisotropy, in contrast to tractography methods. However, it also has the disadvantage that it requires the user to predefine two ROIs at the endpoints of the white matter tract of interest. Consequently, this approach is only appropriate when the anatomy of the white matter pathway is well-known, i.e., its endpoint regions can be reasonably identified, because a white matter path will always be found. Although, if a "false positive" connection is found, this can be detected using heuristic connectivity metrics as introduced by Parker et al. [47] and Jackowski et al. [49].

2.3.4 Connection between Stochastic Tractography and Front-Propagation

There are underlying similarities between front-propagation and stochastic tractography. In front-propagation, we need to select a metric, which tells the cost of moving in a direction. In stochastic tractography, we need to model the PDF, which tells us the probability of moving in a direction. The metric and PDF are, in a sense, in a reciprocal relationship with each other; i.e., a high cost when moving in a direction equates to a low probability of moving in the same direction, and a low cost when moving in a direction equates to a high probability of moving in the same direction.

On one hand, stochastic tractography computes a distribution of fibers, and there are usually many fibers connecting A and B. On the other hand, the front-propagation method computes only one fiber with the lowest cost among all fibers connecting A and B, so this fiber is optimal in terms of cost. According to stochastic tractography, this lowest cost fiber is also likely be optimal or close to optimal in terms of the fiber's probability, for it is very

likely that this fiber has the highest or close to highest probability.

So, if we choose the right pair of metric and PDF for these two methods, the lowest cost fiber between A and B computed from the front-propagation method would be the fiber with the maximal probability connection A and B in stochastic tractography. Even when we do not choose the exactly right pair of metric and PDF, the optimal curves of the two methods may be very close to each other.

If the PDF of stochastic tractography is chosen according to the metric in the front-propagation method, the front-propagation will compute a subset of the fibers computed by stochastic tractography (namely, the fibers with the highest probability). For a mathematical derivation of the relationship between stochastic tractography and front-propagation, please refer to [53].

2.4 Mathematical Background

Differentiable manifolds generalize the concepts of differential calculus. Notions such as differentiation and integration make sense on differentiable manifolds. Based on differentiable manifolds, Riemannian manifolds provide the notion of distance, and thus we can measure the length of curves. This section provides a review of the basic differentiable/Riemannian geometry that will be needed later. A good introduction to the subject may be found in [86, 87]. In addition, in Section 2.4.3, we show that we can compute the geodesics by solving the Eikonal equation.

2.4.1 Riemannian Manifold

A Riemannian manifold is a differentiable manifold equipped with a Riemannian metric. A differentiable manifold (or smooth manifold), a generalization of Euclidean space R^n, extends the differential calculus—differentiation, integration, and vector fields—to more general spaces.

In a differentiable manifold, each point has a neighborhood that is equivalent to the Euclidean space; i.e., there is an invertible map from a neighborhood of a point on the manifold to the Euclidean space, and this map is called a coordinate chart. In Fig. 2.11, we show a diagram of a chart (x, U) that maps a region U on M to an Euclidean space through function x.

In differential geometry, for each point x on a manifold M, there is a vector space attached to each point, as shown in Fig. 2.12. This vector space is called tangent space and is usually denoted as T_xM.

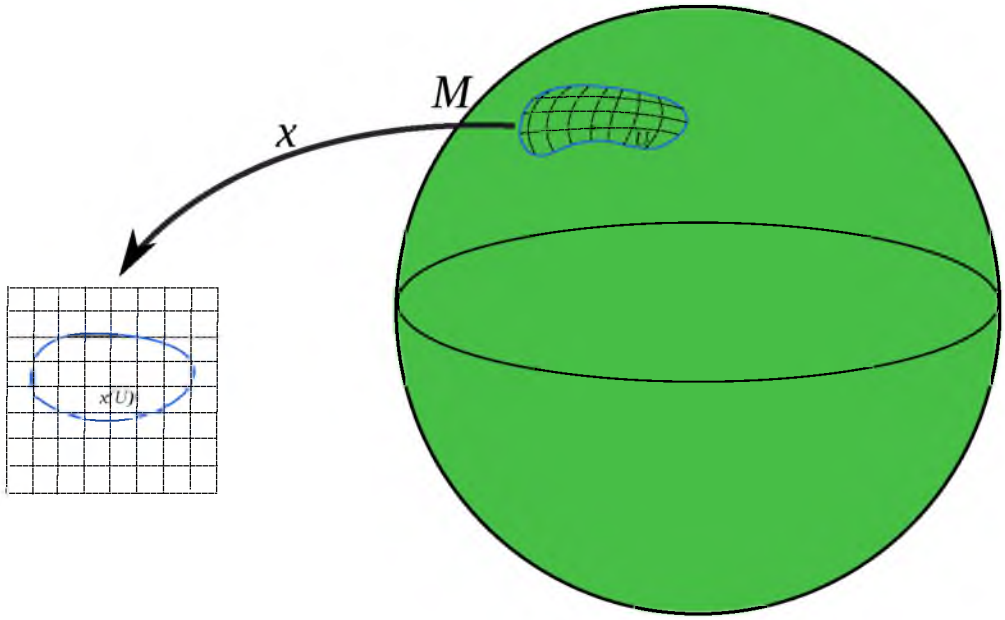

Fig. 2.11. Coordinate chart

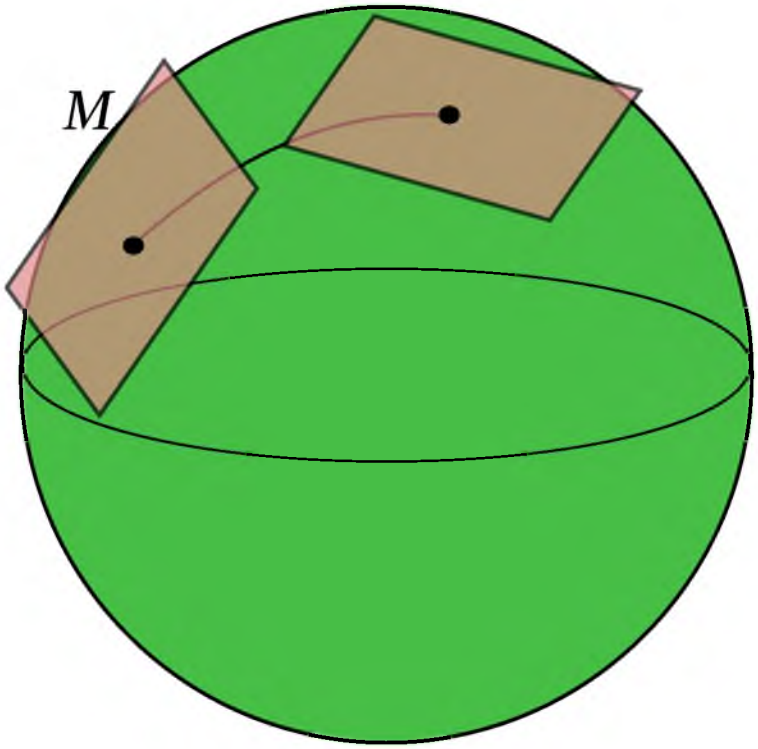

Fig. 2.12. Tangent spaces.

When a differentiable manifold is equipped with a Riemannian metric, it becomes a Riemannian manifold. The Riemannian metric is a natural development of the differential geometry. It defines an inner product $\langle v, w \rangle$ of two vectors in a tangent space, and thus, provides a way of measuring the lengths of tangent vectors and curves.

Definition 1. *A Riemannian metric on a differentiable manifold M is a smooth function that associates to each point p of M an inner product $\langle \cdot, \cdot \rangle$ on the tangent space T_pM.*

The Riemannian metric can be equated with a smoothly varying positive-definite symmetric matrix g, called the metric tensor, defined at each point. For two vectors $v, w \in T_pM$, given local coordinates $(x^1, x^2, \ldots, x^n)$ in a neighborhood of p (note that superscripts here are indices not exponentiation),

$$g_{ij} = \langle E_i, E_j \rangle,$$

where $E_i = \frac{\partial}{\partial x^i}$ are the coordinate basis vectors at p and form a basis of the tangent space T_pM. With this definition, we can compute the inner product $\langle v, w \rangle$ as $v^t g w$. Also, for a vector v, we can compute the length of the vector as $\langle v, v \rangle^{\frac{1}{2}}$.

For example, when the front-propagation method is applied to DTI, people sometimes utilize the inverse of the diffusion tensor, D^{-1}, to define a local cost function as

$$f = \langle u, v \rangle = u^T D^{-1} v.$$

In this case, since the inverse of the diffusion tensors are positive-definite symmetric and they are also Riemannian metric, a DTI is actually wrapped into a Riemannian manifold. This inverse tensor cost function makes sense, as shown in Fig. 2.13, for as we move in the major axis of the diffusion tensor, the time cost is low; as we move in the minor axis of the diffusion tensor, the cost is high.

On a Riemannian manifold M, if there exist two Riemannian metrics g_1, g_2 satisfying $g_1 = f g_2$ for some positive function f on M, we call these two metrics conformally equivalent and the function f a conformal factor.

There is a tangent space attached to each point on a manifold. To connect nearby tangent spaces (see Fig. 2.12) on a Riemannian manifold, we need the Riemannian (or Levi-Civita) connection $\nabla_X Y$, which is the derivative of a vector field Y in the direction of a vector field X. We will write the vector fields X, Y in terms of a coordinate system $(x^1, x^2, \ldots, x^n)$ as $X = \sum a^i E_i$ and $Y = \sum b^j E_j$, where a^i and b^j are smooth coefficient functions. Then, the Riemannian connection is given by

$$\nabla_X Y = \sum_k \left(\sum_i a^i \frac{\partial b^k}{\partial x^i} + \sum_{i,j} \Gamma_{ij}^k a^i b^j \right) E_k. \tag{2.2}$$

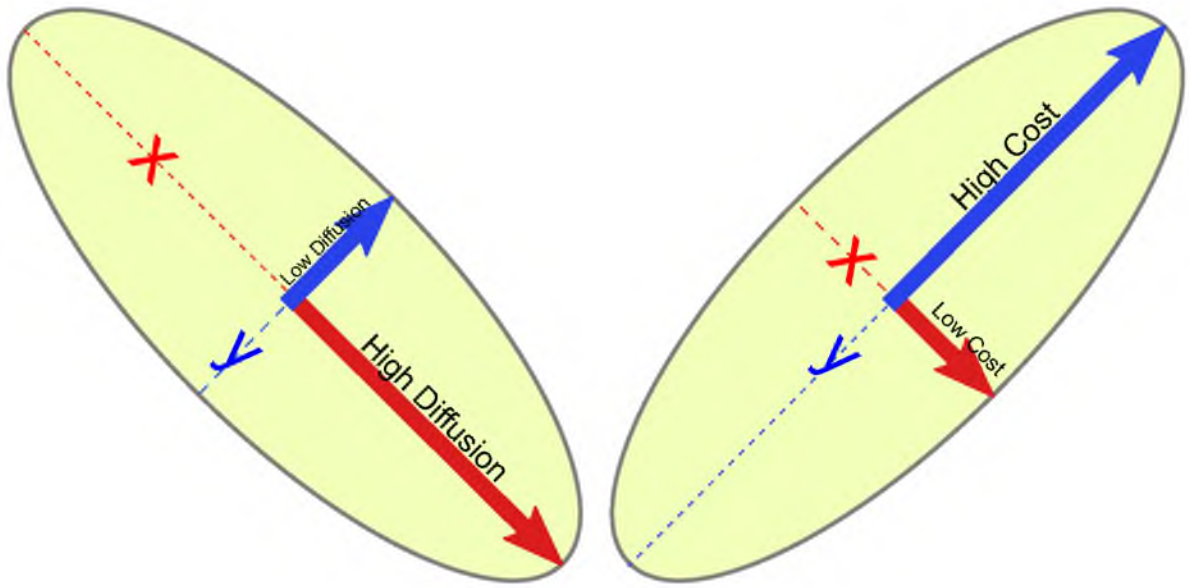

Fig. 2.13. Inverse diffusion tensor as a Riemannian metric.

The terms Γ_{ij}^k are the Christoffel symbols, which are defined as

$$\Gamma_{ij}^k = \frac{1}{2}\sum_{l=1}^{n} g^{kl}\left(\frac{\partial g_{jl}}{\partial x^i} + \frac{\partial g_{il}}{\partial x^j} - \frac{\partial g_{ij}}{\partial x^l}\right),$$

where g^{ij} denotes the entries of the inverse metric, g^{-1}. The intuition behind this Riemannian connection is that it is like a directional derivative of vector fields. In the special case of $Y = X$, $\nabla_X X$ measures how the vector field X bends along its integral curves.

2.4.2 Geodesics on Riemannian Manifold

On a Riemannian manifold, M, the geodesic between two points $p, q \in M$ (one example is shown in Fig. 2.14) is defined by the minimization of the length functional

$$u(\gamma) = \int_0^1 \langle T(t), T(t)\rangle^{\frac{1}{2}}\, dt, \tag{2.3}$$

where $\gamma : [0,1] \to M$ is a curve with fixed endpoints, $\gamma(0) = p$, $\gamma(1) = q$, $T = \gamma' = d\gamma/dt$, and the inner product is given by the Riemannian metric (letting $g(x)$ and T_xM denote the Riemannian metric and tangent space at a point $x \in M$, respectively). The inner product between two tangent vectors $v, w \in T_xM$ is given by $\langle v, w\rangle = v^t g(x) w$.

As shown in [88], a critical curve for (2.3) is also a critical curve for

$$E(\gamma) = \int_0^1 \langle T(t), T(t)\rangle\, dt, \tag{2.4}$$

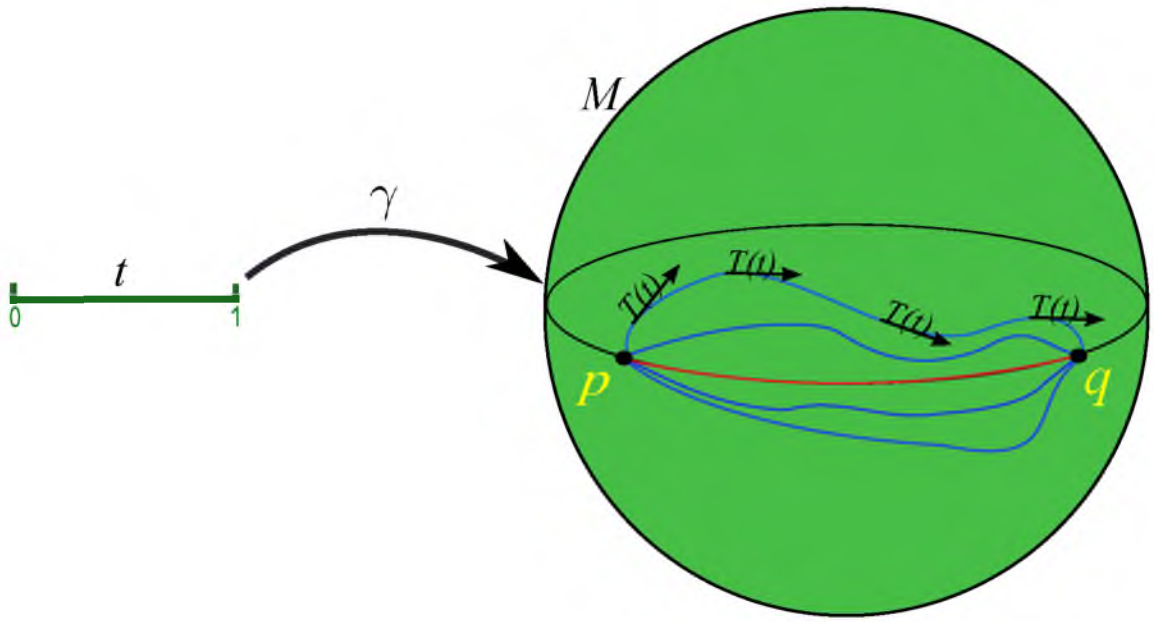

Fig. 2.14. Demonstration of a geodesic. The red curve is the one with minimum length.

and it is easier to work on the critical curves of (2.4). The only difference is that the geodesic that minimizes (2.4) has a constant speed.

As we know, for a functional, $F(f) = \int_a^b L(t, f(t), f'(t))dt$, where L and f are any functions, its critical points satisfy the following equation, called the Euler–Lagrange equation,

$$\frac{\partial L}{\partial f} - \frac{d}{dt}\frac{dL}{df'} = 0.$$

Equation (2.4) can be rewritten in the following form

$$E(\gamma) = \int_0^1 \langle T(t), T(t)\rangle \, dt = \int_0^1 \langle \gamma', \gamma'\rangle \, dt = \int_0^1 L(t, \gamma(t), \gamma'(t))dt.$$

So by computing the Euler-Lagrange equation of (2.4), a critical curve for E satisfies the following geodesic equation:

$$\frac{\partial^2 \gamma^k}{\partial t} = -\sum_{i,j} \Gamma_{ij}^k \frac{\partial \gamma^i}{\partial t}\frac{\partial \gamma^j}{\partial t},$$

which is equivalent to

$$\nabla_T T = 0,$$

where ∇ still is the Riemannian connection defined in Equation (2.2) and $T = d\gamma/dt$ is still the tangent vectors along the curve.

As we mentioned earlier, $\nabla_T T$ measures how the vector field X bends along its integral curves. In addition, it also means that tangent vectors, T, remain parallel if they are transported along the geodesic as shown in Fig. 2.15.

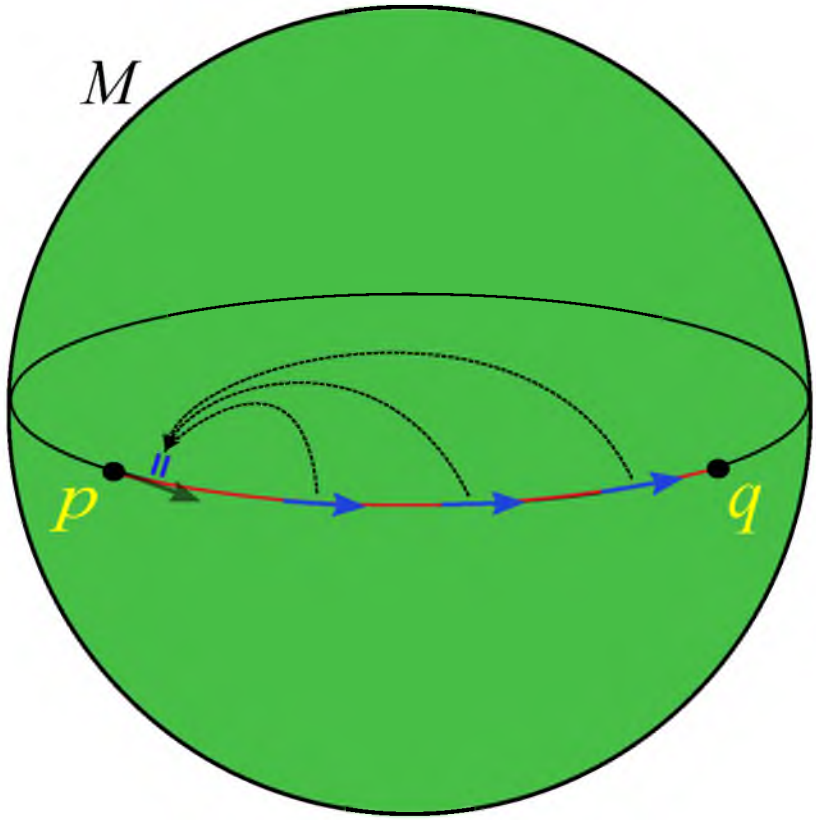

Fig. 2.15. Meaning of Riemannian connection $\nabla_T T = 0$.

2.4.3 Solve Eikonal Equation to Compute Geodesics

In this section, I will show that the geodesic $\gamma(t)$ minimizing $u(\gamma)$ in (2.3) also satisfies the Eikonal equation

$$\nabla u(\gamma)^T g^{-1}(\gamma) \nabla u(\gamma) = 1.$$

First, $u(\gamma)$ can be rewritten as

$$\int_0^1 \langle T(t), T(t) \rangle^{\frac{1}{2}} \, dt = \int_0^1 \sqrt{\gamma'(t)^T g(\gamma) \gamma'(t)} dt = \int_0^1 L(t, \gamma(t), \gamma'(t)) dt.$$

Then, the variation of $u(\gamma)$ is

$$\delta u(\gamma) = \frac{\partial L}{\partial \gamma'} \delta\gamma + \int_a^b (\frac{\partial L}{\partial \gamma} - \frac{d}{dt} \frac{\partial L}{\partial \gamma'}) dt$$

as shown in [53].

Since $\gamma(t)$ is a geodesic, $\frac{\partial L}{\partial \gamma} - \frac{d}{dt} \frac{\partial L}{\partial \gamma'} = 0$. Then,

$$\nabla u(\gamma) = \frac{\delta u(\gamma)}{\delta \gamma} = \frac{\partial L}{\partial \gamma'} = \frac{g(\gamma)\gamma'(t)}{\sqrt{\gamma'(t)^T g(\gamma) \gamma'(t)}}. \tag{2.5}$$

In addition, we can derive that

$$\nabla u^T(\gamma) g^{-1}(\gamma) \nabla u(\gamma) = \frac{\gamma'(t)^T g(\gamma)^T}{\sqrt{\gamma'(t)^T g(\gamma) \gamma'(t)}} g^{-1}(\gamma) \frac{g(\gamma)\gamma'(t)}{\sqrt{\gamma'(t)^T g(\gamma)\gamma'(t)}}$$
$$= \frac{\gamma'(t)^T g(\gamma)^T g^{-1}(\gamma) g(\gamma) \gamma'(t)}{\gamma'(t)^T g(\gamma)\gamma'(t)} = \frac{\gamma'(t)^T g(\gamma)^T \gamma'(t)}{\gamma'(t)^T g(\gamma)\gamma'(t)} = 1,$$

for $g(\gamma)$ is symmetric.

From (2.5), we can see that $\gamma'(t) \propto g^{-1}(\gamma)\nabla u(\gamma)$, for $\sqrt{\gamma'(t)^T g(\gamma)\gamma'(t)}$ is a scalar.

So, in the end, we get the following two equations

$$\nabla u(\gamma) g^{-1}(\gamma) \nabla u(\gamma) = 1 \tag{2.6}$$

$$\gamma'(t) \propto g^{-1}(\gamma)\nabla u(\gamma). \tag{2.7}$$

The two equations tell us that to reconstruct the geodesic $\gamma(t)$ between two points a and b on a Riemannian manifold, we can compute $u(\gamma)$ by solving the Eikonal equation (2.6) [53, 89] for u with the initial condition $u(a) = 0$. Then, compute $\gamma'(t)$ using (2.7) and integrate $\gamma'(t)$ backward from b to a to get the geodesic between the two points.

CHAPTER 3

ADAPTIVE RIEMANNIAN METRICS FOR IMPROVED GEODESIC TRACKING

In this chapter, we present a new geodesic approach for studying white matter connectivity from diffusion tensor imaging (DTI). Previous approaches have used the inverse diffusion tensor field as a Riemannian metric and constructed white matter tracts as geodesics on the resulting manifold. These geodesics have the desirable property that they tend to follow the main eigenvectors of the tensors yet still have the flexibility to deviate from these directions when it results in lower costs. While this makes such methods more robust to noise, it also has the serious drawback that geodesics tend to deviate from the major eigenvectors in high-curvature areas in order to achieve the shortest path. In this chapter, we formulate a modification of the Riemannian metric that results in geodesics adapted to follow the principal eigendirection of the tensor even in high-curvature regions. We show that this correction can be formulated as a simple scalar field modulation of the metric, and the appropriate variational problem results in a Poisson's equation on the Riemannian manifold. We demonstrate that the proposed method results in improved geodesics using both synthetic and real DTI data.

3.1 Introduction

Front-propagation approaches [47, 48, 50–52, 90] in diffusion tensor imaging (DTI) infer the pathways of white matter by evolving a level set representing the time-of-arrival of paths emanating from a starting region. The direction and speed of this evolving front at each point is determined by a cost function derived from the diffusion tensor data. One such method, first proposed by O'Donnell et al. [48], is to treat the inverse of the diffusion tensor as a Riemannian metric, and the paths in the propagating front as geodesics, i.e., shortest paths, under this metric. This makes intuitive sense: traveling along the large axis of the diffusion tensor results in shorter distances, while traveling in the direction of the small axes results in longer distances. Therefore, shortest paths will tend to prefer to remain tangent to the major principal eigenvector of the diffusion tensor. While this is a powerful

framework for computing white matter pathways, these geodesics have the serious deficiency that in high-curvature tracts they tend to deviate from the eigenvector directions and take straighter trajectories than is desired. That is, in high-curvature regions, the incremental cost of following the tensor field is overcome by the cost associated with the longer (more curved) path. In this chapter, we develop a new Riemannian metric that relies on diffusion tensor data but resolves this problem by adapting to high-curvature tracts, resulting in geodesic paths that more faithfully follow the principal eigenvectors.

As mentioned in Chapter 2, front-propagation methods offer several advantages over deterministic tractography [38, 40] and stochastic tractography [41–44]. For example, the front-propagation algorithms are more robust to noise because the wavefront is not constrained to exactly follow the principal eigenvector of the tensors. However, there is one serious drawback in front-propagation methods. Fig. 3.1 shows a diagram illustrating the problem. In a curved tensor field, one would typically prefer a path that follows, to whatever extent possible, the major eigenvectors of the tensors (shown in blue). The shortest path, using a Euclidean metric (i.e., ignoring the tensors) follows a straight line, except at constraints (shown in red). The typical geodesic with a local, anisotropic metric (e.g., using the inverse tensors as metric) will find a compromise between these two (shown in magenta). Although the magenta geodesic is taking infinitesimally higher-cost steps than the blue curve, its overall length under the inverse-tensor metric is shorter.

This issue has been addressed previously [52] by "sharpening" the tensor, i.e., increasing the anisotropy by taking the eigenvalues to some power and renormalizing them. The sharpening increases the cost of moving in directions other than the principal eigenvector. In fact, the first front-propagation algorithm proposed by Parker et al. [47] essentially takes this sharpening strategy to its limit, which results in a cost function that is the dot product of the level set velocity with the principal eigenvector. However, the amount of sharpening is an ad hoc parameter, and sharpening is applied equally across the image, rather than taking the curvature of the tract into account. Sharpening that increases with the curvature of the tract could be more effective. Another downside of sharpening is that it changes the shape of the tensor and reduces the ability to deviate from the principal direction, thus decreasing the desired robustness to noise. It is not clear how to set the amount of sharpening to find the best balance between robustness to noise versus faithful following of the eigenvectors.

Our proposed solution to this problem is to develop a new Riemannian metric that is a modulated version of the inverse diffusion tensor field. This metric is able to adaptively correct the geometry of geodesic curves in high-curvature regions so that they more closely

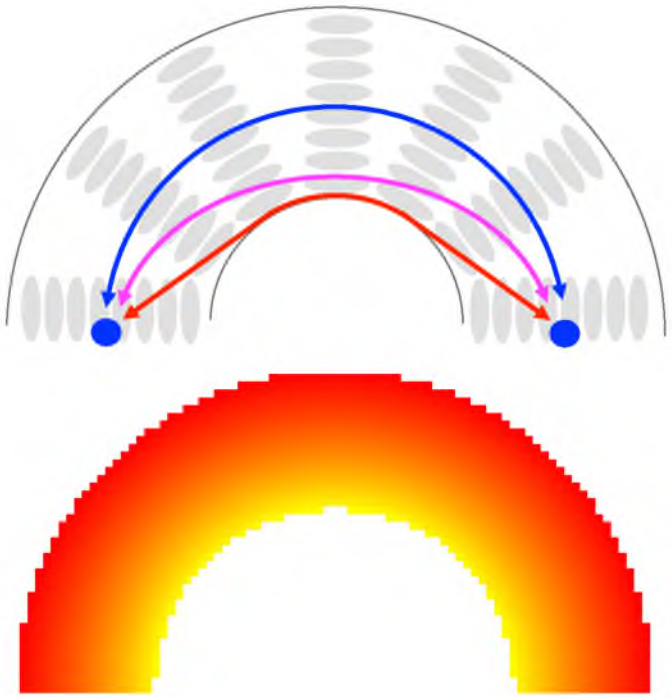

Fig. 3.1. High curvature tract deviation and our proposed solution. Top: Diagram of various pathways between two points in a curved tensor field: the desired path following the principal eigenvectors (blue), the shortest path under the Euclidean metric (red), and the compromise path taken when using the inverse tensor field as metric (magenta). Bottom: A slice of our $\alpha(x)$ solution for the synthetic data in Section 3.4.1 (Voxels are color coded from red [low value] to yellow [high value]).

follow the principal eigenvectors of the tensors. The resulting algorithm requires solving for an unknown scalar field (one example is shown in the bottom image of Fig. 3.1), which requires solving a Poisson equation on the Riemannian manifold—however, it does not require any arbitrary choice of parameters. We show that this solution is sufficient to eliminate the problem with geodesics in high-curvature regions described above and illustrated in Fig. 3.1, and we demonstrate the corrected behavior of geodesics on both synthetic and real DTI data.

3.2 Adaptive Riemannian Metrics

In this section, we derive a procedure for computing geodesic flows in diffusion tensor data that resolves the major drawback of front-propagation approaches outlined above. Namely, the geodesics generated by our method more closely conform to the principal eigenvector field. Rather than directly using the inverse of the diffusion tensor as the

Riemannian metric, as is typically done, we compute a spatially varying scalar function that modulates the inverse tensor field at each point and use this as our metric. We show that this scalar field can be chosen in such a way that the resulting geodesic flows have the desired property of following the eigenvector directions. This entails solving the classical variational problem for geodesic curves, with the exception that the Riemannian metric is scaled by a positive function. In the resulting Euler–Lagrange equation, we then solve for the particular scaling function that causes geodesics to follow the desired directions. In the end, we see that the appropriate function is computed by solving a Poisson equation on the Riemannian manifold.

3.2.1 The Metric Modulating Function

On a Riemannian manifold, M, the geodesic between two points $p, q \in M$ is defined by the minimization of the energy functional

$$E(\gamma) = \int_0^1 \langle T(t), T(t) \rangle \, dt,$$

where $\gamma : [0, 1] \to M$ is a curve with fixed endpoints, $\gamma(0) = p$, $\gamma(1) = q$, $T = d\gamma/dt$, and the inner product is given by the Riemannian metric. In our case the manifold $M \subset \mathbb{R}^3$ is the image domain, and the Riemannian metric can be equated with a smoothly varying, positive-definite matrix $g(x)$ defined at each point $x \in M$. Letting $T_x M$ denote the tangent space at a point $x \in M$, the inner product between two tangent vectors $u, v \in T_x M$ is given by $\langle u, v \rangle = u^t g(x) v$. As mentioned above, previous front-propagation approaches to DTI have used the inverse of the diffusion tensor field as a metric, i.e., $g(x) = D(x)^{-1}$ (or a sharpened or modified version), and this choice of metric leads to geodesics that bend inwards around curves. To rectify this problem, we will scale the Riemannian metric by a positive function $e^{\alpha(x)}$, which results in the new geodesic energy functional

$$E_\alpha(\gamma) = \int_0^1 e^{\alpha(\gamma(t))} \, \langle T(t), T(t) \rangle \, dt. \tag{3.1}$$

We call the function e^α the *metric modulating function* because it scales the Riemannian metric at each point. The exponentiation of α is to ensure that this scaling factor is positive and to make the solution to the variational problem come out simpler in the end. While it is possible to envision more complicated modifications of the metric tensor, we choose to modify the metric in this fashion for three reasons. First, the shape of the diffusion tensor provides information about the relative preference in diffusion directions, and a scaling operation allows us to keep this information intact. Second, the modification in (3.1) is sufficient to correct for the effects of curvature. In other words, if the tensors are following

a curved path, but not changing shape, the metric modulating function can be chosen in such a way that the resulting geodesics perfectly follow the principal eigenvector. We demonstrate this property empirically using a synthetic example in Section 5.3. Third, on a Riemannian manifold M, if there exist two Riemannian metrics g_1, g_2 satisfying $g_1 = fg_2$ for some positive function f on M, we call these two metrics conformally equivalent and the function f a conformal factor. So, our modulated Riemannian metric is a conformal transformation of an inverse-tensor metric, and the computed e^{α} can be seen as a conformal factor.

3.2.2 Computing the Geodesic Equation

To minimize the new geodesic energy functional given in (3.1), we use two tools of Riemannian geometry. The first is the Riemannian connection $\nabla_X Y$, which is the derivative of a vector field Y in the direction of a vector field X. We will write the vector fields X, Y in terms of a coordinate system $(x^1, x^2, \ldots, x^n)$; note that superscripts here are indices, not exponentiation. We write $X = \sum a^i E_i$ and $Y = \sum b^j E_j$, where $E_i = \frac{\partial}{\partial x^i}$ are the coordinate basis vectors, and a^i and b^j are smooth coefficients functions. Then the Riemannian connection is given by

$$\nabla_X Y = \sum_k \left(\sum_i a^i \frac{\partial b^k}{\partial x^i} + \sum_{i,j} \Gamma_{ij}^k a^i b^j \right) E_k.$$

The terms Γ_{ij}^k are the Christoffel symbols, which are defined as

$$\Gamma_{ij}^k = \frac{1}{2} \sum_{l=1}^{n} g^{kl} \left(\frac{\partial g_{jl}}{\partial x^i} + \frac{\partial g_{il}}{\partial x^j} - \frac{\partial g_{ij}}{\partial x^l} \right),$$

where g_{ij} denotes the entries of the Riemannian metric, g, and g^{ij} denotes the entries of the inverse metric, g^{-1}. Again, the intuition behind this Riemannian connection is that it is like a directional derivative of vector fields. In the special case of $Y = X$, $\nabla_X X$ measures how the vector field X bends along its integral curves.

The second tool that we employ is the Riemannian gradient of a smooth function f, which we denote $\operatorname{grad} f$. The gradient of a function on a Riemannian manifold looks like the standard Euclidean gradient, except with a multiplication by the inverse of the metric, i.e.,

$$\operatorname{grad} f = g^{-1} \left(\frac{\partial f}{\partial x^1}, \frac{\partial f}{\partial x^2}, \ldots, \frac{\partial f}{\partial x^n} \right).$$

The gradient is defined in this way so that the inner product with a unit vector u results in the usual directional derivative, $\nabla_u f = \langle \operatorname{grad} f, u \rangle$.

Using the Riemannian connection and Riemannian gradient, we take the variation of the energy (3.1). Let W be a vector field defined along the curve γ that represents an arbitrary perturbation of γ, keeping the endpoints fixed, i.e., $W(0) = W(1) = 0$. Notice that W and T are partial derivatives of the variation of γ, and therefore they commute, i.e., $\nabla_W T = \nabla_T W$. To simplify the notation, we will suppress the parameter t in most of the following equations. Then the variational of the energy functional is

$$\begin{aligned}
&\nabla_W E_\alpha(\gamma) \\
&\quad = \nabla_W \int_0^1 e^\alpha \langle T, T\rangle \, dt \\
&\quad = \int_0^1 \nabla_W e^\alpha \langle T, T\rangle dt \\
&\quad = \int_0^1 \nabla_W e^\alpha \cdot \langle T, T\rangle + e^\alpha \nabla_W \langle T, T\rangle \, dt \\
&\quad = \int_0^1 \langle W, \operatorname{grad} e^\alpha\rangle \cdot \langle T, T\rangle + 2e^\alpha \langle \nabla_W T, T\rangle \, dt \\
&\quad = \int_0^1 \langle W, \operatorname{grad} e^\alpha\rangle \cdot \|T\|^2 + 2 \langle \nabla_W T, e^\alpha T\rangle \, dt \\
&\quad = \int_0^1 \langle W, \operatorname{grad} e^\alpha\rangle \cdot \|T\|^2 + 2 \langle \nabla_T W, e^\alpha T\rangle \, dt \\
&\quad = \int_0^1 \left\langle W, e^\alpha \|T\|^2 \operatorname{grad} \alpha\right\rangle - 2 \langle W, \nabla_T (e^\alpha T)\rangle \, dt \\
&\quad = \int_0^1 \left\langle W, e^\alpha \|T\|^2 \operatorname{grad} \alpha - 2e^\alpha d\alpha(T) \cdot T - 2e^\alpha \nabla_T T\right\rangle dt.
\end{aligned}$$

Now, setting this last line to zero and dividing through by e^α results in the geodesic equation

$$\operatorname{grad} \alpha \cdot \|T\|^2 = 2\nabla_T T + 2d\alpha(T) \cdot T. \tag{3.2}$$

If we assume, without loss of generality, that geodesics have unit-speed parameterization, i.e., $\|T\| = 1$, then $\nabla_T T$ will be normal to T. Now, assuming this parameterization and taking the inner product with T on both sides of (3.2), we obtain

$$\langle \operatorname{grad} \alpha, T\rangle = 2d\alpha(T) = 2\langle \operatorname{grad} \alpha, T\rangle.$$

This can hold only if the tangential component $\langle \operatorname{grad} \alpha, T\rangle = 0$. Therefore, the last term in (3.2) must vanish, and we get the final, simplified geodesic equation

$$\operatorname{grad} \alpha = 2\nabla_T T. \tag{3.3}$$

3.2.3 Computing the Metric Modulating Function

Now that we have the geodesic equation for the modulated Riemannian metric, we introduce the property that we would like to enforce: that the tangent vectors, T, follow

the unit principal eigenvector directions, V. Satisfying this property directly would result in the equation $\operatorname{grad}\alpha = 2\nabla_V V$, which we would need to solve for α. However, given an arbitrary unit vector field V, there may not exist such a function with the desired gradient field.

Instead we minimize the squared error between the two vector fields, i.e., we minimize the functional

$$F(\alpha) = \int_M \|\operatorname{grad}\alpha - 2\nabla_V V\|^2 \, dx. \tag{3.4}$$

As before, the norm here is given by the Riemannian metric. The Euler–Lagrange solution to this problem is derived in the following derivation similarly to the classical Poisson equation,

$$\begin{aligned}
&\frac{dF(\alpha+\epsilon h)}{d\epsilon}\Big|_{\epsilon=0} \\
&= \frac{d}{d\epsilon}\int_M ||\operatorname{grad}(\alpha+\epsilon h) - 2\nabla_V V||^2 dx|_{\epsilon=0} \\
&= \frac{d}{d\epsilon}\int_M \langle \operatorname{grad}(\alpha+\epsilon h) - 2\nabla_V V, \operatorname{grad}(\alpha+\epsilon h) - 2\nabla_V V\rangle dx|_{\epsilon=0} \\
&= 2\int_M \langle \frac{d}{d\epsilon}\operatorname{grad}(\alpha+\epsilon h), \operatorname{grad}(\alpha+\epsilon h) - 2\nabla_V V\rangle dx|_{\epsilon=0} \\
&= 2\int_M \langle \operatorname{grad} h, \operatorname{grad}\alpha - 2\nabla_V V\rangle dx \\
&= -2\int_M \langle h, \operatorname{div}(\operatorname{grad}\alpha) - 2\operatorname{div}(\nabla_V V)\rangle dx \\
&\quad + \int_M \operatorname{div}(h\cdot(\operatorname{grad}\alpha - 2\nabla_V V))dx \\
&= -2\int_M \langle h, \Delta\alpha - 2\operatorname{div}(\nabla_V V)\rangle dx \\
&\quad + \int_{\partial M} h\cdot\langle \operatorname{grad}\alpha - 2\nabla_V V, \overrightarrow{n}\rangle dx.
\end{aligned}$$

The div operator used above is the Riemannian divergence, and the divergence of X on M is defined in coordinates as

$$\operatorname{div}(X) = \frac{1}{\sqrt{|g|}}\sum_i \frac{\partial}{\partial x^i}\left(\sqrt{|g|}a^i\right),$$

where $|g|$ is the determinant of the Riemannian metric, which represents the appropriate volume element. Finally, the equation of the metric modulating function that minimizes (3.4) is given by

$$\Delta\alpha = 2\operatorname{div}\left(\nabla_V V\right), \tag{3.5}$$

where $\Delta\alpha = \operatorname{div}(\operatorname{grad}\alpha)$ is the Laplace–Beltrami operator on M, defined as

$$\Delta(\alpha) = \frac{1}{\sqrt{|g|}} \sum_i \frac{\partial}{\partial x^i} \left(\sqrt{|g|} \sum_j g^{ij} \frac{\partial \alpha}{\partial x^j} \right)$$

in coordinates. From the boundary integral in the last step of the above derivation, the appropriate boundary conditions for this problem are the Neumann conditions,

$$\frac{\partial \alpha}{\partial \vec{n}} = \langle \operatorname{grad}\alpha, \vec{n} \rangle = \langle 2\nabla_V V, \vec{n} \rangle.$$

Finally, we solve (3.5) with the above boundary conditions to compute α for a data set, and the detailed implementation is discussed in Section 3.3. In the bottom image of Fig. 3.1, we show a slice of our α solution for the synthetic torus in Section 3.4.1. The voxels are color coded from red (low value) to yellow (high value), and we can see that the interior of the α field has a higher value than the exterior. Scaling the inverse tensor metric with e^{α} makes the geodesics follow the desired directions. This is because it has a higher cost for a pathway to travel along the interior of the torus than the exterior. In addition, the α field is consistent with equation $\operatorname{grad}\alpha = 2\nabla_V V$. As we mentioned earlier, $\nabla_V V$ measures how V is bending along its integral curve. Since V is rotating only in this case, the $\operatorname{grad}\alpha$ points inward to the torus center, which means α should increase as we move from the exterior of the torus to the interior. In another perspective, since the curvature is higher in the interior of the torus than the exterior, the α also penalizes higher curvature. The higher the curvature, the higher the α. This also happens on real data. For example, in the axial slice of the brain as shown in Fig. 3.2, we can see that the α is higher in the interior of the genu because the curvature is higher in the interior.

3.3 Numerical Implementation

A closer look at (3.5) reveals that it is nothing but an anisotropic Poisson equation on the image domain. The right-hand side is constant in α, and the Laplace–Beltrami operator on the left-hand side can be expressed as $\nabla \cdot (G\,\nabla\alpha)$, where G is a symmetric positive-definite matrix, $\nabla\cdot$ is the usual Euclidean divergence operator, and ∇ is the gradient operator in the image domain. Since the Poisson equation is on the image grid, we approximate both sides of the Poisson equation using a finite-difference approach.

It is common to use central, forward, or backward differences to approximate the first derivative. These techniques perform well on noiseless data, but they do not give adequate results on noisy data. We find that the computation of $\operatorname{div}(\nabla_V V)$ is sensitive to noise. So instead of using these differences, we use the noise-robust differentiator [91] as our

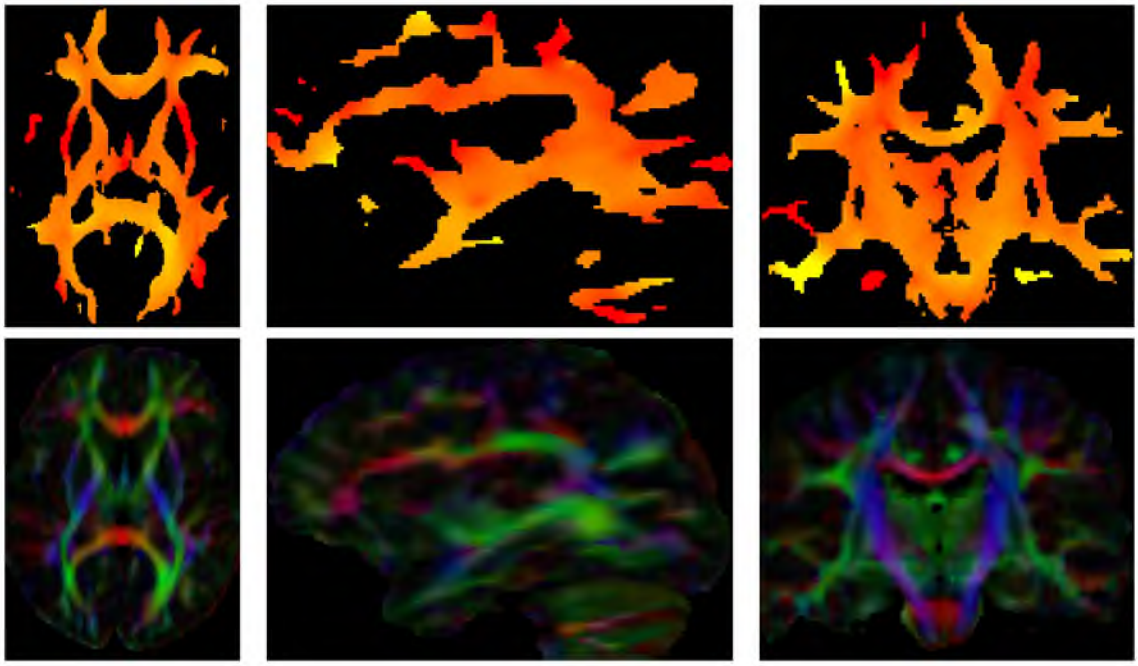

Fig. 3.2. Demonstration of the α solution. Top: Slices of the α solution for a read data in different views (Voxels are color coded from red [low value] to yellow [high value]). Bottom: Corresponding color-coded principal eigenvector image.

finite-difference approximation of the first derivative, which suppresses the high frequencies of the noise signal, is precise on low frequencies, and is particularly beneficial for noisy data.

Care must be taken to handle the sign ambiguity of the eigenvectors V when computing $\nabla_V V$. When we compute $\nabla_V V$ at a node, we need to make the eigenvectors around the node consistent. Our approach selects the eigenvector at the current node as a reference eigenvector and then chooses the directions that have a smaller angle with the reference eigenvector of the eigenvectors in the neighborhood. Remember that since $\nabla_V V = \nabla_{(-V)}(-V)$, it does not matter which direction the reference eigenvector points to of the two possible directions.

After the discretization of the Poisson equation with the Neumann boundary condition, we will get a sparse linear system $A \cdot \alpha = b$ to solve. For sparse linear systems, there are many efficient iterative solvers, such as conjugate gradient [92] (CG). However, CG can apply only to symmetric and positive-definite matrices or at least positive-semidefinite matrices. In our discretization, the Laplace-Beltrami operator A on the left-hand side is asymmetric due to the asymmetric interaction between g^{-1} and the computation of $\nabla\alpha$ in different neighborhoods, so we have to use other solvers that can be applied to asymmetric linear systems, such as the generalized minimal residual method [93] (GMRES) and biconjugate gradient method [94] (BICG). For BICG, we need to compute A^T, which is not trivial, so

we use GMRES as implemented in PETSc [95–97] library in our implementation.

GMRES solves a linear system by constructing a vector space with an orthonormal basis, and the solution can be written as the linear combination of the basis vectors. However, one drawback of the GMRES is that it also needs to save a certain number of basis vectors. In our real data study, to get a good solution, the GMRES usually runs hundreds of iterations, and we need to save several hundreds of basis vectors. Each basis vector usually requires tens of megabytes of memory, which means we need at least several gigabytes of memory. However, the amount of memory usage and computing time depend on the number of iterations, and we can reduce the number of iterations by using a good initialization of α. Our initialization of α is computed by minimizing the L_2 norm of the difference between $\nabla\alpha$ and $2\nabla_V V$, i.e., we will minimize

$$\int \|\nabla\alpha - 2\nabla_V V\|^2 \, dx$$

by solving the Euclidean Poisson equation

$$\Delta\alpha = 2\,\mathrm{div}\left(\nabla_V V\right),$$

where $\Delta\alpha = \mathrm{div}(\nabla\alpha)$ is the Laplace operator and div is just the Euclidean divergence. The reason we choose this initialization is that the Euclidean Poisson equation with Neumann conditions can be easily discretized to a symmetric positive definite linear system, which can be solved using CG efficiently in terms of both memory requirements and computing time. With the good initialization, we usually need tens of iterations instead of hundreds of iterations till the GMRES converges, and we have to save only tens of basis vectors. In our real data study, if we use the GMRES with the good initialization, the total cost is about 2 gigabytes of memory and 5 minutes instead of more than 10 gigabytes of memory and 40 minutes while using the GMRES with zero initialization.

3.4 Results

In this section, we demonstrate the improvement of geodesic flows generated by our metric modulating method compared to flows computed with the inverse-tensor metric and the sharpened-tensor metric [52] using both synthetic and real DTI data. Our measure of quality is how well the geodesics from the three methods follow the principal eigenvectors of the noise free tensors. However, as mentioned in Section 4.2, front-propagation methods do not explicitly compute the geodesic curves, but instead compute a function $u(x)$, which is the time-of-arrival of the geodesic flow at point x. The characteristic vectors of $u(x)$ give the tangent vectors along the geodesic. In the case of the inverse-tensor metric, $D(x)^{-1}$, the

characteristic vectors are given by $T(x) = D(x)\nabla u(x)$. In the case of the sharpened-tensor metric, the characteristic vectors are given by $T(x) = M(x)\nabla u(x)$, where

$$M(x) = |D(x)|^{\frac{1}{3}} \left(\frac{D(x)}{|D(x)|^{\frac{1}{3}}} \right)^{\beta}. \tag{3.6}$$

We demonstrate the changes of the sharpened diffusion tensor in Fig. 3.3, and we use $\beta = 3$ in all our experiments. In the case of our adaptive metric, the characteristic vectors are given by $T(x) = e^{-\alpha(x)} D(x)\nabla u(x)$. Here $\nabla u(x)$ indicates the Euclidean gradient, which we approximate with finite differences, as described in [49].

We compute $u(x)$ by solving a Hamilton–Jacobi equation using the Fast Iterative Method, as described in [52]. For visualization purposes, we compute the geodesics from both methods by integrating their characteristic vectors. Because these vectors always point away from the source region, we compute geodesic curves by integrating the characteristic vectors backward from any target point in the tensor field. These integral curves of the negative characteristic vectors are guaranteed to end up in the source region.

In the following sections, we first validate our adaptive Riemannian metric on clean synthetic data in Section 3.4.1 and on noisy synthetic data in Section 3.4.2.

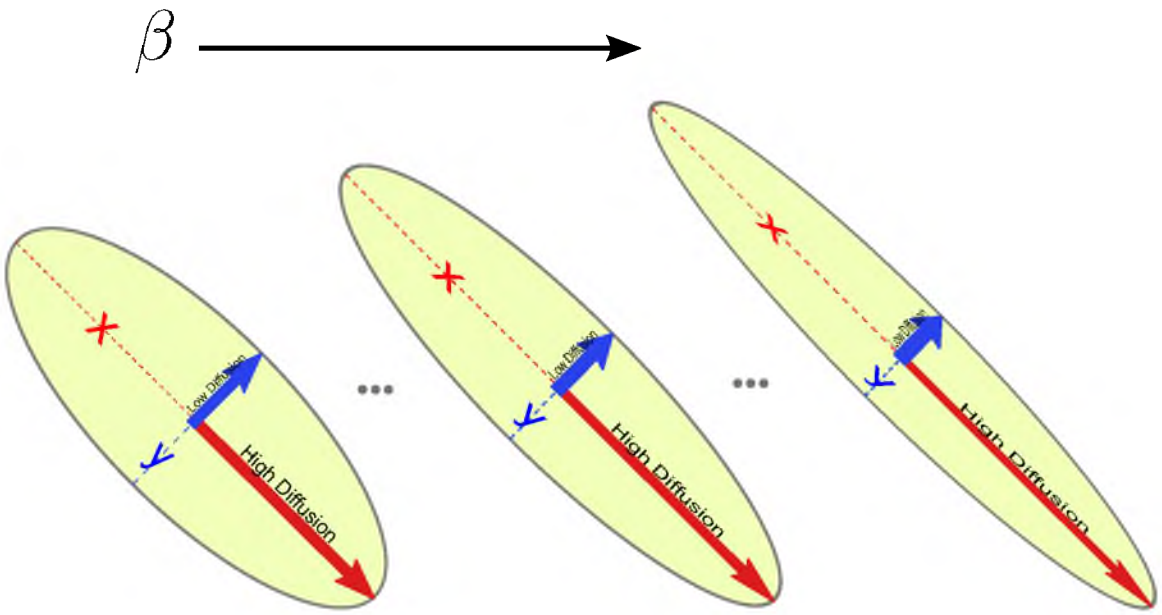

Fig. 3.3. The changes of the sharpened diffusion tensor M as β increases.

3.4.1 Clean Synthetic Curved Tensor Data

To test our method, we generate a synthetic curved tensor field that has similar properties to many white matter tracts in the brain. The synthetic data is the top half of a solid torus, where the tensors rotate along the large circle of the torus. The torus has a minor radius of 8 voxels and a major radius of 40 voxels. Each tensor in the tensor field has the same eigenvalues $(16,4,4)\times 10^{-4}\text{mm}^2/\text{s}$. A middle slice of the tensor field is shown in the first column of Fig. 3.4. The source region for the front-propagation method is shown in white.

In the left column of Fig. 3.4, we compare the characteristic vector field (shown in blue) of the generated noise-free data with the principal eigenvector field (shown in red).

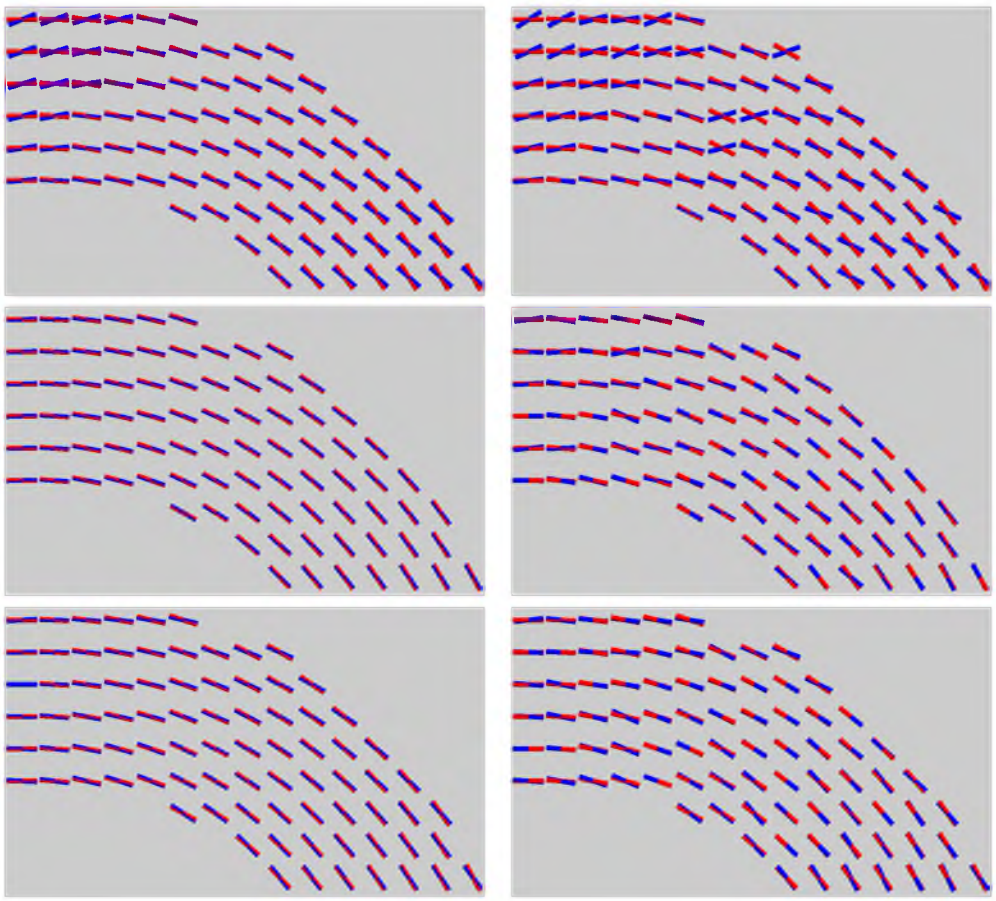

Fig. 3.4. Tangent vectors of the geodesics (blue) of the generated noise-free data (left column) and noisy data at a SNR of 15 (right column) under the inverse-tensor metric without modulation (top row), sharpened tensor metric (middle row), and with our modulation (bottom row). The red vectors are the principal eigenvectors of the diffusion tensors. We subsample the vector field by a factor of 4 both horizontally and vertically in order to visualize it.

Comparing the three images, we can clearly see the characteristic vectors T follow the principal eigenvectors V much better in the middle and bottom images. We do not show the vectors at the boundary of the white matter, for some characteristic vectors are pointing outwards because of the aliasing artifacts [54], and we will use this convention in the following descriptions.

In this synthetic example, we can compute the analytic solution of $\alpha(x)$, which is $\alpha(x) = -2\ln r(x) + C$, where $r(x)$ is the distance from x to the center of the torus, and C is some constant. We computed the difference between our numerical solution and the analytic $\alpha(x)$, and the result was within numerical error. We also computed the root mean square error (RMSE) of the angles between the geodesic tangent vectors and principal eigenvectors. The RMSE for our adaptive metric is 1.62° compared to 12.21° for the inverse-tensor metric and 0.84° for the sharpened-tensor metric. Again, we did not count the angles at the boundary when we computed RMSE, and we will use this convention in the following descriptions.

In the left column of Fig. 3.5, we visualize the integrated geodesics of the generated noise-free data between some target points (on the right side of the torus) and the source region (shown in white). Under the sharpened-tensor metric and adaptive metric, the geodesics follow the principal eigenvectors of the tensor field and arrive at a point inside the source region. In contrast, the geodesics under the inverse-tensor metric without modulation, starting from the same target points, take a shortcut and end up at the closest point inside the source region by closely following the boundary constraints.

As shown in Fig. 3.4, the sharpened-tensor metric and our adaptive metric have better characteristic vector fields and geodesics than the inverse-tensor metric. The sharpened-tensor metric is even better than our adaptive metric in terms of RMSE of the angles as shown in Table 3.1. This makes sense as we make the tensor sharper by increasing β in (3.6), the cost of moving in directions other than the principal eigenvector will increase, and the geodesics will tend to follow the principal eigenvectors more closely. In the limit case, the geodesics will follow the principal eigenvectors perfectly. However, we do not want to let the geodesics follow the principal eigenvectors too closely on noisy data, for this would decrease the robustness of the front-propagation method to noise as we demonstrate in Section 3.4.2. Besides, the amount of sharpening is an ad hoc parameter and even if there exists an optimal amount of sharpening, it is not clear how to compute this optimal value.

3.4.2 Noisy Synthetic Curved Tensor Data

To test the robustness of our method, we simulate Rician noise on the clean synthetic data we generated in Section 3.4.1, with a signal-to-noise ratio (SNR) of 10, 15, and 20. To

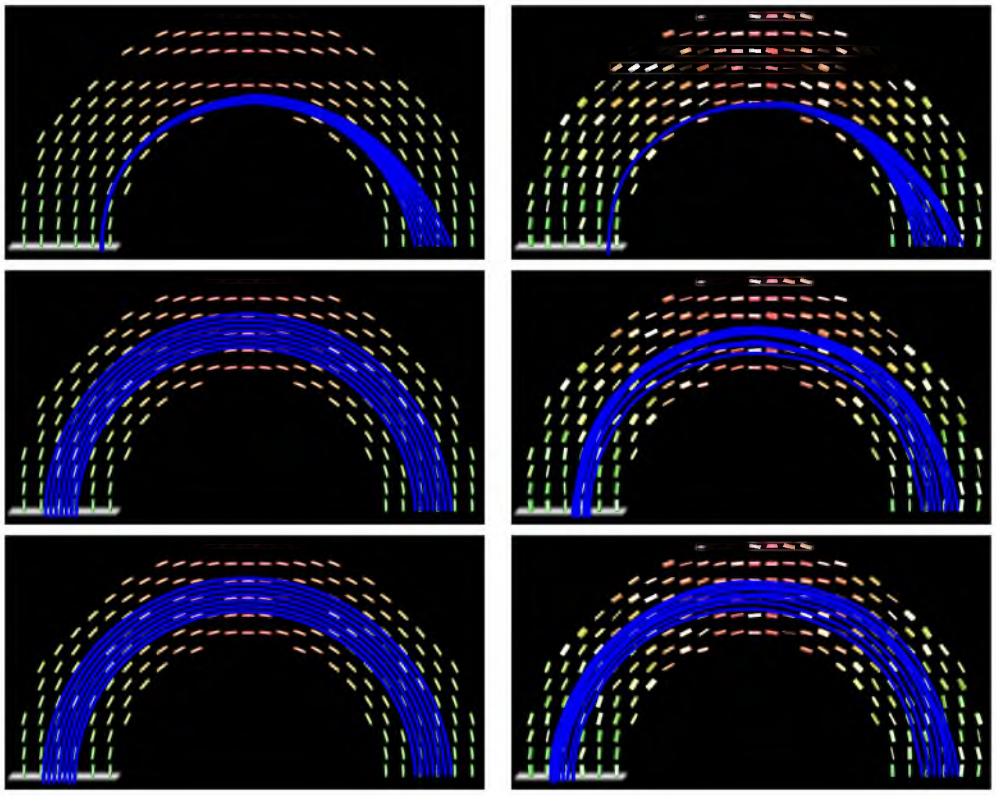

Fig. 3.5. The geodesics of the generated noise-free data (left column) and noisy data at a SNR of 15 (right column) emanating from the targets points (right side of the torus) to the source region (white). The order is the same as Fig. 3.4. We subsample the tensor field by a factor of 4 both horizontally and vertically in order to visualize it.

simulate Rician noise, we use the Stejskal–Tanner equation to generate 12 "clean" diffusion-weighted images (DWIs) with $b = 1000\text{s/mm}^2$ and one non-diffusion-weighted image. We then simulate Rician noise on each DWI and estimate the noisy synthetic tensor data.

We do the same comparison for the noisy synthetic data as we did for the clean synthetic data. In the right column of Fig. 3.4, we compare the characteristic vector field (shown in blue) of the generated noisy data at an SNR of 15 with the principal eigenvector field (shown in red) of the *clean synthetic data*. We can clearly see the characteristic vectors T follow the principal eigenvectors V much better for the sharpened-tensor metric and adaptive metric compared to the inverse-tensor metric, but we can also see some characteristic vectors T have a relative large angle with the principal eigenvectors V for the sharpened-tensor metric. Again, we compute the RMSE of the angles between the geodesic tangent vectors and clean principal eigenvectors. The RMSE for our adaptive metric is 5.94° compared to 16.35° for the inverse-tensor metric and 6.97° for the sharpened-tensor metric.

In addition, in Table 3.1, we can see that the RMSE of the angles between the geodesic tangent vectors and *clean principal eigenvectors* increases as the SNR decreases for all three metrics. Though our modulating metric has a somewhat larger RMSE than the sharpened-tensor metric on the clean data, our modulating metric always has the lowest RMSE on the noisy data.

In the right column of Fig. 3.5, we visualize the integrated geodesics of the generated noisy data at an SNR of 15 between a target region (on the right side of the torus) and a source region (shown in white). Under our adaptive metric, the geodesics follow the principal eigenvectors of the tensor field closely and arrive at a point inside the source region. In contrast, the geodesics under the inverse-tensor metric take a shortcut and end up at the closest point inside the source region by closely following the boundary constraints. The geodesics under the sharpened-tensor metric are better than the ones under the inverse-tensor metric, but are slightly worse than the ones under our adaptive metric.

3.4.3 Real Data

We now show the results of our method applied to a corpus callosum tract from a DTI of a healthy volunteer. DTI data were acquired on a Siemens Trio 3.0 Tesla Scanner with an eight-channel, receive-only head coil. DTI was performed using a single-shot, spin-echo, EPI pulse sequence and SENSE parallel imaging (undersampling factor of 2). Diffusion-weighted images were acquired in 12 noncollinear diffusion encoding directions with diffusion weighting factor b = 1000 s/mm^2 in addition to a single reference image (b = 0). Data acquisition parameters included the following: contiguous (no-gap) 50 2.5mm thick axial slices with an acquisition matrix of 128 x 128 over a FOV of 256 mm (2 x 2 mm^2 in-plane resolution), four averages, repetition time (TR) = 7000 ms, and echo time (TE) = 84 ms. Eddy current distortion and head motion of each data set were corrected using an automatic image registration program [98]. Distortion-corrected DW images were interpolated to 1 x 1 x 1 mm^3 voxels, and six tensor elements were calculated using weighted least squares. The

Table 3.1. The RMSE of the angles (in degrees) between the geodesic tangent vectors and *clean principal eigenvectors* under different metrics and different noise levels.

	No Noise	SNR 20	SNR 15	SNR 10
Inverse-tensor	12.21	15.76	16.35	18.35
Sharpened-tensor	0.84	5.31	6.97	10.70
Our adaptive	1.62	4.85	5.94	8.36

tensor upsampling is done only for the purposes of numerical computations on the voxel grid; a finer grid results in higher numerical accuracy.

In the left column of Fig. 3.6, we compare the characteristic vector field T (shown in blue) with the principal eigenvector field V (shown in red) of the corpus callosum. Both sharpened tensor and adaptive metrics result in characteristic vectors that tend to follow the main eigendirections better. We computed the RMSE of the angles between the geodesic tangent vectors and principal eigenvectors. The RMSE with our modulation is 9.31° compared to 17.74° without modulation and 7.28° with sharpened modulation. Note here that there is no ground truth, so a lower RMSE just gives a sense of how closely the characteristic vectors follow the noisy eigenvectors. As discussed earlier, following the principal eigenvectors too closely results in a decrease in robustness to noise.

In the right column of Fig. 3.6, as in the synthetic example, we track backward from target points (in the upper right side of the image) to a source region (upper left). Again, the geodesics under the inverse-tensor metric take a shortcut and merge into the closest point in the source region. In contrast, the geodesics under the sharpened-tensor metric and our adaptive metric more faithfully follow the tensor directions. Geodesics from our adaptive metric are drawn together slightly because the tensor field is thinner around the corner of the corpus callosum. The main paths of the adaptive metric and sharpened-tensor metric are similar, which is consistent with our Section 3.4.1 experiments on the synthetic torus without noise.

3.5 Conclusion

We presented a new geodesic front-propagation method for computing white matter pathways in DTI and showed that it results in geodesics that more faithfully follow the principal eigenvectors of the diffusion tensor field, especially in tracts with high curvature. Our method is formulated as a simple scalar field modulation of the Riemannian metric, and the appropriate variational problem results in a Poisson's equation on the Riemannian manifold. Furthermore, our method is less sensitive to local perturbations, such as noise, partial volume effects, or fiber crossing, compared to tractography algorithms. First, our adaptive metric is computed by minimizing functional (3.4), which makes our metric less sensitive to the noise as shown in Section 3.4.2. Second, the front-propagation method computes the pathways by optimizing a global functional using the whole DTI data and hence is less influenced by noise, partial volume effects, or fiber crossing.

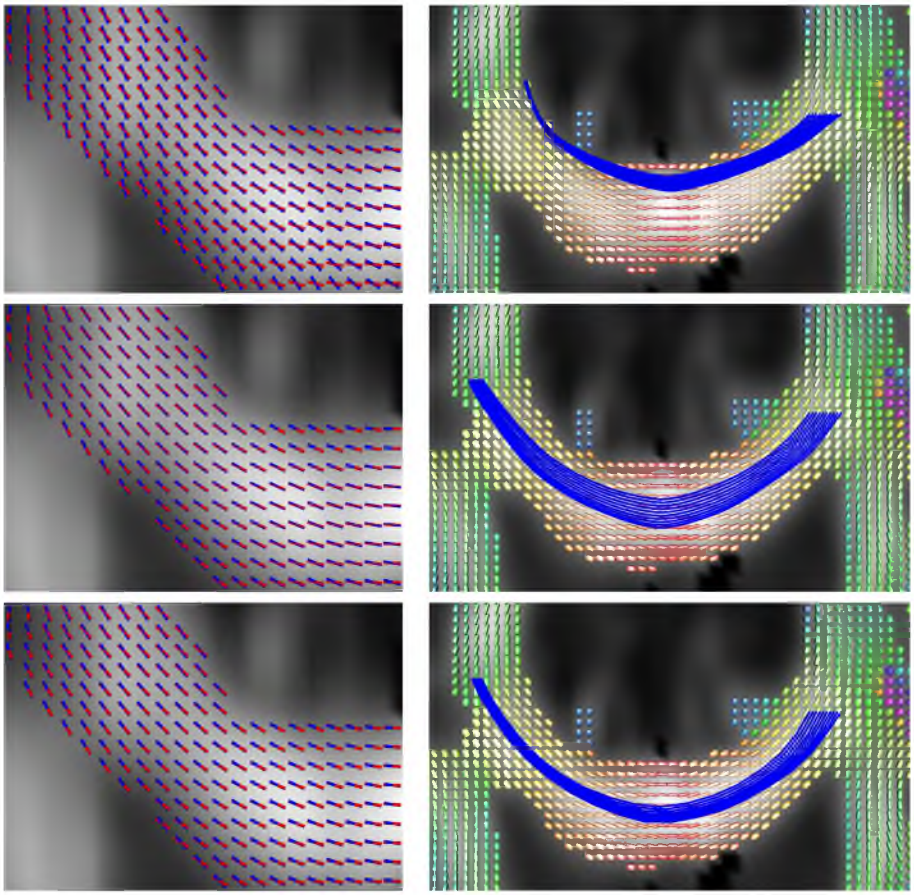

Fig. 3.6. Comparison of the tangent vectors and geodesics under different metrics. Left column: tangent vectors of the geodesics (blue) under the inverse-tensor metric (top), sharpened-tensor metric (middle) and our adaptive metric (bottom) for a part of the corpus callosum. The red vectors are the principal eigenvectors of the diffusion tensors. The FA image is shown in the background. Right column: the geodesic flow in the corpus callosum from the target points (in the left frontal forcep) to the source region (in the right frontal forcep). The background images are the FA image and the diffusion tensor field.

CHAPTER 4

BINARY SEGMENTATION OF WHITE MATTER TRACTS BASED ON GEODESIC TRACKING

We present a novel geodesic approach to segment white matter tracts from diffusion tensor imaging (DTI). Compared to deterministic and stochastic tractography, geodesic approaches treat the geometry of the brain white matter as a manifold. The white matter pathways are then inferred from the resulting geodesics. Previous methods have tried to threshold the cost of the geodesics to segment white matter tracts, but the segmentation is senstitive to the threshold value. In this chapter, we develop a way to automatically segment the white matter tracts based on the computed geodesics. We show the robustness of our method on simulated data with different noise levels. We also compare our segmentation method using adaptive Riemannian metrics as proposed in Chapter 3 with tractography methods and geodesic approaches using other Riemannian metrics and demonstrate that the proposed method results in improved segmentations using both synthetic and real DTI data.

4.1 Introduction

In order to study normal brain development, as well as neuropsychiatric disorders such as autism, it is crucial to understand how different functional regions of the brain are connected by white matter pathways. One approach to studying white matter in vivo is diffusion tensor imaging (DTI), which provides a means for inferring the microstructural properties of the white matter and analyzing fiber tracts. Three approaches to DTI analysis are whole-brain connectivity analysis, localizing white matter regions by registration to an atlas, and segmenting individual white matter tracts from specified regions of interest (ROI). In whole-brain connectivity analysis, the goal is to explore the connectivity among many anatomical regions over the whole brain, typically using tractography and graph statistics [26]. In atlas-based methods, the white matter is analyzed at the voxel level [99] or the atlas is used to segment the white matter into several anatomical tracts [100]. In

this chapter, we focus on segmentation of individual white matter tracts connecting two specified ROIs.

Several works have developed segmentation methods for white matter tracts from DTI data. Zhukov et al. [56] employed level-sets to create geometric models of brain structures. Rousson et al. [57] extended region-based surface evolution to DTI. Lenglet et al. [58] modeled DTI data as multivariate Gaussian distributions and employed a level variational approach to segment the white matter structures. Wang and Vemuri [59] used the square root of the J-divergence as the distance of tensors in a region-based active contour model for DTI segmentation. Ziyan et al. [60] proposed a modified spectral clustering method to segment thalamic nuclei. Awate et al. [61] used a nonparametric model to get a fuzzy segmentation of the white matter tracts. Melonakos et al. [62] proposed a locally constrained Bayesian region growing approach based on a precomputed anchor path inside the white matter tract. Niethammer et al. [63] developed a segmentation framework for near-tubular white matter tracts through global statistical modeling and local reorienting of the diffusion orientation. These methods focus on segmenting the white matter tracts of interest from the tensor field, and they do not compute parameterized fiber pathways connecting the two end regions of the tracts. Tractography [38–46] and front-propagation [47–54] approaches, however, provide both a volumetric segmentation of the tract suitable for region-based analysis and a parameterization suitable for along-tract statistics [101]. In this chapter, we extend the front-propagation approaches and compare our approach to previous methods for front-propagation and tractography.

As mentioned in Chapter 2, deterministic tractography [38–40] computes streamlines by forward integration of the principal eigenvector of the diffusion tensors from one region, but one major problem with tractography is that imaging noise causes errors in the principal eigenvector direction, and these errors accumulate in the integration of the streamlines. Stochastic tractography [41–46] is an approach that deals with the problems arising from image noise, but this is a computationally-intensive procedure (typically requiring several hours). In contrast, front-propagation approaches infer the pathways of white matter by first evolving a level set, $u(x)$, representing the time-of-arrival of paths emanating from some starting region. Then the pathways are computed by integrating the characteristics vectors of the level set backward from any target point to the starting region [49].

To segment a white matter tract, as shown in Fig. 4.1, Fletcher et al. [52] proposed the idea of first defining two ROIs at each end of the tract and then thresholding the addition $u(x) = u_1(x) + u_2(x)$ with a threshold ϵ, where $u_1(x)$ and $u_2(x)$ are the two cost functions

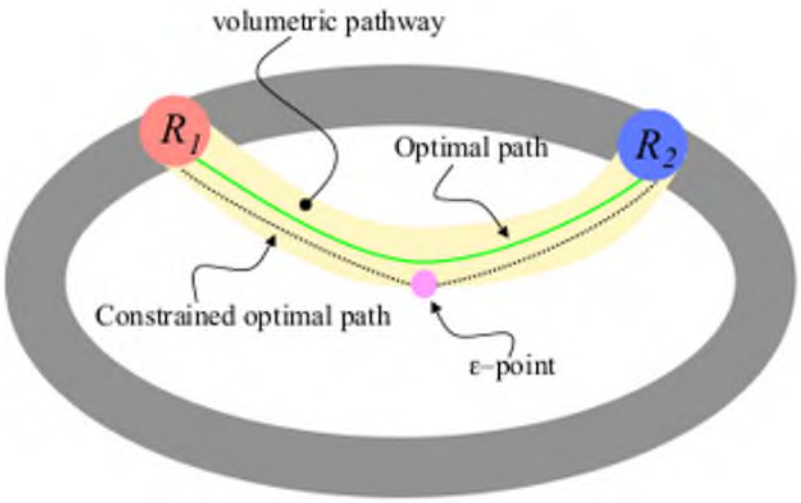

Fig. 4.1. Image is from [52]. The volumetric pathway is segmented by thresholding u with a threshold ϵ, where $u = u_1 + u_2$, and u_i is the time-of-arrival function from starting region R_i.

from the two ROIs. In Fig. 4.2, we show an example of $u_1(x)$, $u_2(x)$, and $u(x)$.

This threshold ϵ, however, is preset and the segmentations of white matter tracts vary hugely with the changes of the threshold ϵ. In Fig. 4.3, we show a slice of the thresholeded genu tract with ϵ equals to 0.03, 0.04, and 0.05. We can see that the segmentations vary excessively. As ϵ increases, part of the segmentation starts to oversegment the tract while some other parts still undersegment the tract. So it is tricky to find a good threshold value.

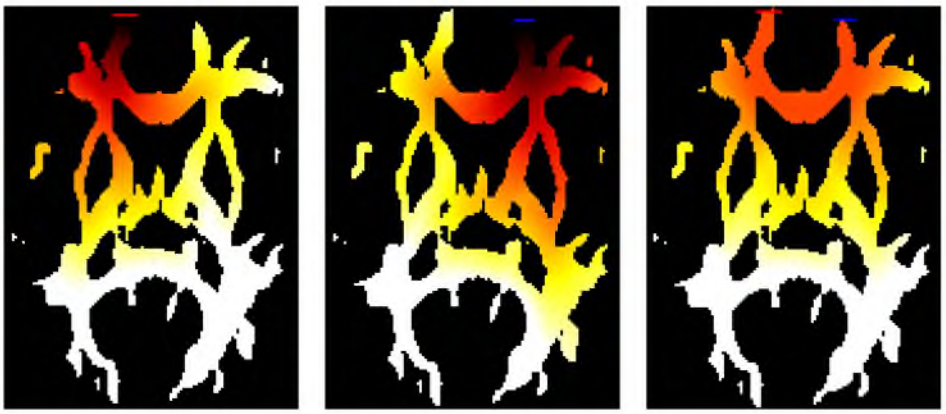

Fig. 4.2. The first/second image is the time-of-arrival function from starting region $R1/R2$, and the last image is the total cost image $u = u_1 + u_2$.

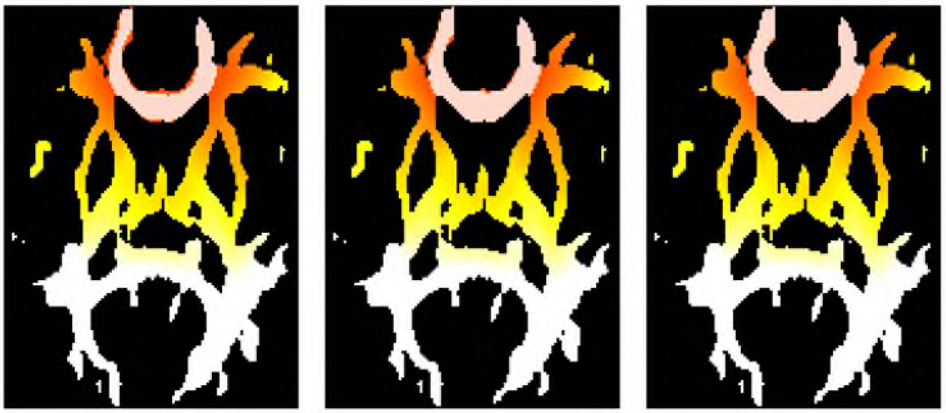

Fig. 4.3. White matter tracts that are segmented (white) by thrsholeding the total cost image with ϵ equals 0.03, 0.04, and 0.05.

Thus, users often need to manually adjust the threshold value, which is not only time consuming but also may reduce the reliability and repeatability of the segmentations. This issue is critical especially for longitudinal studies where we need to analyze the changes of a white matter tract over time and we want the segmentations of the white matter tract to be consistent for different time points. In this chapter, based on the angles of the geodesics from the two end regions of a white matter tract, we develop an automatic segmentation framework resulting in segmentations that better delineate the white matter tracts and without requiring the users to tune parameters or other kinds of user intervention. We also show the improvements of segmentations of the white matter tracts on both synthetic and real data (in Section 5.3).

4.2 Automatic Segmentation of White Matter Tracts

Front-propagation methods do not explicitly compute the geodesic curves, but instead compute a cost function $u(x)$, which is the time-of-arrival of the geodesic flow at the point x. The characteristic vectors of $u(x)$ give the tangent vectors along the geodesic, and the characteristic vectors are given by $T(x) = g(x)^{-1}\nabla u(x)$, where $g(x)$ is the Riemannian metric and $\nabla u(x)$ indicates the Euclidean gradient.

In this section, we propose to segment a white matter tract based on the angles of the two characteristic vector fields from the two ROIs (see Fig. 4.4). Intuitively, the characteristic vectors from the two ROIs would tend to point against each other inside the white matter tract and tend to point to similar directions outside the tract. In theory, for each point on the Riemannian manifold, there must exist a geodesic from each ROI to the point, which

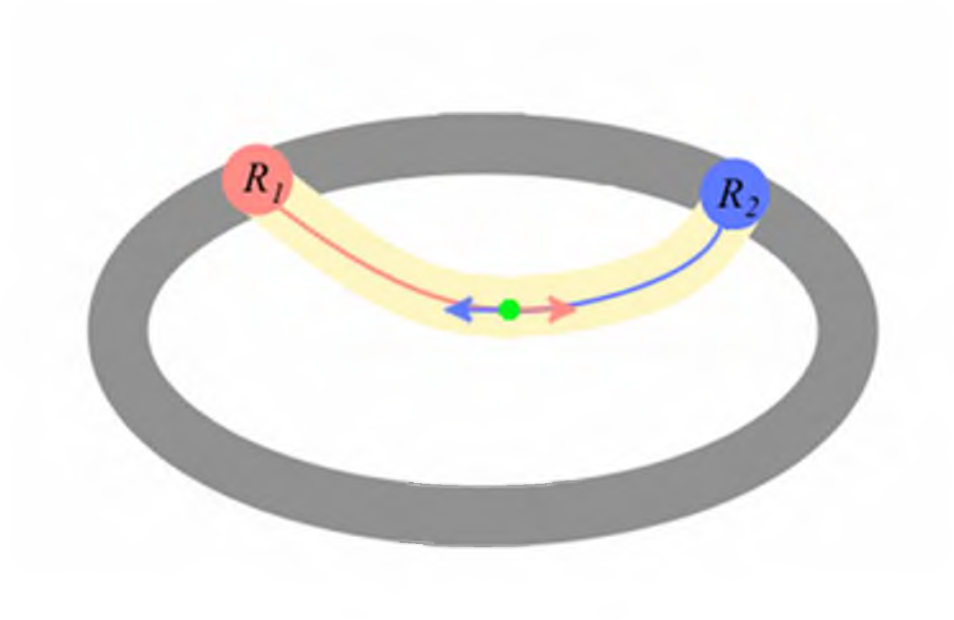

Fig. 4.4. The characteristic vectors from the two ROIs would tend to point against each other inside the white matter tract.

means we have two characteristic vectors at each point. If the point is on a geodesic from one ROI to the other ROI, as shown in the second image of Fig. 4.5, the two characteristic vectors must point to opposite directions, though in practice, we do not require that the two characteristic vectors be exactly opposite but have a large angle. When we compute the angle image of the two characteristic vector fields, since some characteristic vectors are pointing outwards at the boundary of the white matter boundary [54], we apply a median filter to the angle image to fix this artifact.

In order to segment the tract, we propose to threshold the angle image of the two characteristic vector fields. In addition, we do not want to manually set this threshold, as this may introduce reliability issues across different subjects or time points. Rather, we want to use an algorithm for automatically finding the optimal threshold for the angle image. Since the boundary of the tract of interest is very clear in the angle image (one example is shown in the second image of Fig. 4.5), we propose to use Otsu's method [102] to automatically segment the tract from the white matter.

Otsu's method automatically thresholds a gray-level image to a binary image by calculating the optimal threshold that minimizes the within-class variance

$$\sigma_w^2(t) = \omega_1(t)\sigma_1^2(t) + \omega_2(t)\sigma_2^2(t),$$

where $\omega_1(t)$ and $\omega_2(t)$ are the probabilities of the two classes thresholded by t, which are

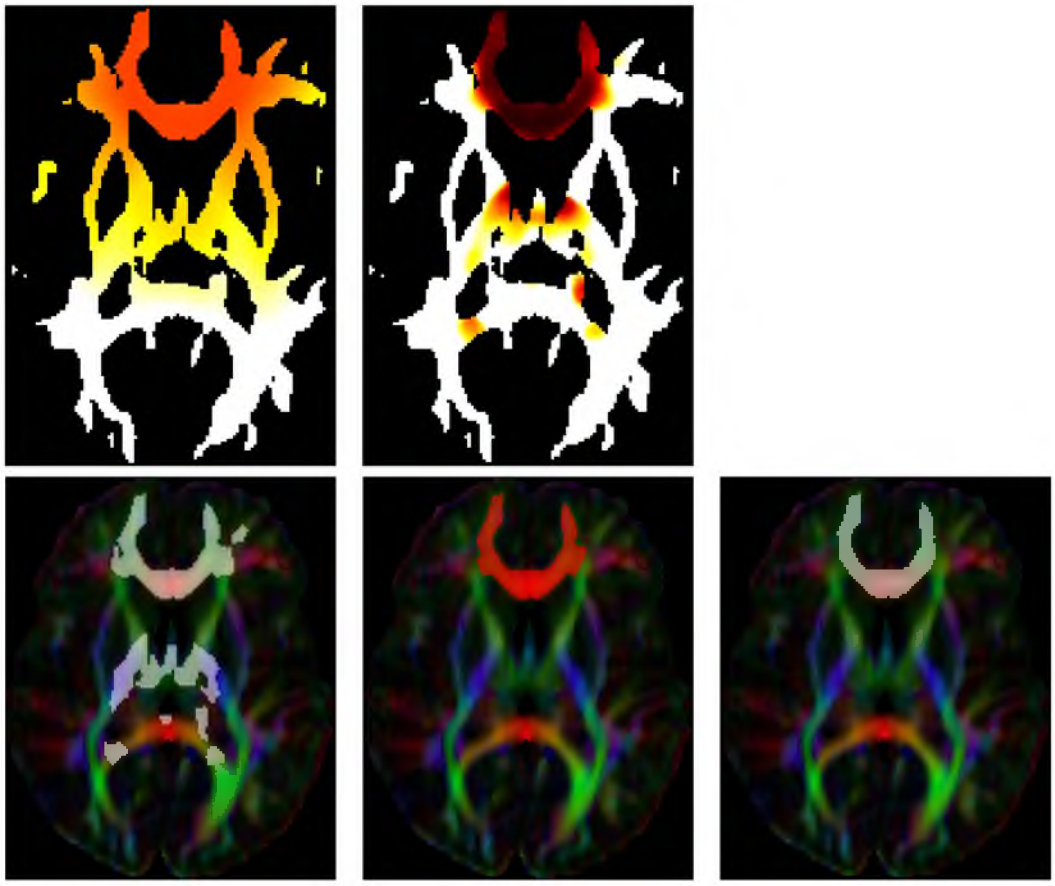

Fig. 4.5. From left to right, top to bottom: A slice of the cost image $u(x)$; the angle image between two characteristic vector fields, voxels colors are from white (small angle) to red (large angle); result of Otsu's thresholding directly on the angle image (shown in white); result of 95% thresholding of the cost image $u(x)$ (shown in red); and result of Otsu's thresholding of the angle image from the 95% thresholded region.

computed from the histogram, and $\sigma_1^2(t)$ and $\sigma_2^2(t)$ are the variance of the two classes. When the image to be thresholded contains two classes of voxels with well-separated intensity distributions, which holds for our angle images, Otsu's method performs well.

With Otsu's thresholding, we can segment the white matter tract of interest pretty well in most cases, but there is still an issue: the two characteristic vector fields sometimes could also meet at some white matter tracts other than the one of interest, and the segmented image would contains parts of some other white matter tracts (one example is shown in the third image of Fig. 4.5). In the case that these extra parts are not connected to the tract of interest, we can exclude these parts by choosing only the component containing the two ROIs using the connected component method. If these extra parts, however, are connected to the tract of interest, the connected component method does not help.

To resolve this issue, we introduce a step before the Otsu's thresholding. We propose to threshold the cost image $u(x)$ to the limit where all the voxels inside the ROIs are included in the thresholded region. We do this because more and more voxels inside the ROIs are included in the thresholded region as the threshold increases, and once all the voxels inside the ROIs are included, voxels that do not belong to the tracts will be included if we continue increasing the threshold. This threshold could be the max cost of all the voxels inside the two ROIs, but in case there are some outlier voxels inside the ROIs, we use the 95% largest cost of the voxels inside the two ROIs instead. Usually this thresholding of the cost image results in a region that is slightly larger than the tract of interest. One example is shown in the fourth image of Fig. 4.5. Though the choice of 95% threshold seems ad hoc and the increase of the threshold oversegments the tract of interest even more, our method is not sensitive to this specific threshold value. The reason is that the following Otsus thresholding of the angle image from the thresholded region reduces the amount of oversegmentation as shown in the last image of Fig. 4.5. Moreover, this thresholding strategy can be replaced with some outlier detection algorithms.

To summarize, our segmentation algorithm has two steps:

1. Segment a relatively small region containing the tract of interest by automatically thresholding the cost image $u(x)$ as described above.
2. Based on the angle image, use Otsu's method to automatically segment the tract of interest from the thresholded region from step 1.

4.3 Results

In this section, we demonstrate the improvement of segmentations generated based on our metric modulating method compared to those computed with the inverse-tensor metric, the sharpened-tensor metric, the BF and multi-ROI approach, and stochastic tractography [45] using both synthetic and real data. The segmentation algorithms based on geodesic tracking are mentioned in Section 4.2. We also test the BF and multi-ROI approach because it increases the validity of tractography as shown in Huang et al. [103]. In this approach, a fiber is traced for all pixels in the image, but only those fibers that penetrate the predefined ROIs are selected. Also, for a fair comparison with other segmentations, we truncate the selected fibers if they pass beyond the ROIs. For the deterministic tractography algorithm used in the BF + two-ROI approach, we test continuous tracking (FACT) [104] and tensor line [105] methods for both synthetic and real data. In addition, since we use a two-tensor model (4.1) to simulate several fiber crossing data in Section 4.3.1, we also do two-tensor estimation in the crossing regions and test two-tensor FACT and two-tensor

tensor line methods for the generated fiber crossing data. In the tractography algorithms used in our experiments, our step size is 0.1 of the slice thickness, and for the deterministic tractography algorithms, the streamline stops when the change of angle is larger than 75° during tracking. The stochastic tractography algorithm we used in our experiment is Bayesian tractography with 10,000 tracts initiated from each seed point. To compare with other two-ROIs approaches, we select only those fibers starting from one ROI passing through the other ROI, and the connectivity map is computed from the selected fibers. In addition, for quantitative validation purposes, we also truncate the selected fibers as mentioned earlier and threshold the connectivity maps with threshold value zero to get binary segmentations of the tracts. We use the implementation in Camino [106] library for the two-tensor estimation, deterministic tractography, and stochastic tractography.

In the following, we compare our segmentation method with other approaches and perform quantitative evaluation of the segmentations on synthetic data in Section 4.3.1. Then, we validate our adaptive Riemannian metric and segmentation method on real data in Section 4.3.2.

4.3.1 Fiber Crossing Tensor Data

To test the effectiveness of our segmentation algorithm presented in Section 4.2 on crossing tracts, we generate three fiber crossing tensor fields with similar properties to many white matter tracts in the brain. One goal of this experiment was to test the influence of oblate tensors, where the principal eigenvectors that our adaptive metric attempts to follow are not well defined. The synthetic images are two bars crossing at the center of the image at an angle of 60° and 90° and a curved torus crossing with a cylinder. The bar has a width of 8 voxels, the cylinder has a radius of 8 voxels, and the torus has a minor radius of 8 voxels and a major radius of 40 voxels. We show a center slice of each tensor field along with the ROIs we use in this experiment in the first column of Fig. 4.6.

The tensors in each tract of the two crossing tracts have eigenvalues $(16,4,4)\times 10^{-4}\text{mm}^2/\text{s}$. Each voxel of the generated DWI in the crossing area was computed based on the two-tensor model,

$$S = S_0(fe^{-bg^tD_1g} + (1-f)e^{-bg^tD_2g}), \tag{4.1}$$

where S_0 is the baseline image, g is the gradient direction, and D_1 and D_2 are the crossing tensors at a voxel. In this case, we use 64 gradient directions with $b = 1000\text{s/mm}^2$ and $f = 0.5$. In addition, the DWI was corrupted by Rician noise to simulate an SNR of 10, 15, and 20.

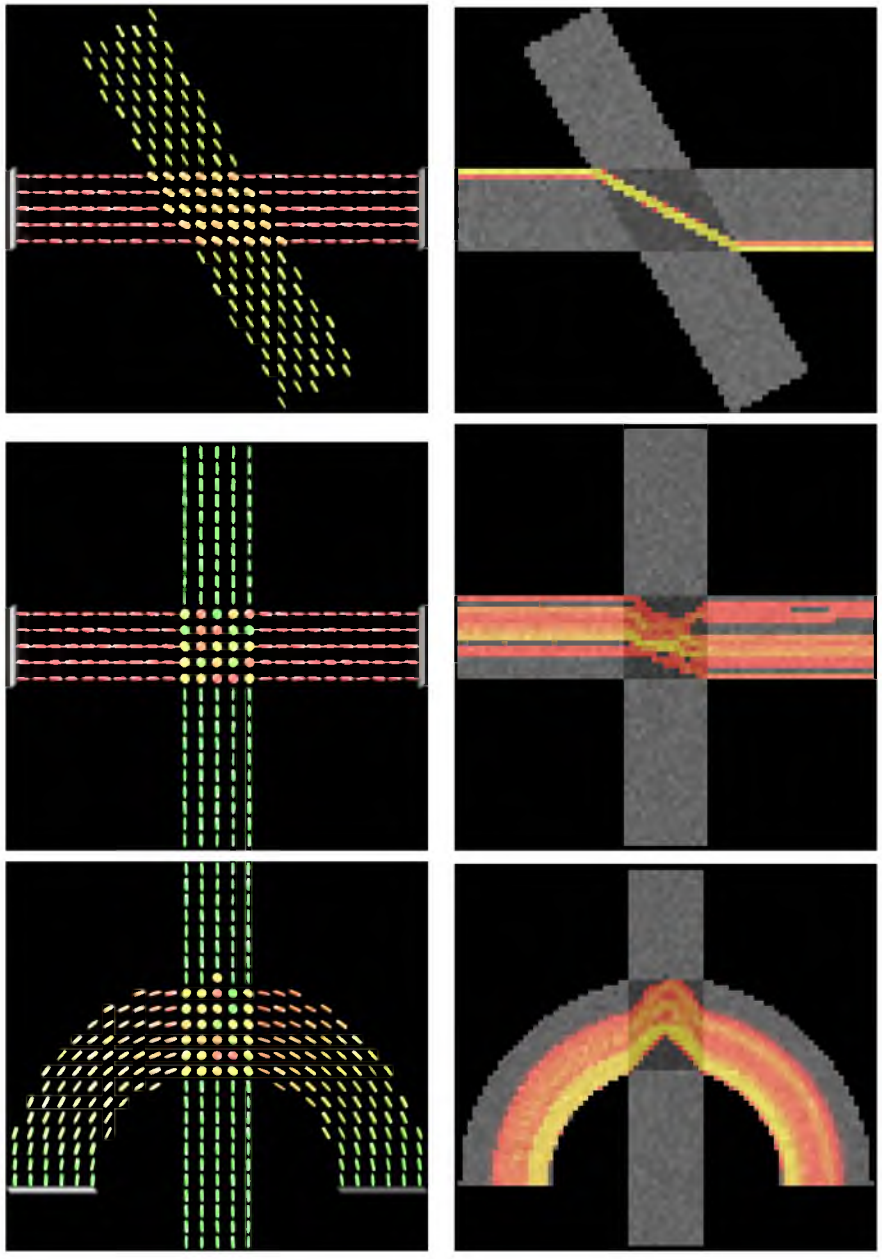

Fig. 4.6. Simulated fiber crossing data and the connection map from stochastic tractography. Left column: the simulated fiber crossing tensor fields with two ROIs (white and gray). We subsample the tensor field by a factor of 3 both horizontally and vertically in order to visualize it. Right column: the connection map (voxels are color coded from red [low intensity] to yellow [high intensity]) from stochastic tractography. The background image is the fractional anisotropy (FA) image.

In Tables 4.1 and 4.2, we compare the sensitivity, specificity, and Dice coefficient of the segmentations computed by eight methods. While the sensitivity and specificity represent only the true positive rate and the true negative rate of the segmentations, respectively, the Dice coefficient measures how similar the segmentations and the ground truth are overall. A segmentation with either a higher sensitivity or a higher specificity does not mean this segmentation is better. For example, on one hand, if a segmentation has every pixel, it will have sensitivity 1 and specificity 0; on the other hand, if a segmentation has no voxel, it will have sensitivity 0 and specificity 1, which is the case for the single-tensor FACT method in Table 4.2. So the Dice coefficient is of most interest and a high Dice coefficient should have both high sensitivity and high specificity.

From the two tables, we can see that it is very difficult for the single-tensor FACT and tensor line methods to pass the 60° crossing area. The stochastic tractography method works somewhat better, but its Dice coefficients are still low compared to our method. The major reason is that for these three methods, most of the fibers from one tract enter the wrong tract by following the ill-defined principal eigenvectors in the crossing region. The two-tensor methods perform much better than the single-tensor methods. For the 90° crossing data, most of the fibers of the single-tensor FACT method cannot pass though the crossing region because the principal eigenvectors are random at the crossing region, but the tensor line method works well because the tensors in the crossing region looks like pancakes and the fibers tend to go straight. The two two-tensor methods work better compared to the 60° crossing case, for the crossing angle is larger, which is easier for the two-tensor

Table 4.1. Quantitative evaluation (Dice, sensitivity and specificity) of the segmentations on the generated noisy data at an SNR of 10 based on 1) inverse-tensor metric, 2) sharpened-tensor metric, 3) our modulating metric, 4) single-tensor FACT BF + two-ROI, 5) single-tensor tensor line BF + two-ROI, 6) stochastic tractography, 7) two-tensor FACT BF + two-ROI, 8) two-tensor tensor line BF + two-ROI.

	60° Crossing			90° Crossing			Curved Crossing		
	Dice	SENS	SPEC	Dice	SENS	SPEC	Dice	SENS	SPEC
1	**0.997**	1	0.992	0.996	1	0.991	0.977	0.960	0.989
2	**0.997**	1	0.993	0.996	1	0.991	0.978	0.960	0.993
3	**0.997**	1	0.993	**0.997**	1	0.991	**0.993**	0.990	0.991
4	0.044	0.023	0.994	0.143	0.078	0.991	0.665	0.500	0.989
5	0.189	0.105	0.999	0.991	0.989	0.991	0.958	0.919	0.999
6	0.327	0.195	1	0.269	0.155	1	0.860	0.754	0.999
7	0.810	0.681	0.998	0.901	0.821	0.998	0.950	0.905	0.997
8	0.777	0.637	0.996	0.973	0.954	0.991	0.958	0.921	0.994

Table 4.2. Quantitative evaluation (Dice, sensitivity and specificity) of the segmentations on the generated noisy data at an SNR of 20 based on 1) inverse-tensor metric, 2) sharpened-tensor metric, 3) our modulating metric, 4) single-tensor FACT BF + two-ROI, 5) single-tensor tensor line BF + two-ROI, 6) stochastic tractography, 7) two-tensor FACT BF + two-ROI, 8) two-tensor tensor line BF + two-ROI.

	60° Crossing			90° Crossing			Curved Crossing		
	Dice	SENS	SPEC	Dice	SENS	SPEC	Dice	SENS	SPEC
1	**0.998**	1	0.996	**0.996**	1	0.991	0.977	0.958	0.992
2	**0.998**	1	0.996	**0.996**	1	0.991	0.977	0.959	0.992
3	0.997	1	0.992	**0.996**	1	0.991	**0.993**	0.990	0.992
4	0	0	1	0.030	0.015	1	0.705	0.544	0.999
5	0.053	0.027	1	0.991	0.991	0.989	0.952	0.908	0.998
6	0.204	0.124	1	0.536	0.366	1	0.882	0.790	0.997
7	0.929	0.872	0.993	0.949	0.907	0.995	0.967	0.939	0.992
8	0.845	0.749	0.995	0.982	0.974	0.987	0.968	0.941	0.992

estimation algorithm to separate the two tensors. For the image containing a curved tract crossing with a cylinder, the single-tensor FACT and stochastic tractography methods work better compared to the other two cases because the principal eigenvectors are not random except in the center slice of the crossing region, and most of the fibers do not go to the wrong tract by following the principal eigenvectors.

For the segmentations based on the geodesic tracking with three metrics, we can see that these three methods outperform the other five tractography algorithms and that the three methods have very similar Dice coefficients, which are all above 99%, for both 60° and 90° crossing. For the data where a curved tract crosses with a cylinder, although these three methods still outperform the other five tractography algorithms, the segmentations based on our modulating metric have the best Dice coefficient, and their differences from the Dice coefficients of the segmentations based on the other two metrics are greater.

Besides, the geodesic methods have very stable segmentations as the noise level changes, but the tractography methods are relatively more sensitive to noise. In addition, for different crossing data, the best tractography algorithm changes, so it is unclear how to choose the most appropriate tractography algorithm if we want to use tractography to segment tracts.

In Fig. 4.7, we show a slice of the segmentations using the best tractography methods (1st column) in terms of the Dice coefficient, using the sharpened-tensor metric (2nd column), and using our adaptive metric (3rd column). We can see that the segmentations based on our adaptive metric are favorable in all three cases. In the right column of Fig. 4.6, we show the connectivity maps of the stochastic tractography. We can see that the stochastic results miss numerous voxels that are inside the tract of interest.

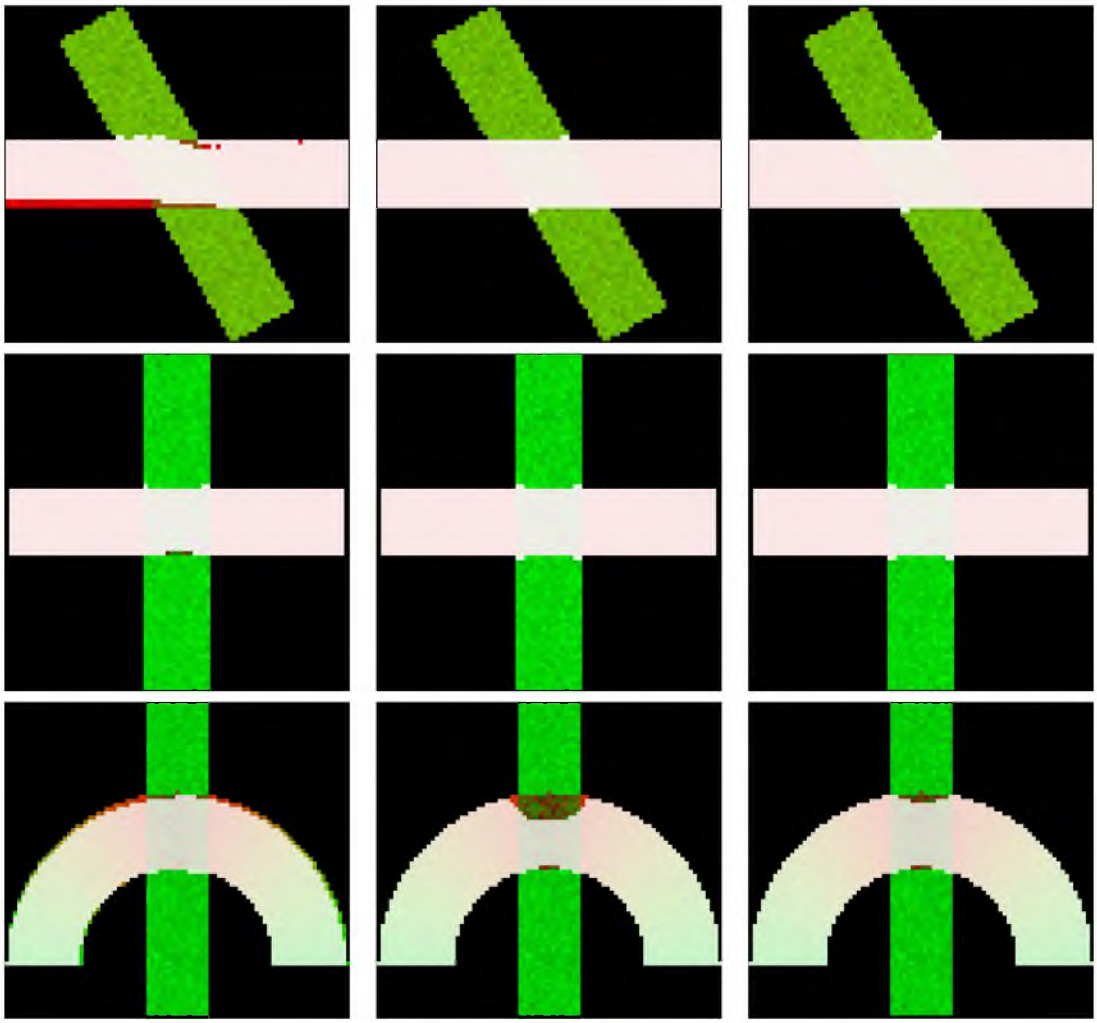

Fig. 4.7. A slice of the segmentations of the fiber crossing data at an SNR of 20. The first column show the best tractography results in terms of the Dice coefficient, which are two-tensor FACT BF + two-ROI method, single-tensor tensor line BF + two-ROI method, and two-tensor tensor line BF + two-ROI method from top to bottom. The second/third column shows the results based on the sharpened-tensor metric/our modulating metric.

4.3.2 Real Data

We now show the results of our method applied to DTI of 10 healthy volunteers. DTI data were acquired on a Siemens Trio 3.0 Tesla Scanner with an 8-channel, receive-only head coil. DTI was performed using a single-shot, spin-echo, EPI pulse sequence and SENSE parallel imaging (undersampling factor of 2). Diffusion-weighted images were acquired in twelve noncollinear diffusion encoding directions with a diffusion weighting factor b = 1000 s/mm^2 in addition to a single reference image (b = 0). Data acquisition parameters included the following: contiguous (no-gap) 50 2.5mm thick axial slices with an acquisition matrix of 128 x 128 over a FOV of 256 mm (2 x 2 mm^2 in-plane resolution), four averages, repetition

time (TR) = 7000 ms, and echo time (TE) = 84 ms. Eddy current distortion and head motion of each data set were corrected using an automatic image registration program [98]. Distortion-corrected DW images were interpolated to 1 x 1 x 1.25 mm^3 voxels, and six tensor elements were calculated using weighted least squares. The tensor upsampling is done only for the purposes of numerical computations on the voxel grid; a finer grid results in higher numerical accuracy.

We selected four white matter tracts—the uncinate fasciculus, genu, arcuate fasciculus, and corticospinal tracts—to validate our segmentation algorithm on the real DTI from 10 subjects. We compare the segmentations of different algorithms as we did in Section 4.3.1, except that we do not test the two-tensor methods since the diffusion-weighted images were acquired in only 12 diffusion encoding directions. To get a quantitative validation, we need the ground-truth segmentation on these real data, and for this we use the Johns Hopkins University DTI-based white matter atlases [107–109]. There is both a white matter labels atlas, created by hand segmentation, and a white matter tractography atlas, created by averaging the results of deterministic tractography. We first register each subject's DTI to their corresponding T2 images, and then we register the T2 image of the atlas to the T2 image of each subject. In the end, we use the computed deformation field to transform both labels to each of the 10 subject's anatomy. We then use these registered labels as a starting point for manual segmentations of the 10 images. This allowed for manual correction of segmentations due to anatomical variability and registration errors. Tables 4.3 and 4.4 give the Dice coefficients and specificity/sensitivity of all methods, compared to the manual segmentation ground truth.

In Tables 4.3 and 4.4, we can see similar behavior as we found in the segmentation

Table 4.3. Mean and standard deviation of segmentation metrics (Dice, sensitivity and specificity) for the uncinate fasciculus and genu from 10 subjects. Methods shown are 1) Inverse-tensor metric, 2) Sharpened-tensor metric, 3) Our modulating metric, 4) Single-tensor FACT BF + two-ROI, 5) Single-tensor Tensor line BF + two-ROI, 6) Stochastic tractography.

	uncinate			genu		
	Dice	SENS	SPEC	Dice	SENS	SPEC
1	0.793 (0.054)	0.720 (0.087)	0.999 (0)	0.706 (0.132)	0.625 (0.163)	0.993 (0.004)
2	0.829 (0.047)	0.800 (0.099)	0.999 (0)	0.726 (0.078)	0.637 (0.114)	0.993 (0.003)
3	**0.845** (0.036)	0.841 (0.044)	0.999 (0.001)	**0.745** (0.046)	0.709 (0.111)	0.988 (0.006)
4	0.460 (0.121)	0.401 (0.119)	0.998 (0.001)	0.628 (0.091)	0.511 (0.117)	0.994 (0.004)
5	0.545 (0.096)	0.506 (0.126)	0.998 (0.001)	0.698 (0.046)	0.599 (0.075)	0.993 (0.003)
6	0.469 (0.158)	0.341 (0.136)	0.999 (0.001)	0.613 (0.074)	0.474 (0.103)	0.996 (0.004)

Table 4.4. Mean and standard deviation of segmentation metrics (Dice, sensitivity and specificity) for arcuate fasciculus and corticospinal tract from 10 subjects. Methods shown are 1) Inverse-tensor metric, 2) Sharpened-tensor metric, 3) Our modulating metric, 4) Single-tensor FACT BF + two-ROI, 5) Single-tensor Tensor line BF + two-ROI, 6) Stochastic tractography.

	arcuate fasciculus			corticospinal tract		
	Dice	SENS	SPEC	Dice	SENS	SPEC
1	0.729 (0.052)	0.621 (0.074)	0.999 (0.001)	0.778 (0.050)	0.752 (0.089)	0.997 (0.001)
2	0.733 (0.045)	0.650 (0.080)	0.999 (0.001)	0.758 (0.050)	0.733 (0.088)	0.996 (0.001)
3	**0.750** (0.034)	0.687 (0.054)	0.998 (0.001)	**0.782** (0.041)	0.866 (0.049)	0.994 (0.002)
4	0.429 (0.107)	0.322 (0.094)	0.998 (0.001)	0.373 (0.120)	0.260 (0.098)	0.998 (0.001)
5	0.530 (0.110)	0.410 (0.112)	0.999 (0.001)	0.367 (0.095)	0.246 (0.083)	0.999 (0.001)
6	0.568 (0.123)	0.474 (0.122)	0.997 (0.003)	0.462 (0.098)	0.341 (0.095)	0.997 (0.002)

of synthetic data in Section 4.3.1. First, we can see that the tractography methods have difficulties in connecting two regions, especially in the presence of partial voluming or fiber crossing. For example, the Dice coefficients of tractography methods are all below 0.6 for the uncinate fasciculus, arcuate fasciculus, and corticospinal tract, where there are either fiber crossing or fiber kissing inside each tract. The tractography methods work better on the genu, in terms of Dice coefficients, because there are no fiber crossings inside this tract. In all four tracts, the front-propagation approaches perform better than the tractography methods in terms of Dice coefficients, with our adaptive metric performing the highest. For the corticospinal tract, compared to the other three highly curved tracts, the three different geodesic methods have very close Dice coefficients, and the one with our modulated metric does not improve the segmentation by much. This is consistent with what we found on the synthetic data, where the geodesic methods have similar Dice coefficients when the tracts are straight, and our adaptive metric is better when the tracts are curved.

In Figs. 4.8, 4.9, 4.10, and 4.11, we show slices of the ground-truth segmentations, the segmentations of the best tractography methods in terms of Dice coefficient, the connectivity map from stochastic tractography, and the segmentations based on geodesic tracking. We can see that in all cases, the BF + two-ROI methods tend to undersegment the white matter tracts. They often miss a lot of voxels that are obvious inside the tracts of interest. This is especially obvious in the segmentations of uncinate fasciculus (Fig. 4.11) and corticospinal tract (Fig. 4.10). These two methods can usually segment the central part of the tracts, but often miss voxels around the boundary of the tracts since the fibers passing these voxels are likely to stop at the boundary of the white matter or enter into other tracts because of partial voluming or fiber crossing. In addition, we can also see that the BF + two-ROI approach sometimes includes some voxels outside the tracts of interest. For example, in the

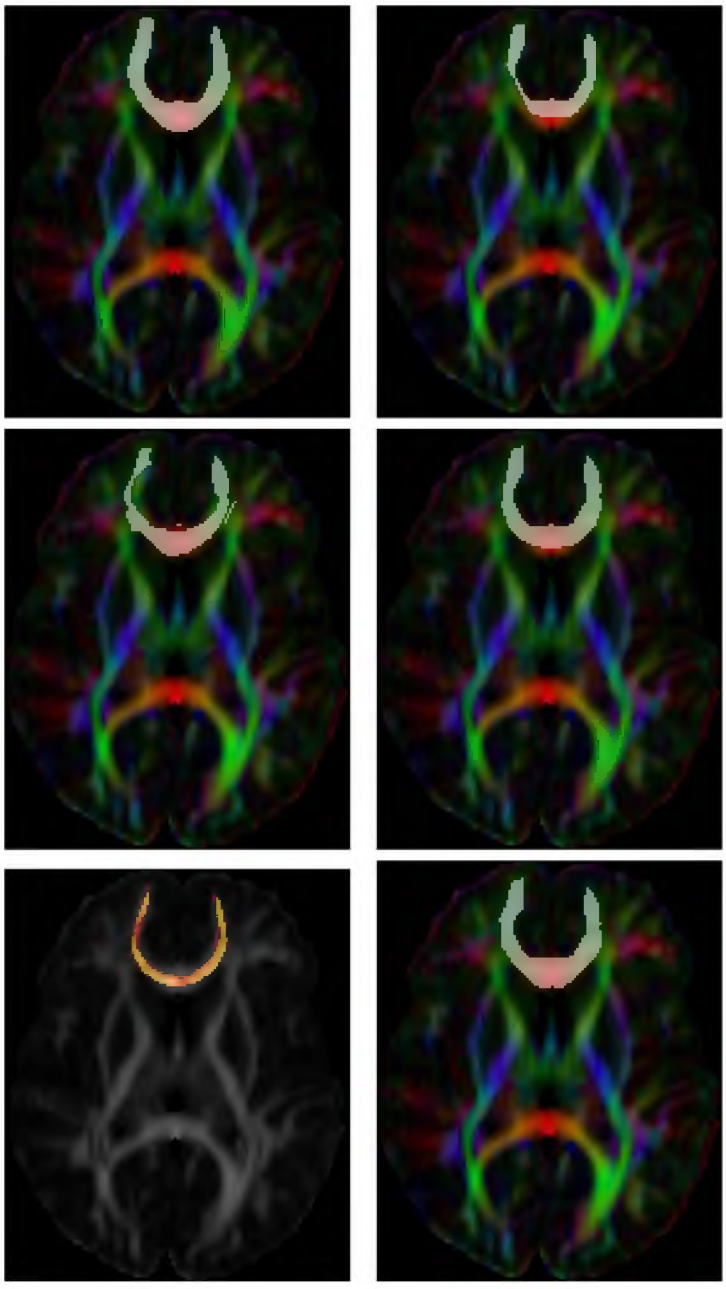

Fig. 4.8. A slice of segmentations (shown in white) and a connectivity map of the genu of the corpus callosum. Left column (from top to bottom): ground-truth segmentation, segmentation from single-tensor tensor line BF + two-ROI method, connectivity map from stochastic tractography; Right column (from top to bottom): segmentations based on geodesic tracking with the inverse-tensor metric, sharpened-tensor metric, and our adaptive metric.

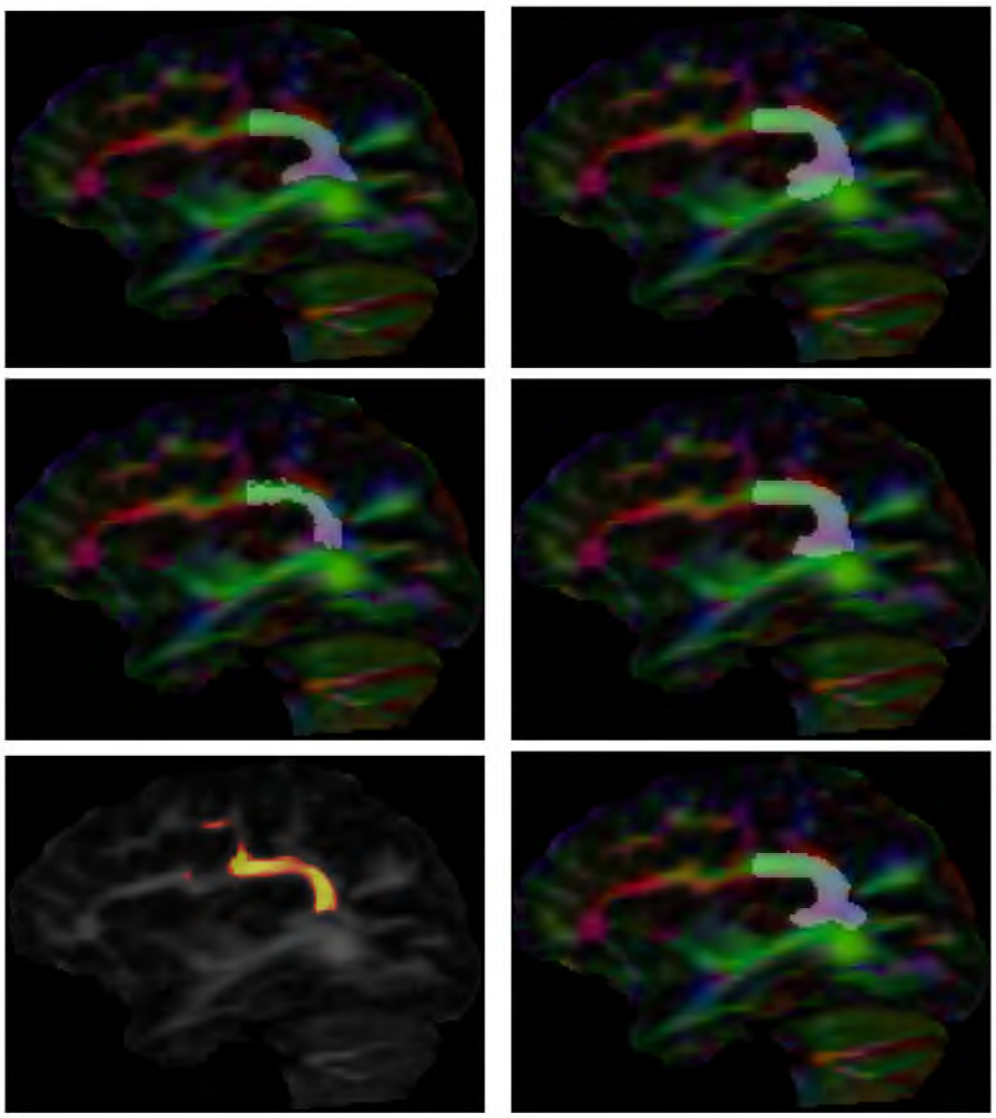

Fig. 4.9. A slice of segmentations (shown in white) and a connectivity map of the direct arcuate fasciculus. Left column (from top to bottom): ground-truth segmentation, segmentation from single-tensor tensor line BF + two-ROI method, connectivity map from stochastic tractography; Right column (from top to bottom): segmentations based on geodesic tracking with the inverse-tensor metric, sharpened-tensor metric, and our adaptive metric

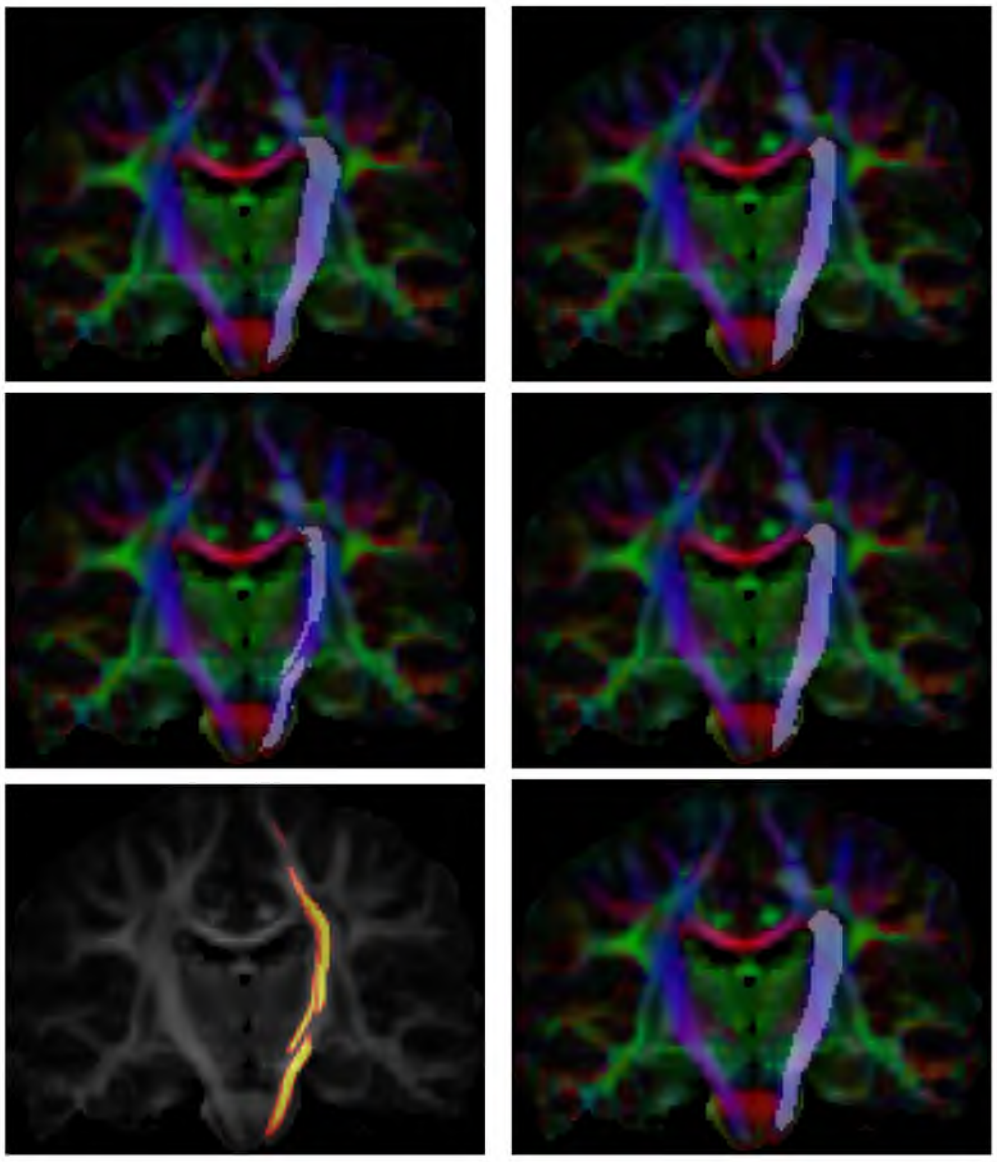

Fig. 4.10. A slice of segmentations (shown in white) and a connectivity map of the corticospinal tract. Left column (from top to bottom): ground-truth segmentation, segmentation from single-tensor FACT BF + two-ROI method, connectivity map from stochastic tractography; Right column (from top to bottom): segmentations based on geodesic tracking with the inverse-tensor metric, sharpened-tensor metric, and our adaptive metric.

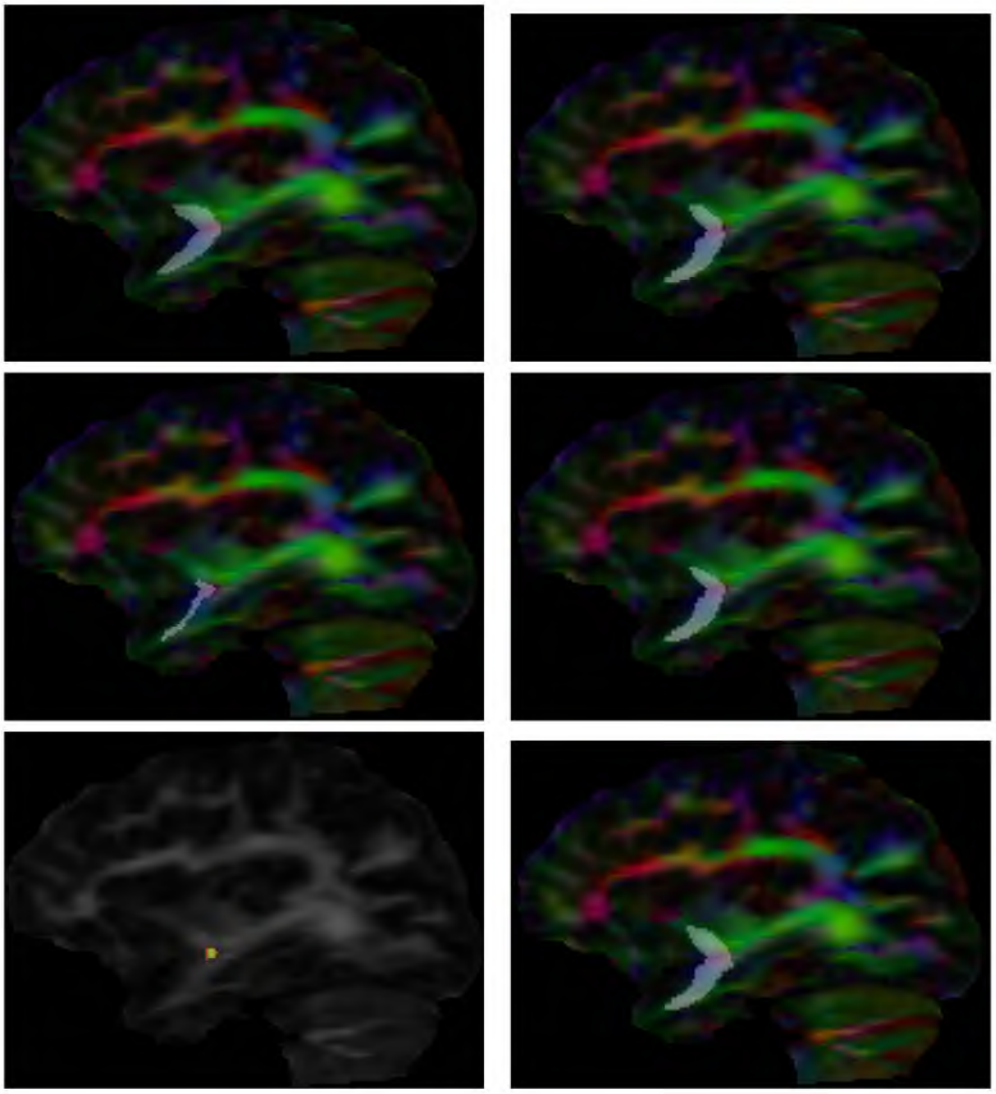

Fig. 4.11. A slice of segmentations (shown in white) and a connectivity map of the uncinate fasciculus. Left column (from top to bottom): ground-truth segmentation, segmentation from single-tensor tensor line BF + two-ROI method, connectivity map from stochastic tractography; Right column (from top to bottom): segmentations based on geodesic tracking with the inverse-tensor metric, sharpened-tensor metric, and our adaptive metric.

segmentation of the genu from the tensor line BF + two-ROI method in Fig. 4.8, we can see that there is an isolated segment in the segmentation. This is caused by some fibers that first went to other tracts of the brain and then make a U-turn before they arrive at the ROI as shown in Fig. 4.12. This problem might be solved by changing our stop criteria, i.e., decreasing the stop angle threshold for tractography, but this results in worse results by also decreasing the volume of the segmentations.

The stochastic tractography has the same undersegmentation problems, as shown by their resulting probability maps. First of all, they miss a lot of voxels around the boundary of the tracts, and we can also see that the central part of the tract has higher probabilities than the voxels close to the boundary of the white matter tracts. For the connectivity map of the uncinate (Fig. 4.11), only a few voxels have intensity in the shown slice, and even in the maximum intensity projection along the sagittal plan (Fig. 4.13), the connectivity map still looks very thin. It is obvious that it is very difficult to get a good segmentation based on the probability map. This makes sense because if a fiber from deterministic tractography stops at the boundary of the white matter, even if we initiate a lot more fibers, there is still a big chance that the fibers arrive at the boundary and stop there. Moreover, both the BF method and stochastic tractography are computationally-intensive approaches. Though the BF process is a preprocessing step and it only needs to be done once, we usually need several gigabytes of storage space to save the whole brain tractography result.

On the other hand, for geodesic-based segmentation methods, the segmentations based

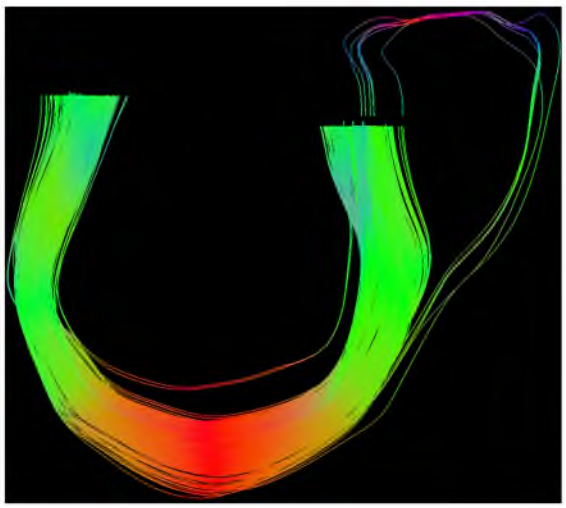

Fig. 4.12. Fibers generated from the single-tensor tensor line BF + tow-ROI method for the genu of the corpus callosum.

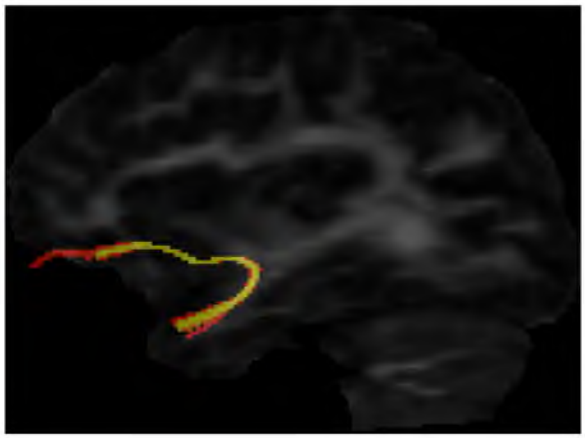

Fig. 4.13. Maximum intensity projection of the connectivity map along the sagittal plane for the uncinate fasciculus.

on the inverse-tensor metric and sharpened-tensor metric are better than the BF + two-ROI approach in terms of missing voxels. For example, they delineate the structure of the corticospinal tract and uncinate fasciculus better, although they sometimes also miss some voxels as shown in Figs. 4.10 and 4.11. However, they also clearly undersegment the genu of the corpus callosum in Fig. 4.8. This is from missing a lot of the voxels at the posterior side of the tract, due to the same curvature effects and shortcutting seen in the synthetic annulus. Also, they may oversegment the tracts as shown in the segmentations of the arcuate fasciculus in Fig. 4.9. Here they both oversegment the tract because they include many voxels below the tract which should be inside the inferior longitudinal fasciculus. However, our adaptive metric results in improved segmentations of these tracts. In the segmentations of the genu in Fig. 4.8, our method corrects the shortcutting and includes most voxels of the genu. Our method's segmentations of the direct arcuate fasciculus are also improved, as seen in Fig. 4.9. While the BF + two-ROI approach undersegments the tract and the other two geodesic-based methods oversegment the tract, our method finds a good balance between the two (although it also includes a few voxels inside the inferior longitudinal fasciculus). For the segmentations of corticospinal tract in Fig. 4.10, the difference among the geodesic-based segmentations is not as obvious as the other tracts since this tract is relatively straight.

4.4 Conclusion

The standard tractography method has the potential to explore white matter structure. It is a good tool to visualize the white matter pathways, but it also lacks reproducibility

and could sometimes produce many false positive tracts due to noise or fiber crossing, so it is not a great tool to do segmentations.

Compared to our method, the BF + two-ROI approach requires the fibers to pass both of the two ROIs. While this increases the validity of tractography, it also make the approach have the tendency to undersegment the white matter tracts since many fibers stop at the boundary of the white matter or enter into other tracts. The stochastic tractography has a very similar problem.

We presented a new geodesic-based algorithm for segmenting white matter tracts in DTI. We developed a segmentation framework based on the computed geodesics from the modified Riemannian metric (Chapter 3). Since the modification and segmentation algorithm are formulated on a general Riemannian manifold, our method can also be applied to problems for which there exist a Riemannian metric (which is just the Euclidean metric in Euclidean space) and preferred geodesics.

We have demonstrated the advantages of our method over the state-of-the-art methods on both synthetic and real data. We have shown that our adaptive Riemannian metric results in geodesics that more faithfully follow the principal eigenvectors of the diffusion tensor field, resulting in segmentations that better delineate the white matter tracts, especially in tracts with high curvature. In addition, there are almost no parameters in our entire framework, and the only user intervention we need is identification of ROIs. As such, our method can be very useful for large data clinical studies, where fewer parameters and user intervention are preferred.

Furthermore, our method is less sensitive to local perturbations, such as noise, partial volume effects, or fiber crossing, compared to tractography algorithms. First, the adaptive metric is computed by minimizing a functional over the whole image domain, which makes our metric less sensitive to the noise as shown in Chapter 3. Second, the front-propagation method computes the pathways by optimizing a global functional using the whole DTI data and hence is less influenced by noise, partial volume effects, or fiber crossing.

CHAPTER 5

JOINT FRACTIONAL SEGMENTATION AND MULTITENSOR ESTIMATION IN DIFFUSION MRI

In this chapter, we present a novel Bayesian approach for fractional segmentation of white matter tracts and simultaneous estimation of a multitensor diffusion model. Our model consists of several white matter tracts, each with a corresponding weight and tensor compartment in each voxel. By incorporating a prior that assumes the tensor fields inside each tract are spatially correlated, we are able to reliably estimate multiple tensor compartments in fiber crossing regions, even with low angular diffusion-weighted imaging (DWI). Our model distinguishes the diffusion compartment associated with each tract, which reduces the effects of partial voluming and achieves more reliable statistics of diffusion measurements. We test our method on synthetic data with known ground truth and show that we can recover the correct volume fractions and tensor compartments. We also demonstrate that the proposed method results in improved segmentation and diffusion measurement statistics on real data in the presence of crossing tracts and partial voluming.

5.1 Introduction

Diffusion-weighted imaging (DWI) is a magnetic resonance imaging (MRI) modality that can measure the directional diffusion of water in tissue, and a second-order model of diffusion within a voxel is estimated from the DWI data in diffusion tensor imaging (DTI). As mentioned in Chapter 2, the diffusion tensor is an elegant description of anisotropic diffusion in white matter and an powerful tool for clinical studies of white matter anatomy and brain development abnormalities, but it is limited to represent only one tract in each imaging voxel. In several regions of the brain, two or more white matter tracts are passing through each other, such as the intersection of the corona radiata and the corpus callosum. In addition, some white matter tracts are mixed with gray matter or cerebrospinal fluid (CSF) at the boundary, such as the corpus callosum and lateral ventricles. In these

cases, a single diffusion tensor is incapable of distinguishing between multiple diffusion compartments.

It has been shown that partial volume effects and underestimation of diffusion measurements occur in crossing areas [110–112]. For example, Alexander et al. [110] showed that the trace of the diffusion tensor will tend to be underestimated in the presence of partial voluming, and Metzler-Baddeley et al. [112] showed that CSF-based partial volume artifacts have a larger impact on tensors with smaller fractional anisotropy (FA). Furthermore, underestimation of diffusion tensor measurements could bias statistics of diffusion measurements, providing misleading results in clinical studies. Although the partial volume effects might be detected during the DTI analysis [113], it cannot resolve the partial volume effects completely, and other methods that can correct the partial volume effects are needed. To address this problem, Tuch et al. [64] proposed an approach using high angular resolution diffusion-weighted imaging (HARDI) (see [65] for a comprehensive review), which measures the DWI signals along a large number of gradient encoding directions, typically 64–100. Several multicompartment models of diffusion have been introduced, such as the multitensor [66] and ball-and-stick [72] models. For example, the multitensor model [66] models the diffusivity in a voxel using a combination of tensor compartments, and each tensor compartment has an associated fraction. HARDI can model the fiber geometries more accurately, but one drawback to HARDI is the increased imaging time required, which has been a barrier to its introduction in clinical studies.

Several works have proposed correcting the partial volume effects using low-angular resolution images (approximately 30 gradient directions) [114–117]. Pasternak et al. [117] proposed a bitensor model that reduces partial volume effects and could also be done in conventional DTI, but this method can only separate brain tissue from surrounding free water and it cannot solve the fiber crossing. Landman et al. [116] used a multitensor model and compressed sensing to solve the fiber crossing using low angular DWI, but they employed a set of basis directions to map the multiple tensor model to lower dimensionality, which could bias the estimated tensors. It has already been shown that the use of spatial regularization can improve the DTI estimation [118–120]. Other researchers [114, 115, 121], therefore, have applied the similar idea and used spatial prior regularization to help the multitensor estimation. For example, Pasternak et al. [121] used a smooth regularization to reduce partial volume effects using multitensor fitting and showed that the regularization can help solve ill-posedness, but they tested their methods on only two fiber crossings. All the methods mentioned above use DWI with at least 30 gradient directions.

None of these methods combine multiple compartment estimation with white matter tract segmentation, which is often a primary goal of DWI analysis. In this paper, we propose a method that jointly solves the tract segmentation and multitensor model estimation problems. In each voxel, our model assigns a fractional weight to each fiber tract to indicate the proportion of that voxel that belongs to the given tract. These weights also serve as the volume fractions in the multitensor model for that voxel, linking the segmentation to the diffusion estimation problem. We impose a Markov random field (MRF) spatial prior to take advantage of spatial redundancy during the estimation and to regularize the multitensor field. To the best of our knowledge, ours is the first model that combines fractional segmentation of white matter with multitensor estimation. We compare our method with state-of-the-art binary segmentations of white matter tracts, which sometimes undersegment or oversegment tracts. We demonstrate that the fractional weights can improve statistical analysis of derived measurements, such as fractional anisotropy (FA), by appropriately weighting the data associated with a particular tract. Using synthetic data with known ground truth, as well as real DWI brain data, we show that our method improves tract segmentations, distinguishes multiple tissue compartments, and provides better diffusion estimates even when using only 12 gradient directions.

5.2 Fractional Segmentation and Multitensor Estimation

In this section, we propose a Bayesian approach to simultaneously estimate both the fractional segmentation of white matter tracts and the multitensor diffusion model. Our goal is to estimate the volume fractions and diffusion tensors in such a way that the DWI signal from the estimated multitensor model matches the measured DWI signal and the estimated tensor compartments in each tract are spatially smooth. This leads to a maximum a posteriori (MAP) estimation approach, in which the log posterior is

$$\log p(\theta|S) \propto \log p(S|\theta) + \log p(\theta),$$

where θ represents the parameters of the model, namely, the multitensor field and volume fractions, and S is the original DWI signal. The likelihood, $p(S|\theta)$, models the fit of the multitensor model in each voxel to the DWI signal, and the prior, $p(\theta)$, is a Markov Random Field (MRF) smoothness prior on the multitensor and volume fraction field. We now describe both the likelihood and prior in detail.

5.2.1 Likelihood—The Data Attachment Term

To model multiple diffusion compartments within a voxel, whether from crossing white matter fiber tracts or mixtures of white matter with CSF or gray matter, we use a multitensor model of the given DWI signals. The multitensor model uses n tensor compartments, D_i, and each tensor compartment is associated with a nonnegative volume fraction f_i to model the DWI signals S_j as

$$S_j(x) = S_0(x) \sum_{i=1}^{n} f_i(x) e^{-b g_j^T D_i(x) g_j}, \text{ with } \sum_{i}^{n} f_i = 1, \tag{5.1}$$

where b is the b-value, S_0 is the baseline image, and g_j is the j-th gradient encoding direction. In contrast to the usual multitensor model, we also associate each volume fraction f_i to a white matter tract segmentation. That is, we want to segment the DWI into n white matter tracts, where $f_i(x)$ represents the fraction of the voxel at position x that is occupied by fibers in the ith tract. In addition, we preserve the n-th tract, a background tract that represents the fraction of the voxel that does not belong to any of the $n-1$ tracts.

Now, assuming the DWI signal is corrupted by additive, i.i.d. Gaussian noise, our log-likelihood is the following DWI signal matching term:

$$\log p(S_j | f_i, D_i) \propto - \int_{\Omega} \sum_{j=1}^{m} \left(S_0(x) \sum_{i=1}^{n} f_i(x) e^{-b g_j^T D_i(x) g_j} - S_j(x) \right)^2 dx.$$

This noise model could be replaced with a Rician noise likelihood or a noncentral chi-distribution for multichannel MRI. Conceptually this would not change the underlying methodology, but rather would make the estimation procedure slightly more complicated. The Gaussian likelihood is a simplifying approximation.

5.2.2 The Markov Random Field Prior

Inside a white matter tract, it is reasonable to assume that the tensors field should be spatially correlated, i.e., the tensor field flows smoothly inside a white matter tract. Thus, we incorporate an MRF prior on the tensor fields inside each tract, given by

$$p(D_i) = \frac{1}{Z} e^{-U_1(D_i)}, \text{ and } U_1(D_i) = \lambda_1 \int_{\Omega} \sum_{i}^{n} \phi_1(D_i(x)) dx,$$

where Z is a normalization constant, λ is a weighting parameter, and $\phi_1(D_i(x))$ is a function that measures the correlation of tensors in the ith tract, around x.

Similarly, the fractions f_i should also be smooth inside a tract except at the boundary of fiber crossings. The prior we incorporate on the fractions inside each tract is in the same form as the prior on the tensor fields, which is

$$p(f_i) = \frac{1}{Z} e^{-U_2(f_i)}, \text{ and } U_2(f_i) = \lambda_2 \int_\Omega \sum_i^n \phi_2(f_i(x))dx.$$

Thus, by combining the log-likelihood term with the prior, we end up minimizing the energy

$$E(f_i, D_i) = \int_\Omega \Bigg(\sum_{j=1}^m \Big(S_0(x) \sum_{i=1}^n f_i(x) e^{-b g_j^T D_i(x) g_j} - S_j(x) \Big)^2 + \lambda_1 \sum_i^n \phi_1(D_i(x)) + \lambda_2 \sum_i^n \phi_2(f_i(x)) \Bigg) dx.$$

We use the full six-component tensor model to represent D_i, but we want to emphasize that D_i could be any other diffusion model, such as the ball-and-stick model. In addition, we use

$$\phi_1(D_i(x)) = \sum_{p,q} \|\nabla D_i^{pq}(x)\|^2 = \sum_{p,q} \sum_{y \in N(x)} (D_i^{pq}(y) - D_i^{pq}(x))^2, \tag{5.2}$$

where N(x) is a neighborhood around x, and D_i^{pq} represents the component in the pth row and the qth column of the matrix D_i. $\phi_1(D_i(x))$ could be generalized to other functions for measuring the smoothness of D_i. For example, we find that it is helpful to use a function that can preserve the edge of the tensor fields, such as the total variation norm, on the background, especially when there are multiple tracts or elements on the background. In this case, the total variation norm can help prevent the blurring across different tracts or elements. We use the total variation norm for the background tract in Section 5.3.4. For the prior on f_i, in order to smooth f_i and preserve boundaries inside f_i as well, our prior on f_i is

$$\phi_2(f_i(x)) = \|\nabla f_i(x)\| = \sqrt{\sum_{y \in N(x)} (f_i(y) - f_i(x))^2}. \tag{5.3}$$

5.2.3 Optimizing f_i and D_i

We use a gradient descent algorithm to compute f_i and D_i. The partial derivatives are computed using the prior in (5.2) and (5.3), but the partial derivatives using other prior can be computed similarly. The partial derivative of E with respect to f_i is

$$\begin{aligned}\frac{\partial E}{\partial f_i} &= \sum_{j=1}^{m} 2\left((S_0(x)\sum_{i=1}^{n} f_i(x)e^{-bg_j^T D_i(x)g_j} - S_j(x))\cdot e^{-bg_j^T D_i(x)g_j}\cdot S_0(x)\right) \\ &\quad + \lambda_2\cdot(-\operatorname{div}(\frac{\nabla f_i(x)}{|\nabla f_i(x)|})), \\ &= 2S_0(x)\sum_{j=1}^{m}\left(e^{-bg_j^T D_i(x)g_j}\cdot\left(S_0(x)\sum_{i=1}^{n} f_i(x)e^{-bg_j^T D_i(x)g_j} - S_j(x)\right)\right) \\ &\quad - \lambda_2\cdot\operatorname{div}(\frac{\nabla f_i(x)}{|\nabla f_i(x)|}),\end{aligned}$$

and the partial derivative of E with respect to D_i^{pq} is

$$\begin{aligned}\frac{\partial E}{\partial D_i^{pq}} &= \Big(\sum_{j=1}^{m} 2\Big((S_0(x)\sum_{i=1}^{n} f_i(x)e^{-bg_j^T D_i(x)g_j} - S_j(x))f_i e^{-bg_j^T D_i(x)g_j}S_0(x) \\ &\quad\cdot(-bg_j^p g_j^q)\Big) + 2\cdot\lambda_1\cdot(-\operatorname{div}(\nabla D_i^{pq}(x)))\Big)\cdot\psi(p,q), \\ &= \Big(\sum_{j=1}^{m} 2\Big((S_0(x)\sum_{i=1}^{n} f_i(x)e^{-bg_j^T D_i(x)g_j} - S_j(x))f_i e^{-bg_j^T D_i(x)g_j}S_0(x) \\ &\quad\cdot(-bg_j^p g_j^q)\Big) - 2\cdot\lambda_1\Delta(D_i^{pq}(x))\Big)\cdot\psi(p,q),\end{aligned}$$

where g_j^p represents the pth element of the vector g_j, and $\psi(p,q) = 1$ if $p = q$, and $\psi(p,q) = 2$ if $p \neq q$. Special care is required in the update of f_i. In every iteration of our gradient descent algorithm, we project the computed gradient of E with respect to f_i onto the constraint hyperplane defined by $\sum_{i=1}^{n} f_i = 1$. To ensure that the f_i remain positive, we also need to project the gradient onto the simplex boundary defined by the constraints $f_i \geq 0$ when necessary. Then we do a line search to compute the optimal step size for updating f_i. Though this should guarantee that f_i satisfies the constraint in theory, in practice we still need to renormalize the f_i to make $\sum_{i=1}^{n} f_i = 1$ every certain number of iterations because of the numerical error.

5.2.4 Initialization of the Optimization with Binary Segmentation

So far, we have not discussed how the binary segmentations are involved in our model. The way we incorporate binary segmentations is through the initialization of our optimization. For the n tracts, the first $n-1$ tracts are the binary segmentation of the white mater tract we want to segment, and we will preserve the last one, the n-th tract that represents the fraction of the voxel that does not belong to any of the $n-1$ tracts.

As in Algorithm 4, to initialize our gradient descent, we first compute binary segmentations for each of the $n-1$ tracts of interest. The nth label is reserved as a "background"

label that does not belong to any of the tracts. The binary segmentations just need to roughly capture the tracts, which could be accomplished by several methods. We use a front-propagation geodesic segmentation [52, 54, 55], which uses a Riemannian metric derived from the diffusion tensor field and constructs white matter tracts as geodesics connecting two regions-of-interest (ROI) on the resulting manifold. These geodesics have the desirable property that they tend to follow the main eigenvectors of the tensors, yet still have the flexibility to deviate from these directions when such deviation results in lower costs. This makes such methods more robust to noise and also allows them to pass through crossing regions. After segmenting the $n-1$ tracts of interest for each voxel inside the predefined image mask, if no segmentations include the voxel, we initialize f_n as 1 and D_n as the weighted least squares estimate of a single-tensor model. Otherwise, we initialize the fractions f_i equally amongst all segmentations that intersect at the voxel, and we initialize all corresponding tensors D_i in that voxel with the same weighted least-squares estimate of a single-tensor model at that voxel.

Algorithm 4 Initialization of f_i and D_i

{Let Ω be the mask we are working with and x be a voxel}
for $x \in \Omega$ **do**
  {Let C be number of binary segmentations that contain voxel x and $T(x)$ be the diffusion tensor estimated from the diffusion tensor model at voxel x.}
  if $C \neq 0$ **then**
    for $i = 1, 2, ..., n-1$ **do**
      $f_i(x) = 1/C, D_i(x) = T(x)$
    end for
    $f_n(x) = 0, D_n(x) = 0$
  else
    for $i = 1, 2, ..., n-1$ **do**
      $f_i(x) = 0, D_i(x) = 0$
    end for
    $f_n(x) = 1, D_n(x) = T(x)$
  end if
end for

5.2.5 Parameter Selection

One key issue of the proposed method is how to select the appropriate parameters for the prior. We find that the most important parameter is the one associated with the tensor smoothness. So we will focus on how to select this parameter, with other parameters fixed.

Our approach to select the appropriate parameter is based on cross validation. Basically, we first randomly select n (for example, we use $n = 24$ for the parameter selection in Sec-

tion 5.3.4) subjects from our dataset. Each subject has a DWI with 12 gradient directions. We randomly select one of the 12 DWI signals as the test data in such a way that the selected gradient directions can spread uniformly on the sphere S^2, and the remaining 11 DWI signals with the b0 image are used to optimize the fractions and tensors. Then, we choose several reasonable parameter values. With each parameter value, we optimize the fractions and tensors, compute the prediction in the gradient direction associated with the test DWI data, and then measure the root mean square error (RMSE) between the predicted DWI and the test DWI data for each subject. In the end, we average the RMSE over the 24 subjects and use the result as a measure of goodness of the parameter value.

In Section 5.3.4, the parameter values we selected are 1E6, 5E6, 1E7, 5E7, 1E8, 5E8, 1E9, 5E9, and 1E10. Their averaged RMSE are $5.47, 5.26, 4.93, 4.44, 4.34, 4.18, 4.25, 5.17$, and 5.30, respectively. In addition, we also fit a single-tensor image with the 11 DWI signals using the weighted least square method and compute its prediction error for the test DWI data. The averaged RMSE is 5.27.

In Fig. 5.1, we plot the computed errors. We can see that the RMSEs of most selected parameters are better than the RMSE of the single-tensor image. Also, among all the parameter values, the one associated with 5E8 has the minimum error.

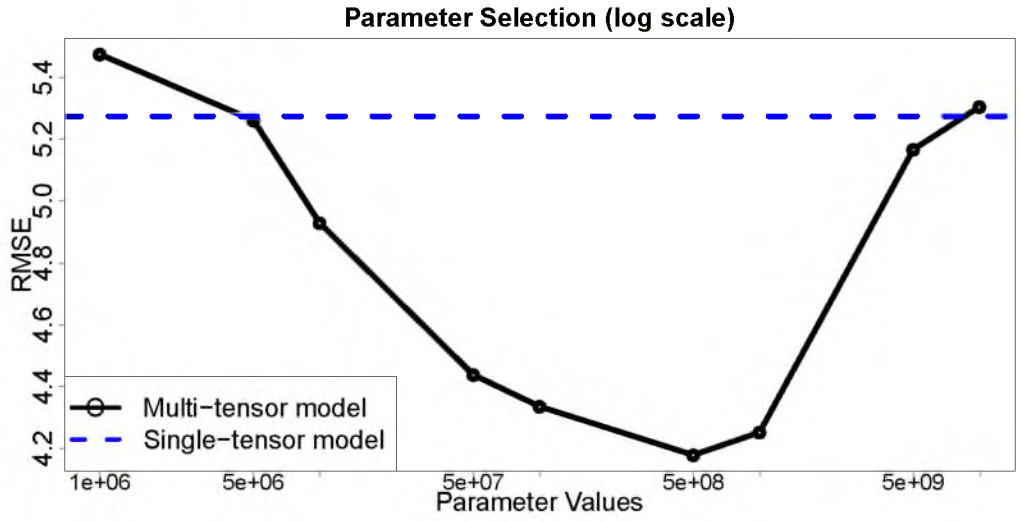

Fig. 5.1. Plot of the averaged RMSE. The RMSE for each parameter value is shown as black points, and the RMSE for the single-tensor image is shown as a blue line.

5.2.6 Path Regression Along the Segmented Tracts

Our estimated fraction f_i can also be used to improve statistical summaries of the diffusion data along segmented tracts. Here we demonstrate an example of the use of these fractions in a nonparametric regression along a tract. Let $\{x_i\}$ be the collection of voxel locations within a segmented tract. Each voxel has an associated parameter, $s_i = s(x_i) \in [0, 1]$, which denotes the arc-length parameter along the pathway at the spatial location x_i [52]. Denote by d_i a data value at the location x_i. This data may be a full diffusion tensor or a derived measure, such as FA or mean diffusivity (MD). We compute a continuous description of the data as a function of s using a nonparametric kernel regression,

$$y(s) = \frac{\sum_i^N d_i f_i G(s - s_i, \sigma)}{\sum_i^N f_i G(s - s_i, \sigma)},$$

where $G(\mu, \sigma)$ denotes a Gaussian kernel with mean μ and standard deviation σ. In the kernel regression, in addition to the Gaussian kernel, each data value is weighted by the fraction f_i, which makes our regression more robust to partial voluming since our fractional segmentation will appropriately assign small f_i to data values influenced by partial voluming. The function y defined above gives a continuous average of the data along the pathway, which can be used to quantify the diffusion measurement along a pathway.

5.3 Results

In this section, we demonstrate the advantages of the fractional segmentations and improvements in multitensor estimations computed by our method on both synthetic and real data. On synthetic data with ground truth, we test our method on both low and high angular DWI and compare it with the multitensor model estimation implemented in Camino [106] using HARDI. Our measure of quality is the root mean square error (RMSE) between the estimated volume fractions/tensors and true volume fractions/tensors. In addition, we also show that our method improves the diffusion measurement statistics. On real data, we demonstrate that the proposed method results in improved segmentation and diffusion measurement statistics in crossing tracts and in the presence of partial voluming. To visualize the fractional segmentation, we convert our fractional segmentation to a color-coded RGB image, where each color component is set to a corresponding volume fraction. For visualization purposes, tensors with a weight lower than 0.2 are not shown.

5.3.1 Correcting Partial Volume Effect

To test the ability of our method to correct partial volume effects, we generated one white matter tract whose boundary is mixed with isotropic tensors as shown in Fig. 5.2.

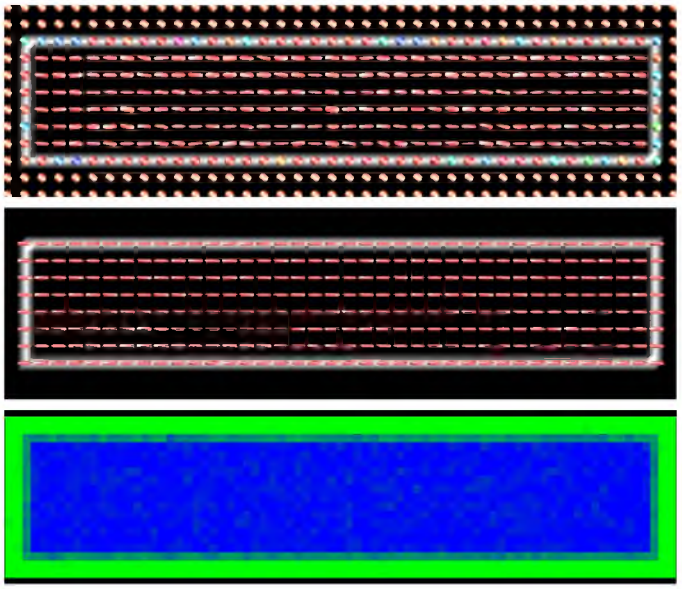

Fig. 5.2. Demonstration of partial volume effect correction. Top: synthetic white matter tract with partial volume effects at the boundary (shown in white). Middle: our estimated tensors. Bottom: our fractional segmentation. We subsample the tensor field by a factor of two both horizontally and vertically in order to visualize it.

The ground truth is a straight white matter tract with a width of 8 voxels and a length of 38 voxels, mixed with isotropic diffusion tensors at the boundary (shown in white in Fig. 5.2) with equal volume fractions in the multitensor model (5.1). The sphere tensors used to simulate CSF have eigenvalue $(3,3,3)\times 10^{-3}\text{mm}^2/\text{s}$. The tensors in the white matter tract have eigenvalue $(1.6,0.4,0.4)\times 10^{-3}\text{mm}^2/\text{s}$. Using the mixed tensor field, we generate DWIs with 12 gradient directions and slightly blur the DWIs to simulate the point spread function (PSF) arising from imaging. We corrupt the DWIs with Rician noise to get an SNR of 20 (top image of Fig. 5.2).

Our estimated white matter tensor field is in the middle image of Fig. 5.2. As we can see, the estimated tensor field can recover the true white matter tensor from the mixed tensors at the boundary. In addition, our estimation algorithm denoises tensors in the interior. Our color-coded fractional segmentation is shown in the bottom panel of Fig. 5.2. In this example, the segmented white matter tract is the blue channel and the exterior is the green channel. The boundary is correctly assigned a 50% mixture of both compartments. The RMSE of our fractional segmentation of the white matter tract is 7.74×10^{-2}, and the RMSE of our estimated tensors is 5.22×10^{-5}.

In the left two images of Fig. 5.3, we do a regression analysis of the FA in the segmented

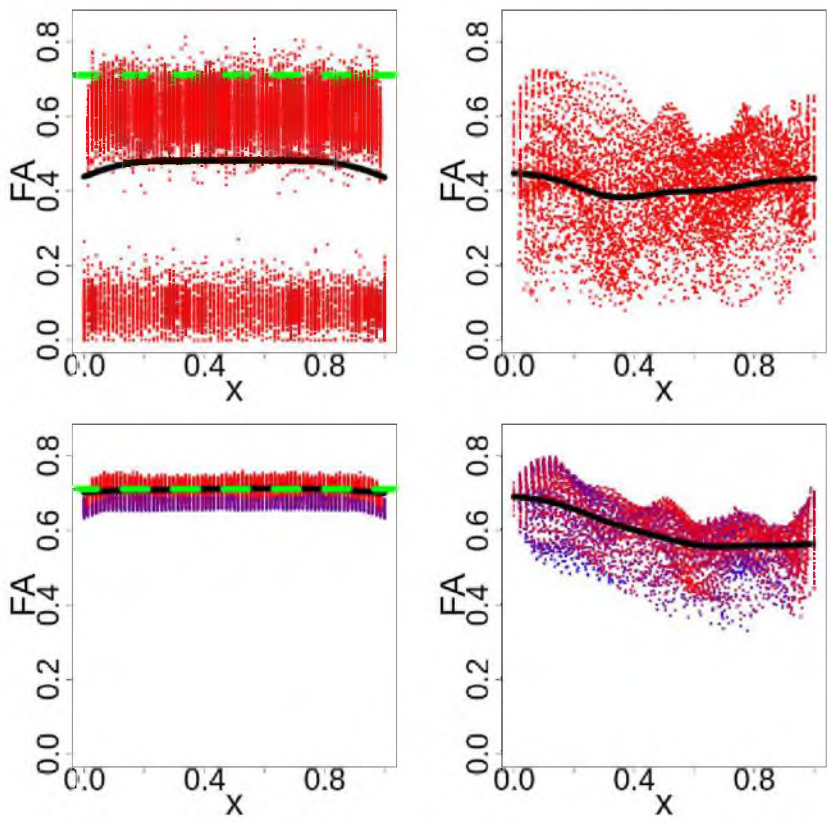

Fig. 5.3. Path regression along the segmented tracts. Left two images: FA regression of simulated straight tract using binary (top) and fractional (bottom) segmentations, respectively. Ground truth is shown in green and the regression is shown in black. Right two images: FA regression of arcuate fasciculus from binary (top) and fractional (bottom) segmentations, respectively.

tracts with $\sigma = 0.1$ as mentioned in Section 5.2.6, where the x-axis is the arc-length position along the tract. We first plot the FA values as points. The color is coded by the volume fractions: solid blue denotes 0, and solid red denotes 1, so the binary segmentation values are always shown in red. The regression along the tract is shown in black, and the ground truth is shown as a dashed green line. It is clear that the partial volume effects bias the regression in the binary segmentations. In our method, the FA values are more tightly distributed around the ground truth due to the reduction of the partial volume effects and the denoising from our spatial prior.

5.3.2 Fiber Crossing White Matter Tracts

To test the performance of our method in the presence of multiple white matter tracts crossing, we generate three fiber crossing tensor fields that have properties similar to many

white matter tracts in the brain: 1) two bars crossing at the center of the image at an angle of 45°, 2) a curved tract crossing with a bar, and 3) three orthogonal bars crossing at the center of the image. We show a center slice of each tensor field in Fig. 5.4.

The tensors in each white matter tract have eigenvalues $(1.6,0.4,0.4)\times 10^{-3}\text{mm}^2/\text{s}$. We generate two sets of DWI datasets, one with 12 gradient directions and the other with 64 gradient directions. Each voxel of the generated crossing DWI at the crossing area was computed based on the multitensor model (5.1), and we use $b = 1000\text{s}/\text{mm}^2$ for both datasets. The true fractions in the crossing regions for the three data sets are (0.4, 0.6), (0.4, 0.6), and (0.3, 0.3, 0.4), respectively. In addition, the DWI was corrupted by Rician noise to simulate an SNR of 20.

In Figs. 5.5 and 5.6, we show the estimated tensors and fractions from our method and Camino. We test Camino only on noisy 64-direction DWI because Camino cannot estimate a multitensor model from only 12 gradient directions (it estimates each voxel independently). However, we can test our method on both noisy 64-direction DWI and 12-direction DWI because our spatial prior utilizes information from multiple neighboring voxels. On the first row of Fig. 5.5, we test our method on noiseless 12-direction DWI to show that we can recover multiple tensors, even when the solution is underdetermined at single voxels because of our spatial prior. On the second and third rows, we test our method on noisy 64-direction DWI and noisy 12-direction DWI. The results are much improved over those from Camino, and our method works slightly better on the 64-direction DWI, for it has more information. The results from Camino are shown in the last row of Fig. 5.5. We gave Camino the advantage of a map of the correct number of tensor compartments in each voxel, but did not provide this extra information to our algorithm.

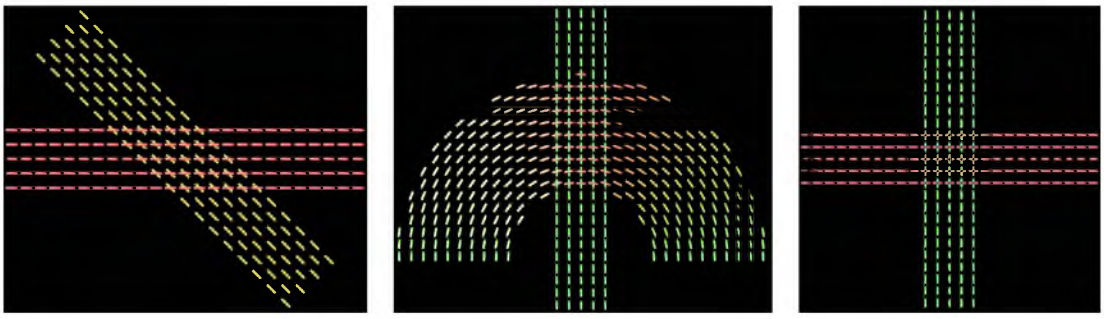

Fig. 5.4. Generated fiber crossing data. Left: 45° crossing. Middle: a curved tract crossing with a straight tract. Right: three orthogonal tracts crossing. We subsample the tensor field by a factor of three both horizontally and vertically in order to visualize it.

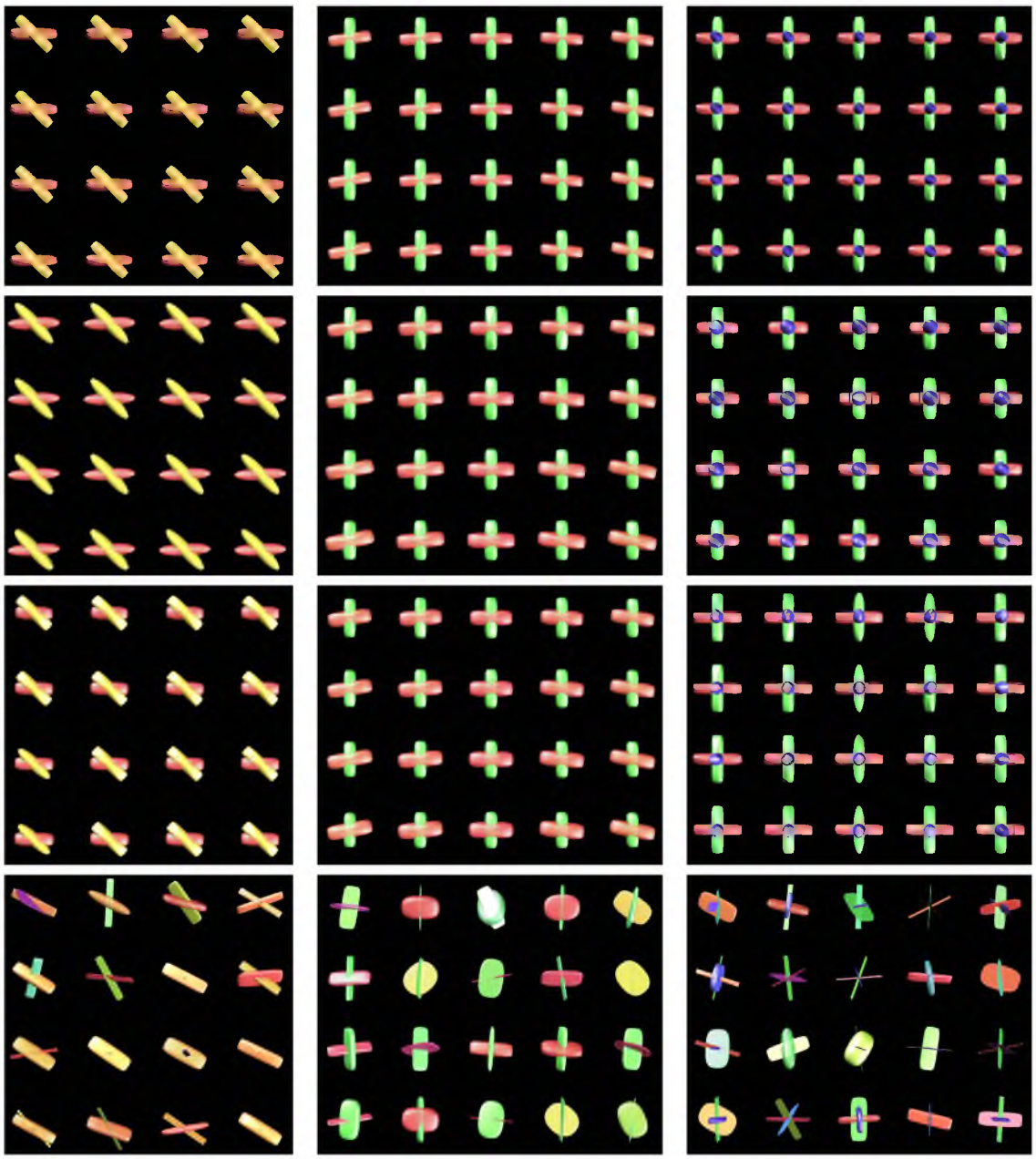

Fig. 5.5. Estimated tensors of the crossing region for the three crossing datasets: first column is for the 45° crossing, second column is for the curved tract crossing, and the third column is for the three orthogonal tracts crossing. First row: our estimated tensors from noiseless 12-direction DWI. Second row: our estimated tensors from noisy 64-direction DWI. Third row: our estimated tensors from noisy 12-direction DWI. Fourth row: estimated tensors from Camino using noisy 64-direction DWI.

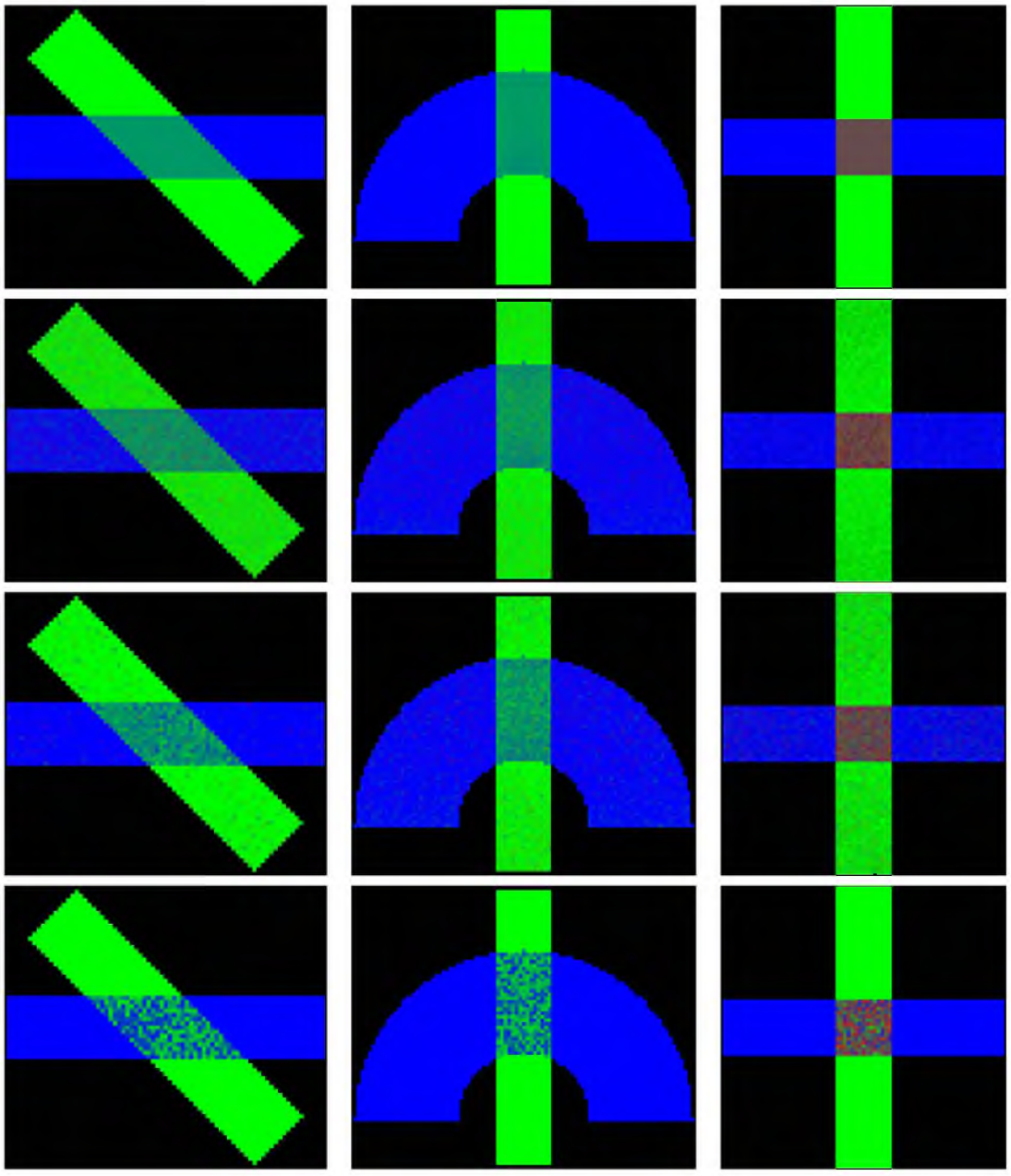

Fig. 5.6. Estimated fractional segmentations. The order is the same as in Fig. 5.5.

We also show our fractional segmentation in Fig. 5.6. Since the weights computed from Camino do not correspond to segmentations, we solve a correspondence problem by minimizing the angles between estimated tensors from Camino and the true tensors. After the optimal order is found, we use the corresponding weights as the fractional segmentation. Outside the crossing region, as we mentioned earlier, we tell Camino the number of tensors, so Camino always has the true weights outside. The finding is consistent with the case for tensor estimation. For the noiseless data, the error between our solution and the true solution is close to zero, as shown in Table 5.1. For the noisy data, the solution of our method is worse when we use the 12-direction DWI than when we use the 64-direction DWI, but generally our results are fairly good for all three cases, and they look better than Camino inside the crossing regions.

In Table 5.1, we do a quantitative comparison of our method and Camino. Since we give Camino the true weight outside the crossing regions, to do a better comparison, we compute the RMSE of the estimated volume fractions only inside the crossing region, but we compute the RMSE of tensors in the whole white matter tracts. As shown in Table 5.1, the RMSE of our method is much smaller than the RMSE of Camino, and our method works best on the noiseless data, but when there is noise, our method has smaller RMSE when using DWI with more gradient directions.

5.3.3 Real Data

We now show the results of our method applied to real DWI data. DWI data were acquired on a Siemens Trio 3.0 Tesla Scanner with an 8-channel, receive-only head coil. DWI was performed using a single-shot, spin-echo, EPI pulse sequence and SENSE parallel imaging (undersampling factor of 2). Diffusion-weighted images were acquired in 12 noncollinear diffusion encoding directions with diffusion weighting factor b = 1000 s/mm^2 in addition to a single reference image (b = 0). Data acquisition parameters included the following:

Table 5.1. RMSE of the estimated volume fractions and tensor compartments of our method (first three rows) and Camino using noisy DWI with 64 directions (last row).

	45° Crossing		Curved Crossing		Three Crossing	
	Weight	Tensor	Weight	Tensor	Weight	Tensor
Clean 12-dir	$1.16E{-}4$	$5.61E{-}7$	$1.44E{-}2$	$2.97E{-}5$	$1.33E{-}5$	$1.12E{-}7$
Noisy 64-dir	$7.38E{-}2$	$1.39E{-}4$	$4.89E{-}2$	$1.38E{-}4$	$5.16E{-}2$	$2.09E{-}4$
Noisy 12-dir	$8.37E{-}2$	$1.54E{-}4$	$6.18E{-}2$	$1.63E{-}4$	$5.71E{-}2$	$3.07E{-}4$
Camino	$2.6E{-}1$	$4.40E{-}3$	$2.34E{-}1$	$2.89E{-}3$	$1.45E{-}1$	$3.14E{-}3$

contiguous (no-gap) 50 2.5 mm thick axial slices with an acquisition matrix of 128 x 128 over a FOV of 256 mm (2 x 2 mm^2 in-plane resolution), four averages, repetition time (TR) = 7000 ms, and echo time (TE) = 84 ms. Eddy current distortion and head motion were corrected using an automatic image registration program [98]. Distortion-corrected DW images were interpolated to 1 x 1 x 1 mm^3 voxels, and six tensor elements were calculated using weighted least squares. The tensor upsampling is done only for the purposes of numerical computations on the voxel grid; a finer grid results in higher numerical accuracy.

To test the reliability of our method, we first randomly select one subject from the dataset, who has both a 12-direction DWI and a 64-direction DWI. Using the 12-direction DWI, we fit a single-tensor image. Using the same 12-direction DWI and selected parameter value as described in Section 5.2.5, we apply our method to the left arcuate fasciculus of the brain of the subject. Then we compute the RMSE between the predicted DWI and the 64-direction DWI data for both the single-tensor method and the proposed method.

The histogram of the differences between the two sets of RMSE is shown in Fig. 5.7. We can see that most of the RMSE of the proposed method is smaller than the one of the single-tensor method. The mean and standard deviation of the differences are -0.91 and 1.50. Also, we did a one-sided Wilcoxon test of the differences. The null hypothesis is that the differences have a 0 mean, and the result shows that the mean is significantly less than 0 with a p-value 1.28E-5. This means that the RMSE of the proposed method is significantly smaller than the one of the single-tensor method.

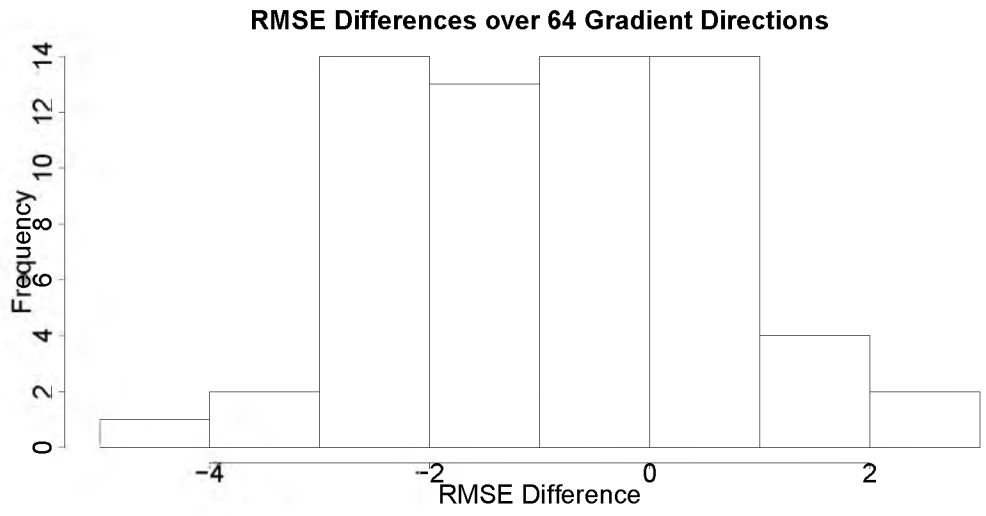

Fig. 5.7. Histogram of the differences between the RMSE of the proposed method and the one of the single-tensor image over 64 gradient directions.

In Fig. 5.8, we show our results for the arcuate fasciculus of the brain of a subject. In the first column, we show the initial binary segmentation, the DTI tensor field, and the color-coded principal eigenvector image. As we can see, the binary segmentation oversegments the tract because it includes many voxels (red arrow) below the tract that should be inside the inferior longitudinal fasciculus. In addition, it also undersegments the tract, missing the blue area on the lower right of the image (black arrow), which should be included in the segmentation. On the top-right image, we overlay the DTI tensor field on our fractional segmentation to demonstrate that our segmentation corrects the errors from the binary segmentation. In the middle-right image, we overlay our estimated tensors on top of our

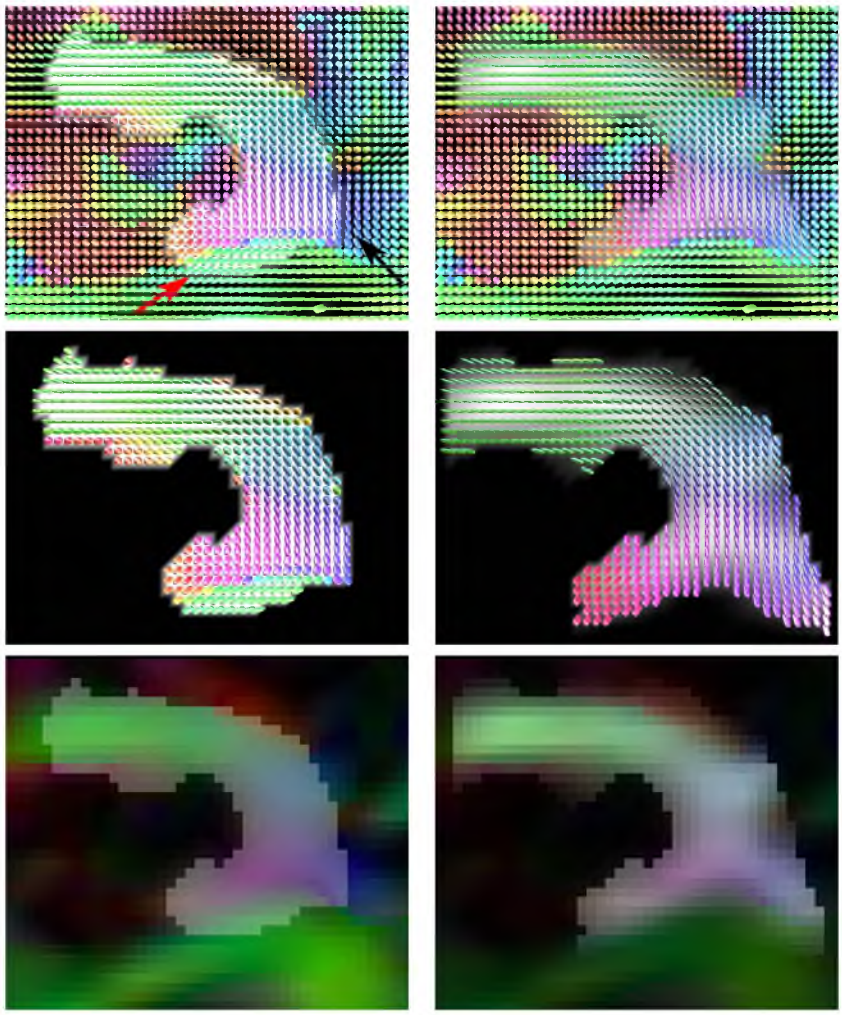

Fig. 5.8. The binary segmentation is shown on the first column and our fractional segmentation is shown on the second column. The overlay tensor fields are the DTI tensor field except for the last one, where our estimated tensors are displayed. On the last row, the background images are the color-coded principal eigenvector images.

segmentation. In the bottom-right image, we overlay our estimated fractional segmentation on the color-coded principal eigenvector image. From both images, we can see that our segmentation reduces the partial voluming effect at the boundary of the tract and has lower weights at the border of the arcuate fasciculus and inferior longitudinal fasciculus, where the tensors from the two tracts are mixed together. In addition, our segmentation also includes the blue area, which the binary segmentation missed.

In the right two images of Fig. 5.3, we do a similar regression analysis as mentioned in Section 5.3.1. We can see the FA values are more tightly distributed on the bottom image than on the top one, which is a sign of a possible reduction of partial volume effects as shown in Section 5.3.1. In addition, it may improve statistical power in clinical studies by reducing the within-subject variance.

We also test our method on a brain region with complex white matter organization as shown in Figs. 5.9 and 5.10. In this brain region, we segment three white matter tracts as the binary input of our method. These three tracts are one branch from the corpus callosum, the corticospinal tract, and the superior longitudinal fasciculus. In Fig. 5.10, we compare the DTI model with the proposed method. In the first column, we overlay the DTI tensor field on the FA background and its closer view of the crossing region. In the second column, we show our estimated tensors and a closer view of the same crossing region. As we can see, the DTI model cannot tell the different fibers inside a voxel. However, it is clear that our method can estimate multiple tensor compartments in the crossing region and also reduce the isotropic partial voluming of the estimated tensors in the corpus callosum (blue arrow). Our fractional segmentation is shown in Fig. 5.9, where we overlay our color-coded fractional segmentation on top of the FA background on the top two images. We overlay the estimated tensor compartments on the corresponding fractional segmentation on the bottom three images. We can see that the tensors in each white matter tract are spatially consistent due to our spatial prior, and the fractional segmentation is biologically reasonable.

5.3.4 Diffusion Measurement Analysis of Autism Disorder

Many disorders and diseases are related to brain white matter tracts. Autism spectrum disorder is one of them. Autism is a neuropsychiatric disorder characterized by impaired communication and repetitive behavior. The prevalence of autism in children is about 2% in the United States as of 2012. Analyzing the cause of autism is important not only for studying the white matter abnormalities in neuropsychiatric disorders, but also for better understanding normal brain development.

A key diagnostic feature of autism is impairment in communication, especially language

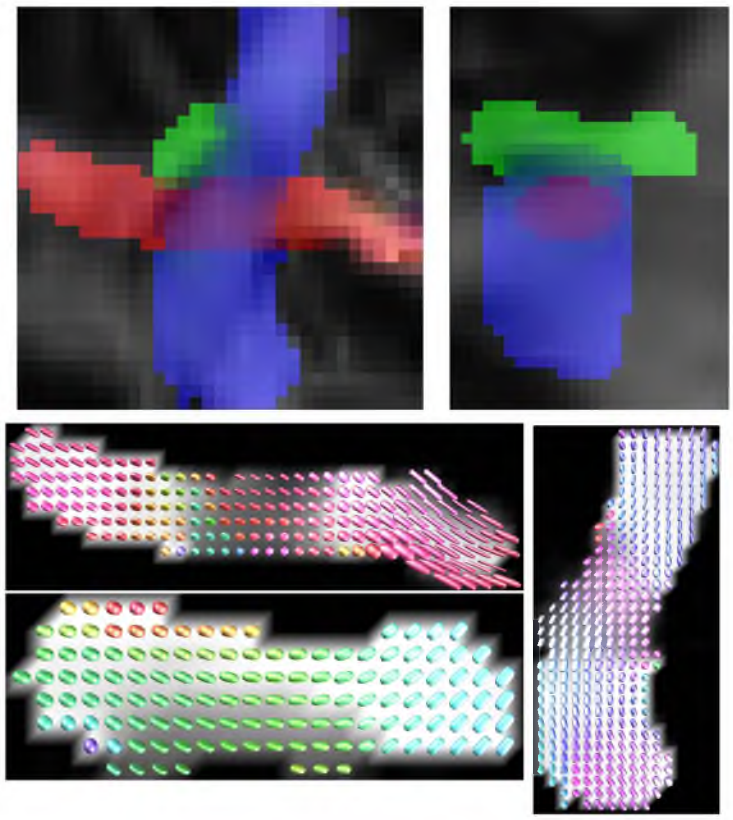

Fig. 5.9. Our fractional segmentation.

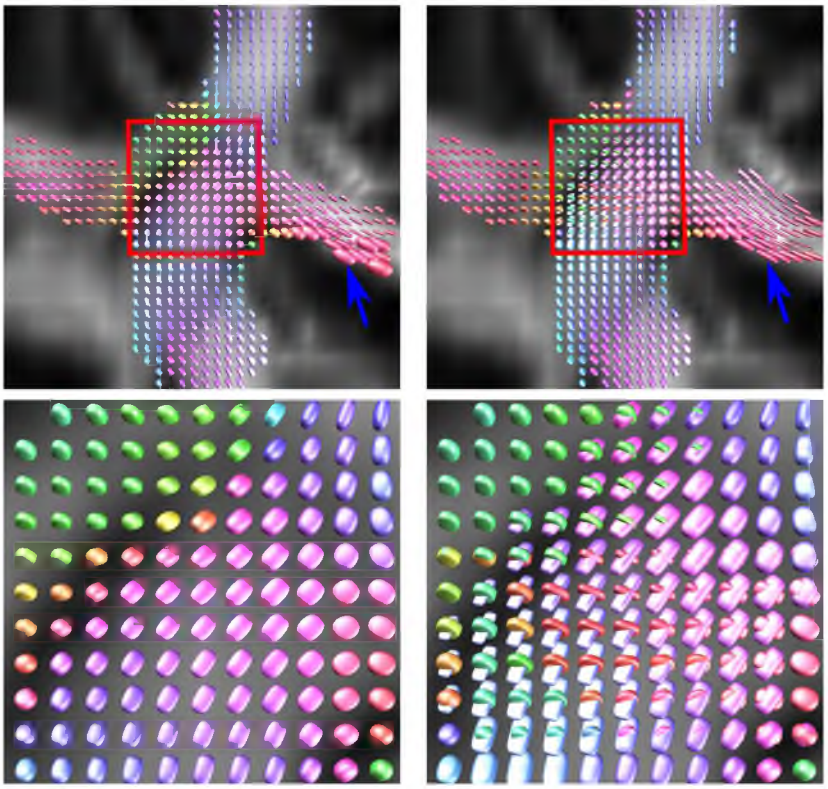

Fig. 5.10. The proposed method can distinguish multiple tissue compartments in a fiber crossing area. First row: the DTI field, and our estimated multitensor field. Second row: the closer views of the crossing region (inside the red box).

impairments, and it has been found that language development and functioning is significantly delayed in autism. For example, children with autism sometimes have difficulty responding to spoken language even though their hearing is normal. Moreover, the arcuate fasciculus (AF) is a white matter tract that is crucial in language, and it connects three language regions, Wernicke's area, Broca's area, and Geschwind's area. Thus, the AF is an important structure to study in autism, and it is interesting to research whether the AF of individuals with autism is different from that of typically developing people.

We have been working with an autism dataset from our collaborator Dr. Janet Lainhart from the Department of Psychiatry, University of Wisconsin-Madison. This dataset includes many DWI scans of patients with autism and typically developing people. We use this dataset to explore the white matter abnormalities in autism by comparing the diffusion measurements from segmentations of people with autism with the ones of typically developing people.

Table 5.2 shows the characteristics of the selected samples from this dataset. We selected

Table 5.2. Characteristics of the samples.

	Control Group (n=29)			Autism Group (n=27)		
	Mean	SD	Range	Mean	SD	Range
Age (years)	15.64	5.43	8-26	15.71	5.23	7-27
PIQ	110.55	11.55	90-134	108.24	12.11	80-125
VIQ	112.34	12.54	91-140	107.44	20.26	71-145

29 typically developing people and 27 people with autism. The two groups were matched on age, verbal IQ, and performance IQ. We first use the method proposed in Chapter 4 to compute binary segmentations of AF for both groups. Then, we study the white matter abnormalities in autism by comparing the diffusion measurements computed from binary segmentations of people with autism with the ones of typically developing people [122]. In the next, with the binary segmentation as the initialization of the proposed method, we compute the fractional segmentation and multitensor estimation of AF for both groups, and similarly we use the estimated tensors to explore the white matter abnormalities in autism neuropsychiatric disorder by analyzing the diffusion measurements computed from our fractional segmentation. In addition, we also compare the diffusion measurements analysis using the binary segmentation with the one using fractional segmentation.

As mentioned earlier, we compute the binary segmentations of both the left and the right AF for each subject. For each segmented AF, we compute the average values for axial diffusivity (AD), radial diffusivity (RD), FA, and MD as in [122]. For the proposed method, we compute the fractional segmentation and multitensor estimation of both the left and the right AF with the selected optimal parameter value as described in Section 5.2.5, and then we compute the weighted mean of AD, RD, FA, and MD for each AF. In the following discussion, when we say the diffusion measurements in fractional segmentation, we mean the diffusion measurements computed from the foreground tensors weighted by the foreground fractions.

Many studies show hemisphere asymmetry in volume or diffusion measurements of the AF. To understand the hemisphere asymmetries in AF between the typically developing people group and the autism group, we fit linear mixed effect (LME) models for each diffusion measurements. The model we use is $y \sim$ age + group (autism or control) + hemisphere (left or right) + group*hemisphere, where y is one of the diffusion measurements and group*hemisphere represents the interaction between group and hemisphere. The control group and left hemisphere (LH) is chosen as the reference category. This means a significant hemisphere (right) effect indicates a significant difference in mean diffusion measurement between left and right hemisphere (RH) for controls, a significant group

(autism) effect indicates a significant difference in mean diffusion measurement between control and autism in the LH, and a significant interaction between group and hemisphere indicates a significant difference in asymmetry between autism and controls.

In Tables 5.3 and 5.4, we show the results from LME of volume for both the binary segmentation and fractional segmentation. We can see that for both binary and fractional segmentation, there was a significant decrease in volume from the left AF to the right AF. In addition, for the binary segmentation, age had a significant effect on volume; for fractional segmentation, the effect of age was not significant but approaches significance ($p = 0.0661$). The volume data is plotted in Fig. 5.11.

Table 5.3. Linear mixed effects model analysis of volume computed from binary segmentation.

Covariate	Est. Effect	SE	t-value	p-value
Age	4.58E1	2.20E1	2.08	0.0426
Autism	1.78E2	2.97E2	0.60	0.5510
RH	-9.56E2	2.57E2	-3.72	0.0005
Autism x RH	3.70E2	5.79E-3	-0.31	0.7613

Table 5.4. Linear mixed effects model analysis of volume computed from fractional segmentation.

Covariate	Est. Effect	SE	t-value	p-value
Age	2.92E2	1.55E1	1.88	0.0661
Autism	1.38E2	2.05E2	0.67	0.5031
RH	-7.77E2	1.70E2	-4.58	0.0000
Autism x RH	2.44E2	8.80E-3	-0.25	0.8042

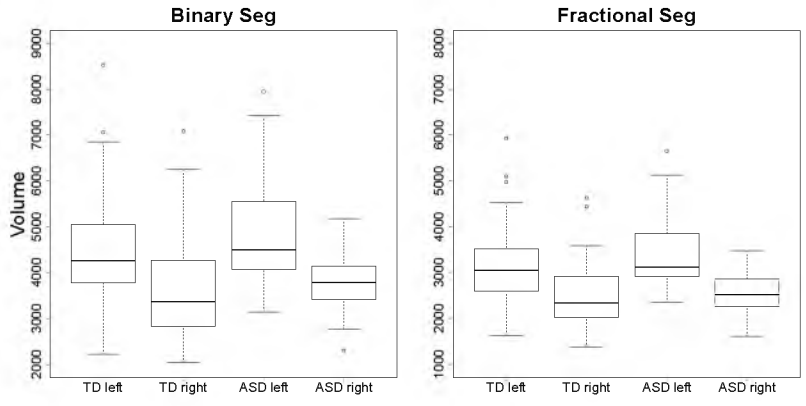

Fig. 5.11. Boxplot of volume in the arcuate fasciculus for both control and autism groups.

In Tables 5.5, 5.6, 5.7, 5.8, 5.9, 5.10, 5.11, and 5.12, we show the coefficients of LMEs of AD, MD, FA, and RD. For AD, there were no significant effects of age, group, or hemisphere in both binary and fractional segmentation, but the interaction between group and hemisphere was significant in the fractional segmentation. For MD, FA, and RD, age, hemisphere, and group had significant effects in the binary segmentation. The MD and RD were significantly decreased with age, whereas the FA was significantly increased with age. In addition, the MD and RD were significantly increased in the RH for controls and in the autism group in the LH, and the FA was significantly decreased in the RH for controls and the autism group in the LH. In contrast, in fractional segmentation for FA and RD, age had similar significant effects with binary segmentation, and the interaction between group and hemisphere was significant for MD. There were no significant effects, however, with hemisphere or group.

Table 5.5. Linear mixed effects model analysis of AD computed from binary segmentation.

Covariate	Est. Effect	SE	t-value	p-value
Age	-1.28E-3	8.69E-4	-1.48	0.145
Autism	1.29E-2	9.88E-3	1.30	0.198
RH	5.67E-3	5.06E-3	1.12	0.268
Autism x RH	8.78E-3	7.29E-3	1.20	0.234

Table 5.6. Linear mixed effects model analysis of AD computed from fractional segmentation.

Covariate	Est. Effect	SE	t-value	p-value
Age	3.92E-4	2.46E-3	0.16	0.8742
Autism	-3.96E-2	3.24E-2	-1.22	0.2278
RH	3.13E-2	2.69E-2	1.16	0.2492
Autism x RH	8.98E-2	3.87E-2	2.32	0.0242

Table 5.7. Linear mixed effects model analysis of MD computed from binary segmentation.

Covariate	Est. Effect	SE	t-value	p-value
Age	-2.93E-3	6.62E-4	-4.43	0.0000
Autism	2.16E-2	7.18E-3	3.01	0.0040
RH	1.82E-2	2.23E-3	8.15	0.0000
Autism x RH	-3.79E-4	3.22E-3	-0.12	0.9067

Table 5.8. Linear mixed effects model analysis of MD computed from fractional segmentation.

Covariate	Est. Effect	SE	t-value	p-value
Age	-2.88E-3	1.64E-3	-1.76	0.0849
Autism	3.50E-3	2.08E-2	0.17	0.8666
RH	1.48E-2	1.59E-2	0.94	0.3535
Autism x RH	4.75E-2	2.28E-2	2.08	0.0425

Table 5.9. Linear mixed effects model analysis of FA computed from binary segmentation.

Covariate	Est. Effect	SE	t-value	p-value
Age	2.65*E-3	5.39E-4	4.92	0.0000
Autism	-1.83*E-2	6.39E-3	-2.86	0.0060
RH	-2.22E-2	4.03E-3	-5.51	0.0000
Autism x RH	1.03E-2	5.79E-3	1.77	0.0816

Table 5.10. Linear mixed effects model analysis of FA computed from fractional segmentation.

Covariate	Est. Effect	SE	t-value	p-value
Age	2.96E-3	9.60E-4	3.09	0.0032
Autism	-2.14E-2	1.11E-2	-1.94	0.0580
RH	-2.27E-3	6.11E-3	-0.37	0.7122
Autism x RH	1.16E-4	8.80E-3	0.01	0.9895

Table 5.11. Linear mixed effects model analysis of RD computed from binary segmentation.

Covariate	Est. Effect	SE	t-value	p-value
Age	-3.75E-3	7.37E-4	-5.16	0.0000
Autism	2.59E-2	8.05E-3	3.22	0.0022
RH	2.45E-2	3.36E-3	7.29	0.0000
Autism x RH	4.96E-3	4.84E-3	-1.03	0.3098

Table 5.12. Linear mixed effects model analysis of RD computed from fractional segmentation.

Covariate	Est. Effect	SE	t-value	p-value
Age	-4.51E-3	1.71E-3	-2.64	0.0109
Autism	2.50E-2	2.03E-2	1.23	0.2234
RH	6.61E-3	1.29E-2	0.51	0.6104
Autism x RH	2.63E-2	1.86E-2	1.41	0.1628

It seems that some significance disappeared in the fractional segmentation (the diffusion measurements from the foreground tensors weighted by the foreground fractions). To understand where the differences were between binary segmentation and fractional segmentation, we did the same analysis on the raw tensors (the single-tensor estimated from DWI) weighted by the foreground fractions to check whether the differences were caused by the estimated fractions or the estimated tensors. The results turned out to be similar to the ones associated with binary segmentation. Age, hemisphere, and group had similar significant effects for MD, FA, and RD, but not for AD. We show the boxplots of AD and MD in Figs. 5.12, 5.13, and 5.14 and results from LMEs of AD and MD in Tables 5.13 and 5.14. These results suggest the statistical differences between binary segmentation and fractional segmentation were mainly from the estimated multitensors. We use the total variation norm as the prior on the background to prevent blurring across different tracts or elements, and the estimated fractions and tensors are more like the multitensor representation of the DWI signals. When some of DWI signals cannot be explained by the foreground tensors, it is likely that they are explained by the background tensors.

Thus, we also did the same kind of analysis on the weighted background tensors using the foreground fractions to check where there are something important for the group difference in the background tensors. We use the foreground fractions to weight the background tensors to find out whether the estimated background tensors are important for the differences between the control group and autism groups. We want to use the background tensors only inside the arcuate fasciculus, so we weighted the background tensors with the foreground fractions. It turns out that for AD, MD, FA, and RD, the hemisphere had a significant effect. The AD, MD, and RD were significantly increased in the RH for controls, whereas the FA was significantly decreased in the RH for controls. We show the boxplots of AD, MD, and RD in Figs. 5.12 and 5.13 and results from the LMEs of AD and MD in Tables 5.15 and 5.16. This result is similar to the one from binary segmentation and consistent with what was found in [122]. Another major finding in [122] was that the MD and FA were less lateralized in the autism group. Though no significant group and hemisphere interactions were found in this experiment, the decreases in asymmetry between control and autism were relatively close to the significance level for AD and MD, compared to the one from binary segmentation. These results suggest the background tensors may contain information that is important for the differences between control and autism groups, and we should consider incorporating the background tensors into the exploration of the white matter abnormalities in autism neuropsychiatric disorder. However, the way we incorporate the background

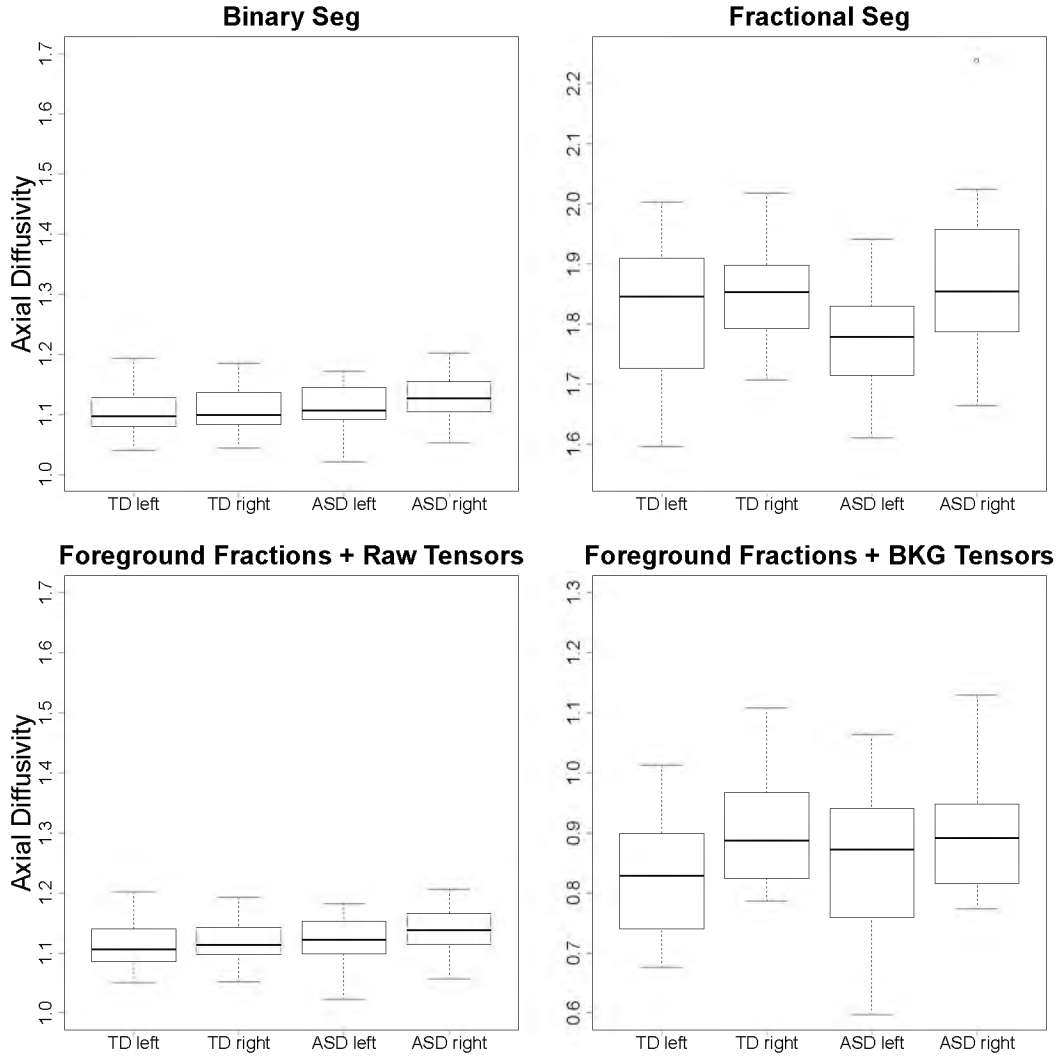

Fig. 5.12. Boxplot of AD in the arcuate fasciculus for both control and autism groups.

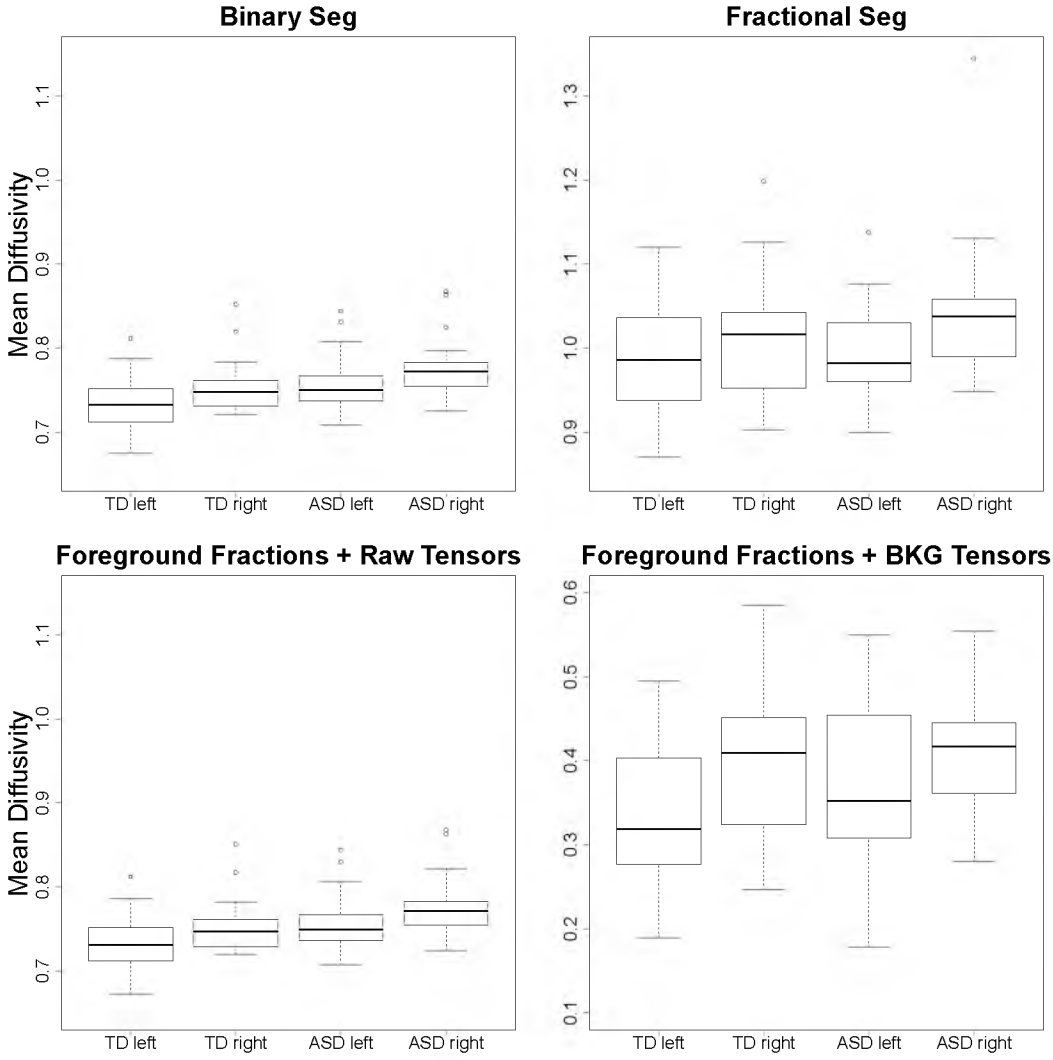

Fig. 5.13. Boxplot of MD in the arcuate fasciculus for both control and autism groups.

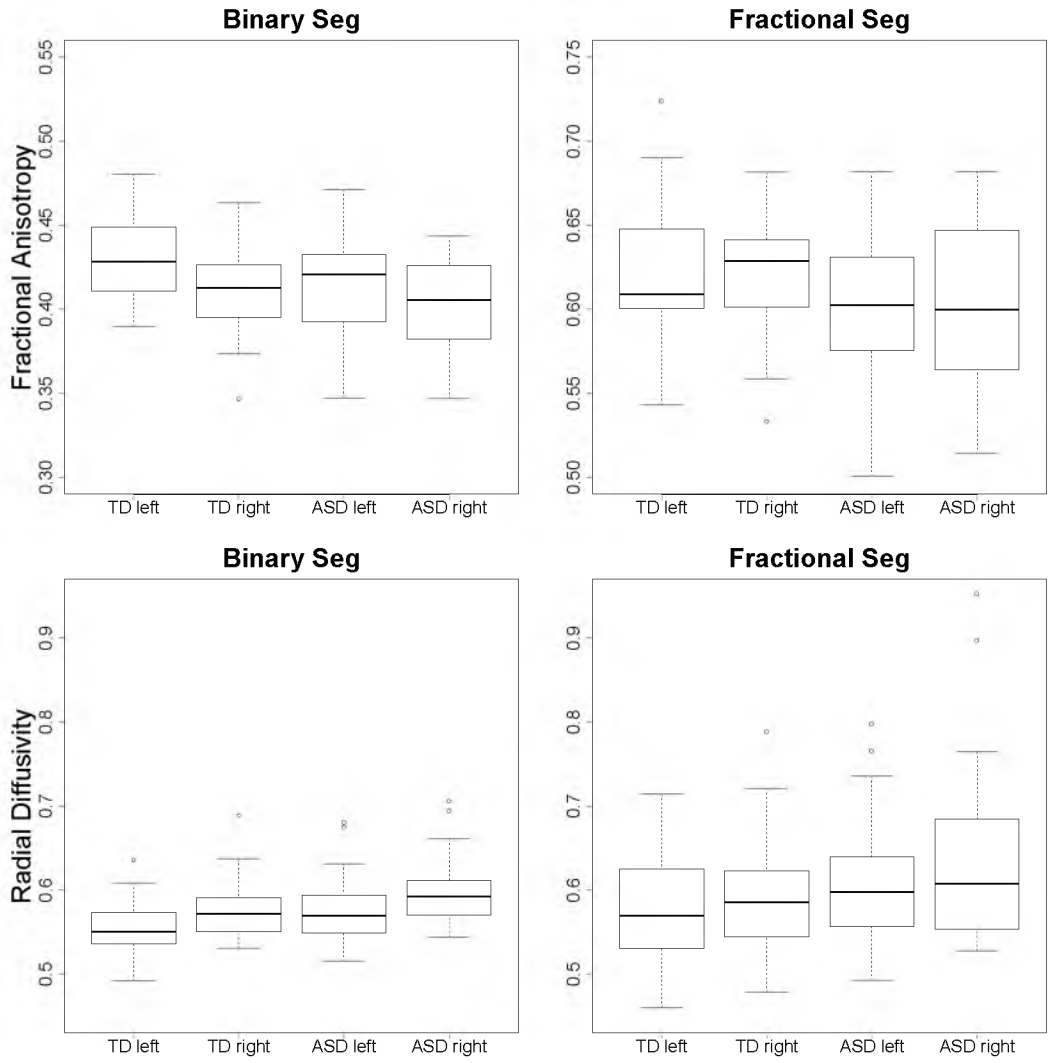

Fig. 5.14. Boxplot of FA (top) and RD (bottom) in the arcuate fasciculus for both control and autism groups.

Table 5.13. Linear mixed effects model analysis of AD computed from fractional segmentation with raw tensors.

Covariate	Est. Effect	SE	t-value	p-value
Age	-1.23E-3	8.89E-4	-1.16	0.2525
Autism	1.31E-2	1.02E-2	-1.29	0.2015
RH	7.42E-3	5.24E-3	1.42	0.1627
Autism x RH	7.31E-3	7.55E-3	0.97	0.3375

Table 5.14. Linear mixed effects model analysis of MD computed from fractional segmentation with raw tensors.

Covariate	Est. Effect	SE	t-value	p-value
Age	-2.92E-3	6.65E-4	-4.40	0.0001
Autism	2.18E-2	7.21E-3	3.02	0.0038
RH	1.82E-2	2.23E-3	8.16	0.0000
Autism x RH	-2.10E-4	3.21E-3	-0.7	0.9481

Table 5.15. Linear mixed effects model analysis of AD computed from fractional segmentation with background tensors.

Covariate	Est. Effect	SE	t-value	p-value
Age	-2.33E-3	2.41E-3	-0.97	0.3375
Autism	2.93E-2	3.23E-2	0.90	0.3697
RH	7.72E-2	2.76E-2	2.79	0.0072
Autism x RH	-6.39E-2	3.98E-2	-1.61	0.1143

Table 5.16. Linear mixed effects model analysis of MD computed from fractional segmentation with background tensors.

Covariate	Est. Effect	SE	t-value	p-value
Age	-2.08E-3	1.81E-3	-1.15	0.2561
Autism	3.46E-2	2.45E-2	1.41	0.1631
RH	6.26E-2	2.11E-2	2.96	0.0045
Autism x RH	-4.40E-2	3.05E-2	-1.44	0.1545

tensors into the analysis is somewhat ad hoc, and how to use this information appropriately is open to future research. In addition, only the hemisphere had a significant effect in this analysis. And for all the analysis, the raw tensors have the most sensitive statistics that can distinguish the two groups. While the fractional segmentation gives a better qualitative segmentation of the tracts and the multitensor model can better represent the DWI signals, it does not necessary give better statistics. At least in this application, the raw tensors have a better summary of the diffusion measurements.

5.4 Conclusion

We present a Bayesian approach for joint fractional segmentation of white matter tracts and multitensor estimation in DWI. Our method can reliably estimate multiple tensor compartments in fiber crossing regions even with low angular DWI. We apply the fractional segmentation to explore the white matter abnormalities in autism neuropsychiatric disorder. The results suggest the raw tensors have the most sensitive statistics that can better distinguish the autism group from the control group. While the fractional segmentation gives a better qualitative segmentation of the tracts and the multitensor model can better represent the DWI signals, it does not necessary give better statistics. It is interesting to research whether there are ways to combine multiple tensors to better summarize the diffusion measurements.

CHAPTER 6

CONCLUSIONS AND FUTURE WORK

In this chapter, I will summarize the contributions and limitations of the dissertation and propose open questions and possible future research directions in DWI segmentation and tracking.

6.1 Summary

The tracking and segmentation of white matter tracts is a challenging problem due to image artifacts, such as noise and partial volume effects. Moreover, due to the lack of high angular DWI data in most clinical studies, it is also difficult to estimate HARDI models. In this dissertation, we address questions about how to track and segment the white matter tracts accurately and how to estimate a HARDI model, such as the multitensor model, from low angular DWI data.

- We first presented a geodesic-based method to track the brain white matter tracts. This method used a scaling of the inverse-tensor Riemannian metric that results in geodesics adapted to follow the principal eigendirection of the diffusion tensor even in high-curvature brain regions. Compared to tractography algorithms, our method is less sensitive to local perturbations, such as noise, partial volume effects, or fiber crossing (Chapter 3).
- On the basis of the proposed adaptive geodesic tracking of the white matter tracts, we then described an automatic binary segmentation framework by taking advantages of the angles of the two characteristic vector fields from the two predefined ROIs. Our method can better delineate the white matter tracts. Since both the adaptive Riemannian metric and the automatic segmentation algorithm are formulated on a general Riemannian manifold, our method can also be applied to problems for which there exist a Riemannian metric (which is just the Euclidean metric in Euclidean space) and preferred geodesics (Chapter 4).
- In the end, to overcome the drawbacks of binary segmentation, we proposed a novel Bayesian approach for fractional segmentation of white matter tracts and simultaneous

estimation of a multi-tensor diffusion model. With a prior that assumes the tensor and fractions fields inside each tract are spatially correlated, our method can reliably estimate multiple tensor compartments in fiber crossing regions even with low angular DWI. In addition, we also apply both the binary and the fractional segmentation methods to explore the white matter abnormalities in autism neuropsychiatric disorder (Chapter 5).

While we have endeavored to develop a robust and reliable framework for DWI tracking, segmentation, and tensor estimation, there remain a number of limitations of the proposed methods. First of all, the proposed adaptive Riemannian metric is effective when the tensor field is only rotating. When there are other effects in the tensor field, more complicated modulations of the metric are required. Second, the proposed binary segmentation method works well for tubular white matter structures. When the structures have branches, the characteristic vectors from the two ROIs of structure may point to similar directions inside these branches. Though we can try to segment the structures with several segments, the choices of the boundary of the segments are not always trivial. Moreover, while the fractional segmentation method can jointly solve the tract segmentation and multitensor model estimation, this method also assumes the number of tracts is known inside the brain region to be segmented. So care must be taken when the method is applied. I will talk about several issues in detail as potential future work in Section 6.2.

6.2 Future Work

In Chapter 3, we proposed a simple scalar field modulation of the Riemannian metric. The modulation we chose is scaling. As demonstrated empirically in Chapter 3, the scaling can correct the geodesics if the tensor filed is only rotating. However, if there are other effects, such as shrinkage or expansion, other kinds of modulation are needed, such as shearing, rotation, or other kinds of linear transformation. Moreover, the idea of modulation was motivated by forcing the geodesics to follow the principal eigenvector of the diffusion tensor, but it is possible to incorporate this modulation idea into diffusion tensor denoising or estimation by minimizing a chosen error function over the whole image domain. In addition, it is also interesting to generalize the similar idea to HARDI models. Moreover, there are two more areas we have identified as potential future work. First, the aliasing artifacts along the white matter boundary described in [54] have, to the best of our knowledge, not been addressed in the literature. One possible solution to this problem would be to use a fuzzy boundary where the cost function increases to infinity along the normal

direction. Currently the cost function changes instantaneously to infinity at the boundary (i.e., moving outside the boundary is infinite cost). Another issue is that the geodesics in front-propagation techniques can, in some cases, cross an edge between two adjacent tracts. We can envision a modification to our metric modulating function, e^{α}, that would increase the penalty for passing across such edges. This could be achieved by scaling the metric by a larger amount at edges, i.e., increasing the distances in these directions.

The segmentation methods we developed in Chapter 4 perform well on highly curved tracts; it might be able to recover U-shaped tracts between neighboring gyri, which are poorly recovered by classical tensor based tractography [39, 123]. In addition, our method needs to predefine two ROIs of the white matter tracts of interest, which requires the tracts of interest are well-characterized and the users have the prior knowledge about the white matter trajectory. Also, the position of the ROIs may influence analysis of the clinical studies, which need to be further studied. One possible future direction is to segment the white matter tract with only one ROI inside the tract, which requires less prior knowledge about the tract of interest. For example, Deschamps and Cohen [124] proposed freezing the propagation front for extraction of thin and long structures from a given single ROI. This idea can be used to segment white matter tracts with one ROI. The challenge is how to determine the appropriate conditions to freeze the front. Moreover, since the proposed method computes binary segmentation of the tracts, which sometimes undersegment or oversegment tracts, it might help to incorporate some anatomical prior, such as a white matter atlas, into our segmentation framework.

In Chapter 5, by incorporating a prior that assumes the tensor and fraction fields inside each tract are spatially correlated, our method can reliably estimate multiple tensor compartments in fiber crossing regions even with low angular DWI. However, this spatial prior on the foreground tracts is isotropic, which means the tensors and fractions tend to blur across the white matter tract boundaries. To prevent this, one idea is to use an anisotropic spatial prior [125]. For example, we can use a prior that assumes the tensors and fractions are spatially correlated only along the tensor directions. Moreover, our noise model could be replaced with a Rician noise likelihood, and it would also be interesting to investigate the sensitivity of our current gradient-based optimization to the initial binary segmentation and explore stochastic optimization schemes. In addition, the way we incorporate the background tensors into the statistical analysis is not elegant, and how to use this background information appropriately is open to future research.

Another important question in the proposed fractional segmentation method is how to

choose or set the strength of the spatial prior. If the prior is too strong, it will ignore the data and make all the tensors similar to each other. If the prior is too weak, the tensor estimation will be unstable because there are too many degrees of freedom in the tensor estimation. Though we used a cross validation approach in Chapter 5 to select the spatial prior parameter, such an approach is very time consuming. In addition, it is not accurate, for there is a spacing between the chosen parameter candidates, and the selected parameter is optimal for a group of subjects but not for a single subject. Thus, it is useful to find methods that can compute the optimal parameter both efficiently and accurately.

It is always exciting to study how the brain regions are connected, so it is important for us to understand the theories of normal brain and cognitive development. One important question that needs to be addressed in brain connectivity analysis is how to measure the strength of the connectivity between two brain regions. For example, a good connectivity metric should be invariant to the distance between the two regions, i.e., this metric should not necessarily increase when the geodesic gets longer. For both the stochastic tractography and the front-propagation methods, the outputted probability and time cost are not invariant to the distance. We can normalize the probability or time cost by dividing it by the distance, but this is ad hoc, and it is more interesting to use properties invariant to distance to define a metric. One possible example is the angle between the two characteristic vector fields from the two predefined ROIs. If we find a good connectivity metric, we can use it to analyze whole brain connectivity. To explore whole brain connectivity, we can first select many different ROIs, compute the strength of the region-to-region connectivity of each pair of these regions, and obtain a symmetric connectivity matrix, A, where A_{ij} denotes the strength of the connectivity between region i and region j. Based on this matrix, we can use some clustering methods, such as spectral clustering, to extract meaningful connectivity information about how the brain regions are connected.

REFERENCES

[1] A. J. Hughes, S. E. Daniel, L. Kilford, and A. J. Lees, "Accuracy of clinical diagnosis of idiopathic parkinson's disease: a clinico-pathological study of 100 cases." *J. Neurol. Neurosurg. Psychiatry*, vol. 55, no. 3, pp. 181–184, 1992.

[2] J. Schwob, T. Fuller, J. Price, and J. Olney, "Widespread patterns of neuronal damage following systemic or intracerebral injections of kainic acid: a histological study," *Neuroscience*, vol. 5, no. 6, pp. 991–1014, 1980.

[3] J. Altman and G. D. Das, "Autoradiographic and histological studies of postnatal neurogenesis. i. a longitudinal investigation of the kinetics, migration and transformation of cells incoorporating tritiated thymidine in neonate rats, with special reference to postnatal neurogenesis in some brain regions," *J. Comp. Neurol.*, vol. 126, no. 3, pp. 337–389, 1966.

[4] B. Ferguson, M. K. Matyszak, M. M. Esiri, and V. H. Perry, "Axonal damage in acute multiple sclerosis lesions." *Brain*, vol. 120, no. 3, pp. 393–399, 1997.

[5] F. Bloch, "Nuclear induction," *Phys. Rev.*, vol. 70, no. 7–8, p. 460, 1946.

[6] E. L. Hahn, "Spin echoes," *Phys. Rev.*, vol. 80, no. 4, p. 580, 1950.

[7] P. C. Lauterbur *et al.*, "Image formation by induced local interactions: examples employing nuclear magnetic resonance," *Nature*, vol. 242, no. 5394, pp. 190–191, 1973.

[8] H. Y. Carr and E. M. Purcell, "Effects of diffusion on free precession in nuclear magnetic resonance experiments," *Phys. Rev.*, vol. 94, no. 3, p. 630, 1954.

[9] H. Y. Carr, "Field gradients in early mri," *Phys. Today*, vol. 57, no. 7, pp. 83–83, 2004.

[10] W. Hollingworth, C. J. Todd, M. I. Bell, Q. Arafat, S. Girling, K. R. Karia, and A. K. Dixon, "The diagnostic and therapeutic impact of MRI: an observational multi-centre study," *Clin. Radiol.*, vol. 55, no. 11, pp. 825–831, 2000.

[11] M. E. Shenton, C. C. Dickey, M. Frumin, and R. W. McCarley, "A review of MRI findings in schizophrenia," *Schizophr. Res.*, vol. 49, no. 1, pp. 1–52, 2001.

[12] C. Jack, R. C. Petersen, Y. C. Xu, P. C. O'Brien, G. E. Smith, R. J. Ivnik, B. F. Boeve, S. C. Waring, E. G. Tangalos, and E. Kokmen, "Prediction of AD with MRI-based hippocampal volume in mild cognitive impairment," *Neurology*, vol. 52, no. 7, pp. 1397–1397, 1999.

[13] J. Jennings, P. Sundgren, J. Attwood, J. McCune, and P. Maly, "Value of MRI of the brain in patients with systemic lupus erythematosus and neurologic disturbance," *Neuroradiology*, vol. 46, no. 1, pp. 15–21, 2004.

[14] A. C. Evans, "The NIH MRI study of normal brain development," *Neuroimage*, vol. 30, no. 1, pp. 184–202, 2006.

[15] E. Stejskal and J. Tanner, "Spin diffusion measurements: spin echoes in the presence of a time-dependent field gradient," *J. Chem. Phys.*, vol. 42, no. 1, p. 288, 1965.

[16] S. Posse, C. A. Cuenod, and D. Le Bihan, "Human brain: proton diffusion MR spectroscopye," *Radiology*, vol. 188, pp. 719–725, 1993.

[17] P. J. Basser, J. Mattiello, and D. Lebihan, "Estimation of the effective self-diffusion tensor from the NMR spin echo," *J. Magn. Reson.*, vol. 103, no. 3, pp. 247–254, 1994.

[18] V. J. Wedeen, P. Hagmann, W.-Y. I. Tseng, T. G. Reese, and R. M. Weisskoff, "Mapping complex tissue architecture with diffusion spectrum magnetic resonance imaging," *Magn. Reson. Med.*, vol. 54, no. 6, pp. 1377–1386, 2005.

[19] C. Beaulieu, "The basis of anisotropic water diffusion in the nervous system–a technical review," *Nucl. Magn. Reson. Biomed.*, vol. 15, no. 7–8, pp. 435–455, 2002.

[20] P. J. Basser and D. K. Jones, "Diffusion-tensor MRI: theory, experimental design and data analysis–a technical review," *Nucl. Magn. Reson. Biomed.*, vol. 15, no. 7-8, pp. 456–467, 2002.

[21] P. J. Basser and C. Pierpaoli, "Microstructural and physiological features of tissues elucidated by quantitative-diffusion-tensor MRI," *J. Magn. Reson.*, vol. 213, no. 2, pp. 560–570, 2011.

[22] P. Sundgren, Q. Dong, D. Gomez-Hassan, S. Mukherji, P. Maly, and R. Welsh, "Diffusion tensor imaging of the brain: review of clinical applications," *Neuroradiology*, vol. 46, no. 5, pp. 339–350, 2004.

[23] Y. Masutani, S. Aoki, O. Abe, N. Hayashi, and K. Otomo, "MR diffusion tensor imaging: recent advance and new techniques for diffusion tensor visualization," *Eur. J. Radiol.*, vol. 46, no. 1, pp. 53–66, 2003.

[24] P. W. Schaefer, P. E. Grant, and R. G. Gonzalez, "Diffusion-weighted MR imaging of the brain," *Radiology*, vol. 217, no. 2, pp. 331–345, 2000.

[25] Y. Assaf and O. Pasternak, "Diffusion tensor imaging (dti)-based white matter mapping in brain research: a review," *J. Mol. Neurosci.*, vol. 34, no. 1, pp. 51–61, 2008.

[26] P. Hagmann, M. Kurant, X. Gigandet, P. Thiran, V. J. Wedeen, R. Meuli, and J.-P. Thiran, "Mapping human whole-brain structural networks with diffusion MRI," *PLoS ONE*, vol. 2, no. 7, p. e597, 2007.

[27] E. V. Sullivan and A. Pfefferbaum, "Diffusion tensor imaging in normal aging and neuropsychiatric disorders," *Eur. J. Radiol.*, vol. 45, no. 3, pp. 244–255, 2003.

[28] M. Kubicki, C.-F. Westin, S. E. Maier, H. Mamata, M. Frumin, H. Ersner-Hershfield, R. Kikinis, F. A. Jolesz, R. McCarley, and M. E. Shenton, "Diffusion tensor imaging and its application to neuropsychiatric disorders," *Harvard Rev. Psychiat.*, vol. 10, no. 6, pp. 324–336, 2002.

[29] D. G. Amaral, C. M. Schumann, and C. W. Nordahl, "Neuroanatomy of autism," *Trends Neurosci.*, vol. 31, no. 3, pp. 137–145, 2008.

[30] D. B. Bashat, L. B. Sira, M. Graif, P. Pianka, T. Hendler, Y. Cohen, and Y. Assaf, "Normal white matter development from infancy to adulthood: comparing diffusion tensor and high b value diffusion weighted MR images," *J. Magn. Reson. Imaging*, vol. 21, no. 5, pp. 503–511, 2005.

[31] J. Schneider, S. Confort-Gouny, Y. Le Fur, P. Viout, M. Bennathan, F. Chapon, C. Fogliarini, P. Cozzone, and N. Girard, "Diffusion-weighted imaging in normal fetal brain maturation," *Eur. Radiol.*, vol. 17, no. 9, pp. 2422–2429, 2007.

[32] A. L. Alexander, J. E. Lee, M. Lazar, and A. S. Field, "Diffusion tensor imaging of the brain," *Neurotherapeutics*, vol. 4, no. 3, pp. 316–329, 2007.

[33] M. Morriss, R. Zimmerman, L. Bilaniuk, J. Hunter, and J. Haselgrove, "Changes in brain water diffusion during childhood," *Neuroradiology*, vol. 41, no. 12, pp. 929–934, 1999.

[34] S. J. Counsell, J. M. Allsop, M. C. Harrison, D. J. Larkman, N. L. Kennea, O. Kapellou, F. M. Cowan, J. V. Hajnal, A. D. Edwards, and M. A. Rutherford, "Diffusion-weighted imaging of the brain in preterm infants with focal and diffuse white matter abnormality," *Pediatrics*, vol. 112, no. 1, pp. 1–7, 2003.

[35] S. Eriksson, F. Rugg-Gunn, M. Symms, G. Barker, and J. Duncan, "Diffusion tensor imaging in patients with epilepsy and malformations of cortical development," *Brain*, vol. 124, no. 3, pp. 617–626, 2001.

[36] R. McKinstry, J. Miller, A. Snyder, A. Mathur, G. Schefft, C. Almli, J. Shimony, S. Shiran, and J. Neil, "A prospective, longitudinal diffusion tensor imaging study of brain injury in newborns," *Neurology*, vol. 59, no. 6, pp. 824–833, 2002.

[37] S. Price, N. Burnet, T. Donovan, H. Green, A. Pena, N. Antoun, J. Pickard, T. Carpenter, and J. Gillard, "Diffusion tensor imaging of brain tumours at 3T: a potential tool for assessing white matter tract invasion?" *Clin. Radiol.*, vol. 58, no. 6, pp. 455–462, 2003.

[38] S. Mori, B. J. Crain, V. P. Chacko, and P. C. M. van Zijl, "Three dimensional tracking of axonal projections in the brain by magnetic resonance imaging," *Ann. Neurol.*, vol. 45, pp. 265–269, 1999.

[39] T. E. Conturo, N. F. Lori, and M. E. Raichle, "Tracking neuronal fiber pathways in the living human brain," *P. Natl. A. Sci.*, vol. 96, p. 10422, 1999.

[40] P. J. Basser, S. Pajevic, C. Pierpaoli, J. Duda, and A. Aldroubi, "In-vivo fiber tractography using DT-MRI data," *Magn. Reson. Med.*, vol. 44, pp. 625–632, 2000.

[41] M. A. Koch, D. G. Norris, and H.-G. Margret, "An investigation of functional and anatomical connectivity using magnetic resonance imaging," *Neuroimage*, vol. 16, pp. 241–250, 2002.

[42] T. Behrens, M. Woolrich, M. Jenkinson, H. Johansen-Berg, R. Nunes, S. Clare, P. Matthews, J. Brady, and S. Smith, "Characterization and propagation of uncertainty in diffusion-weighted MR imaging," *Magn. Reson. Med.*, vol. 50, pp. 1077–1088, 2003.

[43] G. J. M. Parker, H. A. Haroon, and C. A. M. Wheeler-Kingshott, "A framework for a streamline-based probabilistic index of connectivity (PICo) using a structural interpretation of MRI diffusion measurements," *J. Magn. Reson. Imaging*, vol. 18, pp. 242–254, 2003.

[44] M. Lazar and A. L. Alexander, "Bootstrap white matter tractography (BOOT-TRAC)," *Neuroimage*, vol. 24, pp. 524–532, 2005.

[45] O. Friman, G. Farnebck, and C.-F. Westin, "A Bayesian approach for stochastic white matter tractography," *IEEE Trans. Med. Imag.*, pp. 965–978, 2006.

[46] D. K. Jones, "Tractography gone wild: probabilistic fibre tracking using the wild bootstrap with diffusion tensor MRI," *IEEE Trans. Med. Imag.*, vol. 27, no. 9, pp. 1268–1274, 2008.

[47] G. Parker, C. Wheeler-Kingshott, and G. Barker, "Estimating distributed anatomical connectivity using fast marching methods and diffusion tensor imaging," *IEEE Trans. Med. Imag.*, vol. 21, pp. 505–512, 2002.

[48] L. O'Donnell, S. Haker, and C.-F. Westin, "New approaches to estimation of white matter connectivity in diffusion tensor MRI: elliptic PDEs and geodesics in a tensor-warped space," in *Proc. Int. Conf. Medical Image Computing and Computer-Assisted Intervention*, vol. 2488, 2002, pp. 459–466.

[49] M. Jackowski, C. Y. Kao, M. Qiu, R. T. Constable, and L. H. Staib, "White matter tractography by anisotropic wavefront evolution and diffusion tensor imaging," *Med. Image Anal.*, vol. 9, no. 5, pp. 427–440, 2005.

[50] J. Melonakos, V. Mohan, M. Niethammer, K. Smith, M. Kubicki, and A. Tannenbaum, "Finsler tractography for white matter connectivity analysis of the cingulum bundle," in *Proc. Int. Conf. Medical Image Computing and Computer-Assisted Intervention*, vol. 4791, 2007, pp. 36–43.

[51] E. Pichon, C.-F. Westin, and A. Tannenbaum, "A Hamilton-Jacobi-Bellman approach to high angular resolution diffusion tractography," in *Proc. Int. Conf. Medical Image Computing and Computer-Assisted Intervention*, vol. 3749, 2005, pp. 180–187.

[52] P. T. Fletcher, R. Tao, W.-K. Jeong, and R. T. Whitaker, "A volumetric approach to quantifying region-to-region white matter connectivity in diffusion tensor MRI," in *Proc. Int. Conf. Information Processing in Medical Imaging*, vol. 4584, 2007, pp. 346–358.

[53] S. Jbabdi, P. Bellec, R. Toro, J. Daunizeau, M. Pélégrini-Issac, and H. Benali, "Accurate anisotropic fast marching for diffusion-based geodesic tractography," *Int. J. Biomed. Imaging*, vol. 2008, pp. 2:1–2:12, Jan. 2008.

[54] X. Hao, R. T. Whitaker, and P. T. Fletcher, "Adaptive Riemannian metrics for improved geodesic tracking of white matter," in *Proc. Int. Conf. Information Processing in Medical Imaging*, Kloster Irsee, Germany, 2011, pp. 13–24.

[55] X. Hao, K. Zygmunt, R. T. Whitaker, and P. T. Fletcher, "Improved segmentation of white matter tracts with adaptive Riemannian metrics," *Med. Image Anal.*, vol. 18, no. 1, pp. 161–175, 2014.

[56] L. Zhukov, K. Museth, D. Breen, R. Whitaker, and A. H. Barr, "Level set modeling and segmentation of DT-MRI brain data," *J. Electron. Imaging*, vol. 12, pp. 125–133, 2003.

[57] M. Rousson, C. Lenglet, and R. Deriche, "Level set and region based surface propagation for diffusion tensor MRI segmentation," in *Proc. ECCV Workshops Computer Vision and Mathematical Methods in Medical and Biomedical Image Analysis*, 2004, pp. 123–134.

[58] C. Lenglet, M. Rousson, R. Deriche, O. Faugeras, S. Lehericy, and K. Ugurbil, "A Riemannian approach to diffusion tensor images segmentation," in *Proc. Int. Conf. Information Processing in Medical Imaging*, 2005, pp. 591–602.

[59] Z. Wang and B. Vemuri, "DTI segmentation using an information theoretic tensor dissimilarity measure," *IEEE Trans. Med. Imag.*, vol. 24, no. 10, pp. 1267–1277, Oct. 2005.

[60] U. Ziyan, D. Tuch, and C.-F. Westin, "Segmentation of thalamic nuclei from DTI using spectral clustering," in *Proc. Int. Conf. Medical Image Computing and Computer-Assisted Intervention*, vol. 4191, 2006, pp. 807–814.

[61] S. P. Awate, H. Zhang, and J. C. Gee, "Fuzzy nonparametric DTI segmentation for robust cingulum-tract extraction," in *Proc. Int. Conf. Medical Image Computing and Computer-Assisted Intervention*, Brisbane, Australia, 2007, pp. 294–301.

[62] J. Melonakos, M. Niethammer, V. Mohan, M. Kubicki, J. Miller, and A. Tannenbaum, "Locally-constrained region-based methods for DW-MRI segmentation," in *Proc. IEEE Int. Conf. Computer Vision*, 2007, pp. 1–8.

[63] M. Niethammer, C. Zach, J. Melonakos, and A. Tannenbaum, "Near-tubular fiber bundle segmentation for diffusion weighted imaging: Segmentation through frame reorientation," *Neuroimage*, vol. 45, no. 1, Supplement 1, pp. S123–S132, 2009.

[64] D. S. Tuch, "Diffusion MRI of complex tissue structure," Ph.D. dissertation, Division of Health Sciences and Technology, Massachusetts Institute of Technology, Cambridge, MA, Jan 2002.

[65] H.-E. Assemlal, D. Tschumperlé, L. Brun, and K. Siddiqi, "Recent advances in diffusion MRI modeling: angular and radial reconstruction," *Med. Image Anal.*, vol. 15, no. 4, pp. 369–396, 2011.

[66] D. S. Tuch, T. G. Reese, M. R. Wiegell, N. Makris, J. W. Belliveau, and V. J. Wedeen, "High angular resolution diffusion imaging reveals intravoxel white matter fiber heterogeneity," *Magn. Reson. Med.*, vol. 48, no. 4, pp. 577–582, 2002.

[67] D. S. Tuch, "Q-ball imaging," *Magn. Reson. Med.*, vol. 52, no. 6, pp. 1358–1372, 2004.

[68] V. J. Wedeen, R. Wang, J. D. Schmahmann, T. Benner, W. Tseng, G. Dai, D. Pandya, P. Hagmann, H. D'Arceuil, and A. J. de Crespigny, "Diffusion spectrum magnetic resonance imaging (DSI) tractography of crossing fibers," *Neuroimage*, vol. 41, no. 4, pp. 1267–1277, 2008.

[69] Y. Cohen and Y. Assaf, "High b-value q-space analyzed diffusion-weighted MRS and MRI in neuronal tissues–a technical review," *Nucl. Magn. Reson. Biomed.*, vol. 15, no. 7-8, pp. 516–542, 2002.

[70] L. R. Frank, "Characterization of anisotropy in high angular resolution diffusion-weighted MRI," *Magn. Reson. Med.*, vol. 47, no. 6, pp. 1083–1099, 2002.

[71] B. Jian, B. C. Vemuri, E. Özarslan, P. R. Carney, and T. H. Mareci, "A novel tensor distribution model for the diffusion-weighted MR signal," *Neuroimage*, vol. 37, no. 1, pp. 164–176, 2007.

[72] T. E. J. Behrens, M. W. Woolrich, M. Jenkinson, H. Johansen-Berg, R. G. Nunes, S. Clare, P. M. Matthews, J. M. Brady, and S. M. Smith, "Characterization and propagation of uncertainty in diffusion-weighted MR imaging," *Magn. Reson. Med.*, vol. 50, pp. 1077–1088, 2003.

[73] E. Özarslan and T. H. Mareci, "Generalized diffusion tensor imaging and analytical relationships between diffusion tensor imaging and high angular resolution diffusion imaging," *Magn. Reson. Med.*, vol. 50, no. 5, pp. 955–965, 2003.

[74] C. Liu, R. Bammer, B. Acar, and M. E. Moseley, "Characterizing non-gaussian diffusion by using generalized diffusion tensors," *Magn. Reson. Med.*, vol. 51, no. 5, pp. 924–937, 2004.

[75] M. Moseley, Y. Cohen, J. Kucharczyk, J. Mintorovitch, H. Asgari, M. Wendland, J. Tsuruda, and D. Norman, "Diffusion-weighted MR imaging of anisotropic water diffusion in cat central nervous system." *Radiology*, vol. 176, no. 2, pp. 439–445, 1990.

[76] W.-K. Jeong, P. T. Fletcher, R. Tao, and R. T. Whitaker, "Interactive visualization of volumetric white matter connectivity in diffusion tensor MRI using a parallel-hardware Hamilton-Jacobi solver," *IEEE Trans. Vis. Comput. Graphics*, vol. 13, no. 6, pp. 1480–1487, 2007.

[77] X. Hao and P. T. Fletcher, "Joint fractional segmentation and multi-tensor estimation in diffusion MRI," in *Proc. Int. Conf. Information Processing in Medical Imaging*, 2013, vol. 7917, pp. 340–351.

[78] Q. Jarosz, "Structure of a typical neuron." [Online]. Available: http://en.wikipedia.org/wiki/File:Neuron_Hand-tuned.svg

[79] A. Einstein, *Investigations on the Theory of the Brownian Movement.* Mineola, NY: Courier Dover Publications, 1956.

[80] K. O. Lim, M. Hedehus, M. Moseley, A. de Crespigny, E. V. Sullivan, and A. Pfefferbaum, "Compromised white matter tract integrity in schizophrenia inferred from diffusion tensor imaging," *Arch. Gen. Psychiat.*, vol. 56, no. 4, pp. 367–374, 1999.

[81] K. L. Miller, C. J. Stagg, G. Douaud, S. Jbabdi, S. M. Smith, T. E. Behrens, M. Jenkinson, S. A. Chance, M. M. Esiri, N. L. Voets, N. Jenkinson, T. Z. Aziz, M. R. Turner, H. Johansen-Berg, and J. A. McNab, "Diffusion imaging of whole, post-mortem human brains on a clinical MRI scanner," *Neuroimage*, vol. 57, no. 1, pp. 167–181, 2011.

[82] O. Friman, G. Farneback, and C.-F. Westin, "A Bayesian approach for stochastic white matter tractography," *IEEE Trans. Med. Imag.*, vol. 25, no. 8, pp. 965–978, 2006.

[83] M. Björnemo, A. Brun, R. Kikinis, and C.-F. Westin, "Regularized stochastic white matter tractography using diffusion tensor MRI," in *Proc. Int. Conf. Medical Image Computing and Computer-Assisted Intervention*, Tokyo, Japan, 2002, pp. 435–442.

[84] F. Zhang, E. Hancock, C. Goodlett, and G. Gerig, "Probabilistic white matter fiber tracking using particle filtering and von mises-fisher sampling," *Med. Image Anal.*, vol. 13, no. 1, pp. 5–18, Feb. 2009.

[85] S. Barbieri, M. H. A. Bauer, J. Klein, J. H. Moltz, C. Nimsky, and H. K. Hahn, "DTI segmentation via the combined analysis of connectivity maps and tensor distances," *Neuroimage*, vol. 60, no. 2, pp. 1025–1035, 2012.

[86] M. do Carmo, *Riemannian Geometry.* Boston, MA: Birkhauser Verlag AG, 1992.

[87] J. Lee, *Introduction to Smooth Manifolds.* New York City, NY: Springer, 2003.

[88] M. Spivak, *A Comprehensive Introduction to Differential Geometry, vol. 1.* Houston, TX: Publish or Perish, Inc., 1999.

[89] W.-K. Jeong and R. T. Whitaker, "A fast iterative method for eikonal equations," *SIAM J. Sci. Comput.*, vol. 30, no. 5, pp. 2512–2534, 2008.

[90] M. Jackowski, C. Y. Kao, M. Qiu, R. T. Constable, and L. H. Staib, "Estimation of anatomical connectivity by anisotropic front propagation and diffusion tensor imaging," in *Proc. Int. Conf. Medical Image Computing and Computer-Assisted Intervention*, vol. 3217, 2004, pp. 663–670.

[91] P. Holoborodko, "Smooth noise robust differentiators." [Online]. Available: http://www.holoborodko.com/pavel/numerical-methods/numerical-derivative/smooth-low-noise-differentiators/

[92] M. R. Hestenes and E. Stiefel, "Methods of conjugate gradients for solving linear systems," *J. Res. Nat. Bur. Stand.*, vol. 49, pp. 409–436, Dec. 1952.

[93] Y. Saad and M. H. Schultz, "GMRES: a generalized minimal residual algorithm for solving nonsymmetric linear systems," *SIAM J. Sci. Stat. Comput.*, vol. 7, no. 3, pp. 856–869, Jul. 1986.

[94] R. Fletcher, "Conjugate gradient methods for indefinite systems," in *Numerical Analysis*, G. Watson, Ed. Berlin, Germany: Springer, 1976, pp. 73–89.

[95] S. Balay, J. Brown, , K. Buschelman, V. Eijkhout, W. D. Gropp, D. Kaushik, M. G. Knepley, L. C. McInnes, B. F. Smith, and H. Zhang, "PETSc users manual," Argonne National Laboratory, Tech. Rep. ANL-95/11 - Revision 3.4, 2013.

[96] S. Balay, J. Brown, K. Buschelman, W. D. Gropp, D. Kaushik, M. G. Knepley, L. C. McInnes, B. F. Smith, and H. Zhang, "PETSc Web page." [Online]. Available: http://www.mcs.anl.gov/petsc

[97] S. Balay, W. D. Gropp, L. C. McInnes, and B. F. Smith, "Efficient management of parallelism in object oriented numerical software libraries," in *Modern Software Tools in Scientific Computing*, E. Arge, A. M. Bruaset, and H. P. Langtangen, Eds. Berlin, Germany: Birkhäuser Press, 1997, pp. 163–202.

[98] G. Rohde, A. Barnett, P. Basser, S. Marenco, and C. Pierpaoli, "Comprehensive approach for correction of motion and distortion in diffusion-weighted MRI," *Magn. Reson. Med.*, vol. 51, pp. 103–114, 2004.

[99] N. Barnea-Goraly, V. Menon, M. Eckert, L. Tamm, R. Bammer, A. Karchemskiy, C. C. Dant, and A. L. Reiss, "White matter development during childhood and adolescence: a cross-sectional diffusion tensor imaging study," *Cereb. Cortex*, vol. 15, no. 12, pp. 1848–1854, 2005.

[100] P.-L. Bazin, C. Ye, J. A. Bogovic, N. Shiee, D. S. Reich, J. L. Prince, and D. L. Pham, "Direct segmentation of the major white matter tracts in diffusion tensor images," *Neuroimage*, vol. 58, no. 2, pp. 458–468, 2011.

[101] I. Corouge, P. T. Fletcher, S. Joshi, S. Gouttard, and G. Gerig, "Fiber tract-oriented statistics for quantitative diffusion tensor MRI analysis," *Med. Image Anal.*, vol. 10, no. 5, pp. 786–798, 2006.

[102] N. Otsu, "A threshold selection method from gray-level histograms," *IEEE Trans. Syst. Man And Cybern.*, vol. 9, no. 1, pp. 62–66, 1979.

[103] H. Huang, J. Zhang, P. C. van Zijl, and S. Mori, "Analysis of noise effects on DTI-based tractography using the brute-force and multi-ROI approach," *Magn. Reson. Med.*, vol. 52, no. 3, pp. 559–565, 2004.

[104] S. Mori, B. J. Crain, V. P. Chacko, and P. C. M. Van Zijl, "Three-dimensional tracking of axonal projections in the brain by magnetic resonance imaging," *Ann. Neurol.*, vol. 45, no. 2, pp. 265–269, 1999.

[105] D. Weinstein, G. Kindlmann, and E. Lundberg, "Tensorlines: advection-diffusion based propagation through diffusion tensor fields," in *Proc. IEEE Conf. Visualization*, Los Alamitos, CA, USA, 1999, pp. 249–253.

[106] P. A. Cook, Y. Bai, N. S. Gilani, K. K. Seunarine, M. G. Hall, G. J. Parker, and D. C. Alexander, "Camino: Open-source diffusion-MRI reconstruction and processing," in *Proc. 14th Scientific Meeting Int. Society for Magnetic Resonance in Medicine*, 2006, p. 2759.

[107] S. Mori, S. Wakana, P. C. Van Zijl, and L. Nagae-Poetscher, *MRI atlas of human white matter*. Oak, IL: American Society of Neuroradiology, 2005.

[108] S. Wakana, A. Caprihan, M. M. Panzenboeck, J. H. Fallon, M. Perry, R. L. Gollub, K. Hua, J. Zhang, H. Jiang, P. Dubey *et al.*, "Reproducibility of quantitative tractography methods applied to cerebral white matter," *Neuroimage*, vol. 36, no. 3, pp. 630–644, 2007.

[109] K. Hua, J. Zhang, S. Wakana, H. Jiang, X. Li, D. S. Reich, P. A. Calabresi, J. J. Pekar, P. van Zijl, and S. Mori, "Tract probability maps in stereotaxic spaces: analyses of white matter anatomy and tract-specific quantification," *Neuroimage*, vol. 39, no. 1, pp. 336–347, 2008.

[110] A. L. Alexander, K. M. Hasan, M. Lazar, J. S. Tsuruda, and D. L. Parker, "Analysis of partial volume effects in diffusion-tensor MRI," *Magn. Reson. Med.*, vol. 45, no. 5, pp. 770–780, 2001.

[111] H. Oouchi, K. Yamada, K. Sakai, O. Kizu, T. Kubota, H. Ito, and T. Nishimura, "Diffusion anisotropy measurement of brain white matter is affected by voxel size: underestimation occurs in areas with crossing fibers," *Am. J. Neuroradiol.*, vol. 28, no. 6, pp. 1102–1106, 2007.

[112] C. Metzler-Baddeley, M. J. O'Sullivan, S. Bells, O. Pasternak, and D. K. Jones, "How and how not to correct for CSF-contamination in diffusion MRI," *Neuroimage*, vol. 59, no. 2, pp. 1394–1403, 2012.

[113] S. B. Vos, D. K. Jones, M. A. Viergever, and A. Leemans, "Partial volume effect as a hidden covariate in DTI analyses," *Neuroimage*, vol. 55, no. 4, pp. 1566–1576, 2011.

[114] S. N. Sotiropoulos, L. Bai, P. S. Morgan, D. P. Auer, C. S. Constantinescu, and C. R. Tench, "A regularized two-tensor model fit to low angular resolution diffusion images using basis directions," *J. Magn. Reson. Imaging*, vol. 28, no. 1, pp. 199–209, 2008.

[115] W. Guo, Q. Zeng, Y. Chen, and Y. Liu, "Using multiple tensor deflection to reconstruct white matter fiber traces with branching," in *Proc. IEEE Int. Symp. Biomedical Imaging: Nano to Macro*, 2006, pp. 69–72.

[116] B. A. Landman, H. Wan, J. A. Bogovic, P.-L. Bazin, and J. L. Prince, "Resolution of crossing fibers with constrained compressed sensing using traditional diffusion tensor MRI," *Neuroimage*, vol. 59, pp. 2175–86, 2012.

[117] O. Pasternak, N. Sochen, Y. Gur, N. Intrator, and Y. Assaf, "Free water elimination and mapping from diffusion MRI," *Magn. Reson. Med.*, vol. 62, no. 3, pp. 717–730, 2009.

[118] S. Wei, J. Hua, J. Bu, C. Chen, and Y. Yu, "Bayesian regularization of diffusion tensor images using hierarchical mcmc and loopy belief propagation," in *Proc. IEEE Int. Conf. Image Processing*, 2010, pp. 65–68.

[119] D. Tschumperlé and R. Deriche, "Variational frameworks for DT-MRI estimation, regularization and visualization," in *Proc. IEEE Int. Conf. Computer Vision*, vol. vol. 1, 2003, pp. 116–121.

[120] M. Liu, B. C. Vemuri, and R. Deriche, "A robust variational approach for simultaneous smoothing and estimation of DTI," *Neuroimage*, vol. 67, pp. 33–41, 2013.

[121] O. Pasternak, Y. Assaf, N. Intrator, and N. Sochen, "Variational multiple-tensor fitting of fiber-ambiguous diffusion-weighted magnetic resonance imaging voxels," *Magn. Reson. Imaging*, vol. 26, no. 8, pp. 1133–1144, 2008.

[122] P. T. Fletcher, R. T. Whitaker, R. Tao, M. B. DuBray, A. Froehlich, C. Ravichandran, A. L. Alexander, E. D. Bigler, N. Lange, and J. E. Lainhart, "Microstructural connectivity of the arcuate fasciculus in adolescents with high-functioning autism," *Neuroimage*, vol. 51, no. 3, pp. 1117–1125, 2010.

[123] M. Catani, F. DellAcqua, F. Vergani, F. Malik, H. Hodge, P. Roy, R. Valabregue, and M. Thiebaut de Schotten, "Short frontal lobe connections of the human brain," *Cortex*, vol. 48, no. 2, pp. 273–291, 2012.

[124] T. Deschamps and L. D. Cohen, "Fast extraction of tubular and tree 3D surfaces with front propagation methods," in *Proc. IEEE Int. Conf. Pattern Recognition*, 2002, pp. 731–734.

[125] Z. Wang, B. Vemuri, Y. Chen, and T. Mareci, "A constrained variational principle for direct estimation and smoothing of the diffusion tensor field from complex DWI," *IEEE Trans. Med. Imag.*, vol. 23, no. 8, pp. 930–939, 2004.